# From Flux Emergence to Decay

## A High-resolution Study of Sunspots

Universitäts-Dissertation
zur Erlangung des akademischen Grades
doctor rerum naturalium
(Dr. rer. nat.)
in der Wissenschaftsdiziplin Astronomie und Astrophysik

eingereicht an der
Mathematisch-Naturwissenschaftlichen Fakultät
Institut für Physik und Astronomie
der Univestät Potsdam
und
Leibniz-Institut für Astrophysik Potsdam

Robert Kamlah

2024 December 19


Leibniz-Institut für Astrophysik Potsdam
An der Sternwarte 16
14482 Potsdam


Universität Potsdam, Campus Golm
Institut für Physik und Astronomie (Haus 28)
Karl-Liebknecht-Strasse 24/25
14476 Potsdam-Golm

Erstbetreuer/Gutachter: Prof. Dr. Carsten Denker
Zweitbetreuerin: Dr. Meetu Verma
Externer Gutachter: Prof. Dr. Francesco Berrilli
Externer Gutachter: Prof. Dr. Arnold Hanslmeier
Mentorin: Prof. Dr. Maria-Rosa Cioni

# Contents

## Abstract

In order to gain a comprehensive understanding of the dynamic processes occurring on the Sun, it is essential to closely study of the dynamic interplay between plasma flows and magnetic fields. The interplay between plasma flows and magnetic fields within active regions is the primary driver of the formation and evolution of these regions. Once magnetic flux bundles have pierced the photosphere and become visible as dark surface structures, they extend as a canopy structure into the chromosphere and higher atmospheric layers. The emergence of magnetic features affects the typical surface flows, which are generally characterized by global large-scale flow motions and divergence centers caused by granulation. Moreover, their appearance impacts the entire atmosphere, potentially affecting the entire heliosphere causing explosive events such as flares and especially coronal mass ejections (CMEs).

Nevertheless, the processes by which active regions emerge, evolve and decay remain poorly understood. What are the determining factors that make the leading or trailing part the dominant one? What processes, discernible at the photospheric or chromospheric level, contribute to the heating of the corona? What are the mechanisms by which emerging magnetic flux bundles and plasma motions on the solar surface interact with each other? What are the consequences for the evolution of active regions? What processes regulate the evolution of magnetic flux bundles as they rise into the chromosphere, beyond the observed extension in a canopy-like structure? What are the conditions that give rise to the formation of a penumbra? What are the determining factors that influence whether a penumbra fully develops into its characteristic fine filamentary structure or only exhibits a more rudimentary form? To what extent do photospheric flow fields exert an influence on those typically observed in the chromosphere? Furthermore, it is little understood at which moment the gradual process of sunspot decay begins. This raises the question of whether a critical value of the magnetic field marks the onset of penumbral decay, and consequently the decay of the entire sunspot. In this context, the role played by the surrounding plasma motions requires further scrutiny. Is it solely responsible for the advection of small-scale moving magnetic features (MMFs), or does a change in the surrounding flows and magnetic fields instigates penumbral decay?

This doctoral research investigates the complex processes of emergence, evolution, and decay of active regions on the ever-changing Sun. In order to achieve this objective, surface features resulting from the influence of strong magnetic fields, such as pores and sunspots, are examined at the highest spatial, spectral, and temporal resolution, as well as with high polarimetric sensitivity. The data analyzed in this work comprises high-resolution ground-based imaging and spectro-polarimetric data. However, the high-resolution observations only unveil their full potential when placed in context with synoptic data, thus, establishing statistical significance and accurately placing them in the long-term evolution of active regions. The combination of this data enabled a detailed analysis of the three-dimensional magnetic and flow fields in the photosphere and chromosphere.

Considering the complex interaction of plasma motions and magnetic fields, sunspots play a special role in this context. High-resolution observations of the evolution of sunspots, from formation to decay, provide significant insights into the dynamics of the Sun. Optimally, observations should start prior to the initial disturbance of the quiet Sun by emerging magnetic flux bundles and continue to cover the entirety of the active region life cycle. This would include, the formation of a penumbra, which transforms a simple pore into a sunspot, thereby introducing further complexity into the magnetic and flow structure. Later, the evolution into a complex active region must be observed, which consists of multiple sunspots, pores, and related features such as light bridges. These are embedded in a complex plasma flow and magnetic structure until the magnetic flux eventually dissipates and decays. Nevertheless, research should not be limited to sunspots alone, but should also encompass smaller features in the periphery and those related to spots, which should be included in the analysis.

The objective of this research project is to enhance our understanding of active region dynamics. The utilization of sophisticated methods, including Background-subtracted Solar Activity Maps (BaSAMs), Local Correlation Tracking (LCT), and the Stokes Inversions based on Response function (SIR) code, enabled comprehensive studies of several active regions observed in the photosphere and chromosphere. These studies encompassed pores, sunspots with rudimentary and fully formed penumbra, light bridges, and several small-scale features during different stages of evolution.

These research studies are the foundation of three first-author, peer-reviewed articles in scientific journals.

1. The first publication resulting from this doctoral research covered the topic *High-resolution Imaging of Solar Pores* and was published in 2023 in the journal *Astronomy & Astrophysics* (DOI:10.1051/0004-6361/202245410).

   *Context.* Light bridges are bright, long, and narrow features that are typically connected to the formation or decay processes of sunspots and pores.
   *Aims.* The interaction of magnetic fields and plasma flows is investigated in the trailing part of an active region, where pores and magnetic knots evolve into a complex sunspot. The goal is to identify the photospheric and chromospheric processes, which transform the mainly vertical magnetic fields of pores into a sunspot with multiple umbral cores, light bridges, and rudimentary penumbrae.
   *Methods.* Conducting observations with a broad variety of telescopes and instruments provides access to different atmospheric layers and the changing morphology of features connected to strong magnetic fields. While the Helioseismic and Magnetic Imager (HMI) of the Solar Dynamics Observatory (SDO) provides full-disk continuum images and line-of-sight magnetograms, the fine structure and flows around a pore can be deduced from high-resolution observations in various wavelengths as provided by the Goode Solar Telescope (GST) at the Big Bear Solar Observatory (BBSO). Horizontal proper motions are evaluated applying local correlation tracking (LCT) to the available time series, whereas the connectivity of sunspot features can be established using the background-subtracted activity maps (BaSAMs).
   *Results.* Photospheric flow maps indicate radial outflows, where the light bridge connects to the surrounding granulation, whereas inflows are present at the border of the pores. In contrast, the chromospheric flow maps show strong radial outflows at superpenumbral scales, even in the absence of a penumbra in the photosphere. The region in between the two polarities is characterized by expanding granules creating strong divergence centers. Variations in BaSAMs follow locations of significant and persistent changes in and around pores. The resulting maps indicate low variations along the light bridge, as well as thin hairlines connecting the light bridge to the pores and strong variations at the border of pores. Various BaSAMs demonstrate the interaction of pores with the surrounding supergranular cell. The H$\alpha$ line-of-sight velocity maps provide further insights into the flow structure, with twisted motions along some of the radial filaments around the pore with the light bridge. Furthermore, flows along filaments connecting the two polarities of the active region are pronounced in the line-of-sight velocity maps.
   *Conclusions.* The present observations reveal that even small-scale changes of plasma motions in and around pores are conducive to transform pores into sunspots. In addition, chromospheric counterparts of penumbral filaments appear much earlier than the penumbral filaments in the photosphere. Penumbra formation is aided by a stable magnetic feature that anchors the advection of magnetic flux and provides a connection to the surrounding supergranular cell, whereas continuously emerging flux and strong light bridges are counteragents that affect the appearance and complexity of sunspots and their penumbrae.

   **Author Contributions.** The individual contributions by the authors are listed according to the *Contributor Roles Taxonomy* (credit.niso.org). **R. Kamlah:** conceptualization, formal analysis, investigation, software, validation, visualization, and writing – original draft; **M. Verma:** funding acquisition, investigation, methodology, project administration, software, supervision, validation, visualization, and writing – review & editing; **C. Denker:** methodology, project administration, software, supervision, validation, visualization, and writing – review & editing; **H. Wang:** data acquisition, investigation, project administration, supervision, and writing – review & editing.

2. The second paper that covered the topic *Impact of Magnetic and Flow Fields on Penumbrae and Light Bridges of Three Leading Sunspots in an Active Region* was published in 2024 in the journal *Solar Physics* (DOI:10.1007/s11207-024-02386-9).

   This study investigates penumbrae and light bridges based on photospheric and chromospheric flow fields and photospheric magnetic fields in active region NOAA 13096. The improved High-resolution Fast Imager (HiFI+) and the GREGOR Infrared Spectrograph (GRIS) acquired high-resolution imaging and spectropolarimetric data at the 1.5-meter GREGOR solar telescope at the Observatorio del Teide, Izaña, Tenerife, Spain. Background-Subtracted Activity Maps (BaSAMs) have been used to locate areas of enhanced activity, Local Correlation Tracking (LCT) provides

horizontal proper motions, and near-infrared full-Stokes polarimetry offers access to magnetic fields and line-of-sight velocities. The results show that the decaying active region is characterized by a triangular region between the three leading, positive-polarity sunspots with unfavorable conditions for penumbra formation. This region has a spongy appearance in narrow-band H$\alpha$ images, shows signs of enhanced activity on small spatial scales, is free of divergence centers and exploding granules, lacks well-ordered horizontal flows, has low flow speeds, and is dominated by horizontal magnetic fields. Umbral cores are inactive, but the interface between pores and penumbral filaments often shows enhanced activity. Moat flows and superpenumbrae are almost always observed, when penumbral filaments are present, even in very small penumbral sectors. However, evidence of the moat flow can also be seen around pores, surviving longer than the decaying penumbral filaments. Light bridges have mainly umbral temperatures, reaching quiet-Sun temperatures in some places, show strong intensity variations, and exhibit weak photospheric horizontal flows, while narrow-band H$\alpha$ flow maps show substantial inflows.

**Author Contributions. R. Kamlah:** conceptualization, formal analysis, investigation, software, validation, visualization, and writing – original draft; **M. Verma:** conceptualization, formal analysis, funding acquisition, investigation, methodology, project administration, software, supervision, validation, visualization, and writing – review & editing; **C. Denker:** data curation, formal analysis, funding acquisition, investigation, methodology, project administration, software, supervision, validation, visualization, and writing – review & editing; **N. Huang:** investigation, and writing – review & editing; **J. Lee:** investigation, funding acquisition, project administration, supervision, and writing – review & editing; **H. Wang:** investigation, funding acquisition, project administration, supervision, and writing – review & editing.

3. The third article is currently under review for publication in the journal *Solar Physics* and covers the topic *Wide-field Image Restoration of G-band and Ca* II *K Images Containing Large and Complex Active Regions*.

   Restoration of solar images to achieve near diffraction-limited spatial resolution is commonly implemented on large-aperture solar telescopes. However, the extent of the restored field-of-view is typically only 100″ or even smaller. This study reports on wide-field image restoration of G-band and Ca II K images obtained with the 0.7-meter Vacuum Tower Telescope (VTT) at Observatorio del Teide, Tenerife, Spain. The Kiepenheuer Adaptive Optics System (KAOS) at the VTT provides a field-of-view with a diameter of 270″. Time series of datasets with 100 images were acquired with a large-format (7920×6004 pixels) CMOS imager at a frame rate of 30 Hz. An experimental optical setup that enabled wide-field imaging is briefly presented. Results from speckle-masking imaging and Multi-Frame Blind Deconvolution (MFBD) demonstrate the unique potential of the VTT for wide-field imaging. Power spectral analysis quantifies the instrument performance as a function of time and with distance from the lock point of the AO system. Further science capabilities are established using Local Correlation Tracking (LCT), Background-subtracted Solar Activity Maps (BaSAMs), and image quality/seeing metrics. In summary, commercial off-the-shelf camera systems can become an asset to sub-meter-class solar telescopes and open up new science opportunities at the interface between large-aperture and synoptic solar telescopes.

   **Author Contributions. R. Kamlah:** formal analysis, investigation, software, validation, visualization, and writing – original draft; **M. Verma:** formal analysis, investigation, project administration, software, supervision, validation, visualization, and writing – review & editing; **C. Denker:** conceptualization, data curation, formal analysis, investigation, project administration, software, supervision, validation, visualization, and writing – review & editing; **I. Kontogiannis:** investigation and writing – review & editing; **A. G. M. Pietrow:** investigation and writing – review & editing; **J. Rendtel:** investigation and writing – review & editing; **E. Lößnitz:** investigation and writing – review & editing; **A. Faryad:** investigation and writing – review & editing; **R. Volkmer:** project administration – review & editing; **R. Schlichenmaier:** project administration – review & editing; **T. Berkefeld:** resources – review & editing; **M. Esteves:** resources – review & editing; **O. Grassin:** resources – review & editing; **M. Roth:** project administration – review & editing

This doctoral research contributes to a more comprehensive understanding of the emergence, evolution, and decay of active regions and their corresponding features, including sunspots, pores, and light bridges. The analysis focused on the photosphere and chromosphere and incorporated a variety of analytical techniques. The combination of imaging and spectral data from ground-based and space-based telescopes enabled innovative data analysis, which permitted the intricate interactions between magnetic fields and plasma flows to be elucidated. The results of this work further expand our understanding of the dynamics of active region evolution and the influence of various features on flow motions and magnetic field structure within active regions and the connection to the surrounding regions.

# Chapter 1

# Introduction

The Sun, our closest star, provides access to a vital natural laboratory with a highly dynamic environment in which a wide range of magnetic and plasma phenomena are occurring and interacting at any given time. At the heart of these phenomena is the Sun's magnetic field. The magnetic field is responsible for a broad range of solar features, including the appearance of pores and sunspots on the solar surface, as well as large-scale solar eruptions that affect space weather. This thesis focuses on the magnetic features that result from the formation of magnetic flux tubes with high field strengths, such as pores and sunspots. The primary research is carried out in the two inner atmospheric layers of the Sun, i.e., the photosphere and the chromosphere, where these phenomena are observed using different observational facilities. Specifically, the work aims to investigate the processes that govern the structure, evolution, and decay of these magnetic features, with an emphasis on understanding the characteristic interaction between magnetic fields and plasma flows.

## 1.1 Historical Context and Recent Advances

The study of solar magnetic fields has a long and distinguished history, beginning with George Ellery Hale's seminal discovery of the magnetic nature of sunspots in 1908 (Hale 1908). This discovery, seen in the Zeeman broadening of spectral lines, established sunspots as regions of enhanced magnetic fields on the solar surface. Over the next century, our understanding of solar magnetism has advanced significantly, driven by both observational and theoretical developments, as well as advances in simulations (Leka and Steiner 2001; Cameron *et al.* 2007; Rempel *et al.* 2009b; Rempel, Schüssler, and Knölker 2009a; Cheung *et al.* 2010; Rempel and Schlichenmaier 2011; Rempel and Cheung 2014; Toriumi, Cheung, and Katsukawa 2015; Rempel 2015; Siu-Tapia *et al.* 2018; Panja, Cameron, and Solanki 2021).

In the early 20$^{th}$ century, the basic principles of the solar dynamo (Parker 1955) were established as the process theorized to be responsible for the generation of the Sun's magnetic field. However, it is the manifestation of this magnetic field in surface features such as sunspots and pores that has intrigued researchers and provided further insights into the nature of the solar magnetic dynamo.

Recent developments have further refined our understanding of the solar dynamo. Lefèvre and Clette (2011) supported the coexistence of a deep-rooted dynamo (Parker 1955) and a shallow or surface dynamo (e.g., Schatten 2009). Their conclusion was based on the low frequency of smaller sunspots in Solar Cycle 23. Cliver, White, and Richardson (2024) also suggested the existence of two different dynamo processes driving solar magnetism. The first is a large-scale cyclic dynamo that dominates magnetic activity during the solar maximum, which occurs over the course of an 11-year cycle (Hathaway 2010). This influences the Sun's magnetic field and the solar wind. The second is a small-scale turbulent dynamo that operates independently of the solar cycle. This process sets a baseline level of unsigned photospheric magnetic flux and solar wind magnetic field strength. This work highlights the complexity of solar magnetic processes and provides further insight for studies of how these dynamo-generated fields are translated into observable surface features and subsequently interact with higher atmospheric layers of the Sun. This work focuses mainly on the photospheric and chromospheric flows and magnetic fields of the pores and sunspots, with the aim of bridging the gap between theory and observations.

## 1.2 Magnetic Features in the Photosphere and Chromosphere

The photosphere, typically referred to as the surface of the Sun, is characterized by the granulation pattern resulting from the buoyant rise of hot plasma bubbles to the surface (e.g., Unsöld 1930; Richardson and Schwarzschild 1950; Stuart and Rush 1954). At the photospheric levels, the bubbles of rising plasma overturn and transport magnetic flux to their boundaries, i.e., to dark intergranular lanes. In addition to this concentration of magnetic flux along granulation boundaries, other visible manifestations of the underlying magnetic field on the surface include pores, sunspots, and associated structures such as umbral dots, umbral cores, light bridges, and penumbral filaments and grains. These features not only serve as indicators of the magnetic processes at work, but also have a significant influence on the solar atmosphere.

### 1.2.1 Active Regions

Active regions on the Sun are defined as extended areas of concentrated magnetic flux emanating from the Sun in the form of rising magnetic flux tubes. These regions vary widely in size and complexity, ranging from simple unipolar pores or sunspots to large, complex bipolar active regions composed of a multitude of pores and sunspots. The magnetic fields of active regions are extended and dispersed (e.g., van Driel-Gesztelyi and Green 2015). Bipolar active regions, formed by the emergence of a Ω-loop rising through the photosphere, show a separation of opposite polarities during the emergence phase, while no strong motions with respect to the surrounding plasma are found during the passive phase (Švanda, Klvaňa, and Sobotka 2009). The growth of magnetic surface features can be sustained by the continuous addition of magnetic flux from the surroundings (Wang and Zirin 1992). Expanding granules are often observed between opposite polarities within the emerging active regions (Bonet *et al.* 2005; Verma *et al.* 2012; Kamlah *et al.* 2023). Active regions can persist for several weeks, during which a constant emergence and decay of individual features can be observed. Furthermore, the lifetimes, dimensions, and magnetic field strengths of these features exhibit considerable variations. Several reviews summarized the various stages of active region evolution (e.g., Bray and Loughhead 1964; Schrijver and Zwaan 2000; van Driel-Gesztelyi and Green 2015).

### 1.2.2 Sunspots

Sunspots represent one of the most conspicuous magnetic features in active regions, which persist for a period of days to several weeks (Bumba 1963; Tlatov 2023). In particular, the emergence of sunspots, which is a consequence of processes occurring below the surface of the Sun (Parker 1955), remains a topic of considerable uncertainty. Sunspots are characterized by their dark appearance in the photosphere, which is a consequence of the suppression of convective heat transport by concentrations of strong magnetic fields. The dark umbra is surrounded by a lighter penumbra. Jahn and Schmidt (1994) reported a reduced heat flux of 25% concerning the penumbra and 77% for the umbra, which corresponds to effective temperatures of 5777 K, 5275 K, and 4000 K regarding the quiet Sun, penumbra, and umbra, respectively. They typically have diameters between 10 Mm and 50 Mm with magnetic field strengths ranging from 1.8 kG to 3.7 kG (Livingston 2002). However, observations have also been made of even larger field strengths (Wang *et al.* 2018a). The magnetic field of the umbra is predominantly vertical, whereas the magnetic fields within the penumbra are inclined at approximately 70° with respect to the surface normal (Rucklidge, Schmidt, and Weiss 1995). The outer penumbra exhibits field strengths on the order of 600 – 1800 G (Livingston 2002).

In addition to sunspots, emerging flux tubes can also lead to the formation of pores, which are smaller magnetic features. The main distinguishing characteristic between pores and sunspots is the absence of a penumbra (Rucklidge, Schmidt, and Weiss 1995; Leka and Skumanich 1998). In addition, pores have shorter lifetimes and weaker magnetic fields, typically in the range of 600 G – 1.8 kG (Sütterlin 1998; Verma and Denker 2014). In general, photospheric features include magnetic knots (Leka and Steiner 2001). These manifest as granule-sized dark patches (Beckers and Schröter 1968), typically with diameters on the order of 2″, with an intensity that is 30% less than the surrounding quiet Sun (Abdusamatov and Krat 1969). The field strength of magnetic knots can be relatively weak, with values ranging from several 100 G to 1 kG (Frazier and Stenflo 1978; Solanki 1993).

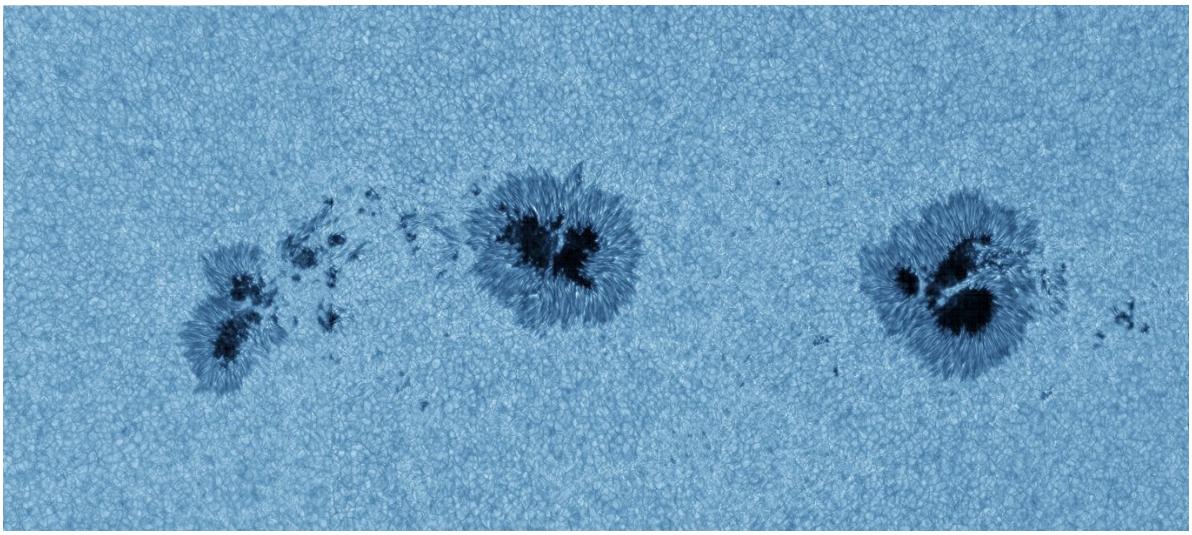

**Figure 1.1** False-color mosaic of three speckle-restored G-band images obtained at the VTT on 2016 July 19. The FOV covers of about $310'' \times 140''$ and includes multiple pores and sunspots in active regions NOAA 12567 and 12565. The fine structure includes rudimentary penumbra, light bridges, umbral cores, umbral dots, and penumbral grains and filaments. Image credit: Carsten Denker (AIP).

All magnetic features observed in the photosphere show a canopy effect in higher atmospheric layers as a consequence of the changing plasma $\beta$. This parameter, defined as the ratio of plasma pressure to magnetic pressure, undergoes significant changes at photospheric heights. Below the photosphere, the motion of the magnetic flux is primarily controlled by the surrounding plasma. However, at the photosphere and in higher layers such as the chromosphere and above, the motion of the plasma must align with the magnetic field lines. This way previously confined magnetic flux concentrations extend in a canopy structure after penetrating the photosphere. However, many questions about these prominent features remain unanswered. The evolution of these features is subject to considerable variations, and the processes governing their formation and decay remain poorly understood.

### Penumbra

The penumbra is a complex structure consisting of elongated light and dark filaments as well as penumbral grains (e.g., Schlichenmaier, Jahn, and Schmidt 1998; Sobotka, Brandt, and Simon 1999; Verma, Kummerow, and Denker 2018a) with spatial scales of about $0.1''$ in the inner penumbra (Scharmer *et al.* 2002) and $0.35''$ in the middle and outer penumbra (Sütterlin 2001). The appearance of the penumbra in both the photosphere and the chromosphere indicates that dynamic processes are at work, driven by the influence of magnetic fields. In the photosphere, the penumbra is characterized by "uncombed" magnetic fields with different angles of inclination. Many studies have shown that the formation of inclined photospheric magnetic field lines is a consequence of the shifting of chromospheric field lines, which typically have inclinations of $40° - 80°$ down to the photosphere (Shimizu, Ichimoto, and Suematsu 2012; Romano *et al.* 2013, 2014; Murabito *et al.* 2016; Romano *et al.* 2020). Penumbrae can manifest either as fully formed or as so-called rudimentary penumbrae (Watanabe, Kitai, and Otsuji 2014). Examples of a rudimentary penumbra and a fully formed penumbra are shown in Figure 1.1. Penumbra formation typically occurs over a relatively short time, lasting between one and ten hours (e.g., Schlichenmaier *et al.* 2010b; Murabito *et al.* 2018). Keil *et al.* (1999) pointed out that the formation of a penumbra can be initiated by the disturbance caused by exploding granules. This formation can be completed rapidly within a few minutes (Leka and Skumanich 1998; Yang *et al.* 2003). However, penumbra formation generally does not occur in the central region where sunspots of the same polarity face each other (Künzel 1969; Verma 2018; Murabito *et al.* 2021). This is due to the predominantly vertical magnetic fields at these locations, where the canopy effect prevents sufficient inclination angles for penumbra formation (Lindner *et al.* 2023). In the chromosphere, the structure encircling sunspots is referred to as superpenumbra (Loughhead 1968; Peter 1996; Jing *et al.* 2019) and displays a more intricate and multi-layered configuration. These contain

thin, dark, and slightly curved individual fibrils or filaments radiating outward from a sunspot, with variable lengths and widths of less than 1″.

A statistical study by Balasubramaniam, Pevtsov, and Rogers (2004) found the average length of the fibrils to be about 43 Mm, with only slight curvatures of 5 Mm observed in rotating sunspots. The lifetime of individual superpenumbral filaments can vary from a few to tens of minutes, but the global structure remains stable for longer periods. Tsiropoula *et al.* (1997) observed that the lifetimes of these filaments vary with their length. The longest fibrils were observed to have lifetimes ranging from one to twenty minutes, with varying visibility. However, an average appearance was defined by orientation, average darkness, and length, which can be preserved for up to hours. Furthermore, chromospheric superpenumbral filaments appear to form even in the absence of counterparts in the photosphere (Kamlah *et al.* 2023). Schad *et al.* (2015) found a decrease in magnetic field strength from nearly 1500 G in the umbra of a sunspot to 100 – 300 G within the superpenumbral canopy. It is currently unclear if fibrils are caused by thermal perturbations or density perturbations. In addition, the lack of information about their origin in the photosphere poses a significant challenge to the analysis of superpenumbral fibrils. In early observations of superpenumbra, vortex motions were reported (Hale 1925, 1927; Richardson 1941). Peter (1996) derived a set of MHD equations to determine the velocity field around sunspots that could reproduce these vortex motions. He concluded that the winding of spirals occurs exclusively at radii larger than 10 000 km, increases with size and also with heliographic latitude, and is largely determined by solar rotation, but independent of polarity.

### Light bridges

The dark umbra of the sunspot is not completely devoid of features. It contains ubiquitous bright umbral dots (Sobotka, Bonet, and Vazquez 1993). Other features seen in the umbra are light bridges, which are bright features that cross or penetrate the umbra. These are often observed during the formation of sunspots or as precursors to their subsequent decay. In the photosphere, light bridges are narrow, elongated, and bright regions that divide the umbra into separate sections. They have been classified as granular light bridges as shown in Figure 1.2 (Lites *et al.* 1991; Rouppe van der Voort, Bellot Rubio, and Ortiz 2010; Lagg *et al.* 2014), faint light bridges (Lites *et al.* 1991; Sobotka and Puschmann 2009), or strong light bridges (Rimmele 2008; Rezaei, Bello González, and Schlichenmaier 2012). It is hypothesized that light bridges result from the intrusion of convective flows into the magnetic field of the sunspot at a certain depth, which are subsequently transported to the surface by upflows, as demonstrated in simulations by Panja, Cameron, and Solanki (2021). The merging of umbral cores can lead to the formation of light bridges between these features (Toriumi, Cheung, and Katsukawa 2015; Li *et al.* 2021). These different formation mechanisms can lead to the formation of narrow light bridges that are more like penumbral filaments (Louis *et al.* 2008; Rimmele 2008; Bharti 2015; Hou *et al.* 2020) and granular light bridges (Sobotka *et al.* 2013; Lagg *et al.* 2014). Consequently, light bridges and umbra should be considered as two discrete systems due to their different characteristics and the local weakening of the magnetic field as well as the more inclined orientation with respect to the surrounding umbra (Jurčák,

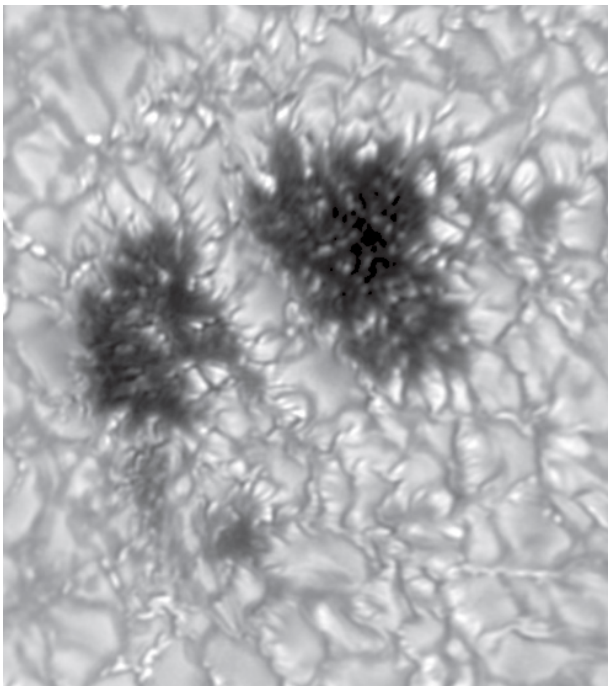

**Figure 1.2** Two umbral cores, which are separated by a granular light bridge, were observed with the GST at BBSO at 19:00 UT on 2015 April 1. The pores were located in the trailing positive-polarity part of NOAA 12317. This speckle restored TiO $\lambda$706 nm image covers a FOV of approximately 15″ × 20″. Image credit: see Figure 2 in Kamlah *et al.* (2023).

Martínez Pillet, and Sobotka 2006; Katsukawa *et al.* 2007; Lagg *et al.* 2014; Liu and Liu 2015; Felipe *et al.* 2016).

In a recent study, Jing *et al.* (2023) emphasized that the appearance of light bridges depends on the magnetic properties and on the degree of compression exerted by the surrounding environment. However, Lagg *et al.* (2014) considered a granular light bridge as a field-free region, suggesting that it was formed by convection with properties similar to those of solar granules. In the chromosphere, light bridges extend in a canopy-like structure that connects with the surrounding region. However, the formation processes and magnetic properties of light bridges remain a subject of ongoing investigation. Furthermore, studies associating the formation of light bridges with intruding umbral dots have also linked them to plasma ejections or chromospheric H$\alpha$ surges along the light bridge (Roy 1973; Bharti, Joshi, and Jaaffrey 2007; Pietrow *et al.* 2022). This evidence suggests that they may also be a potential contributor to chromospheric heating. Louis (2015) observed flux emergence in the light bridge in the form of photospheric blue- and redshifts. They surmised that the rising loop in the light bridge was confined in the lower atmosphere by the overlying sunspot canopy resulting in temperature enhancement in the upper photosphere and lower chromosphere. A similar scenario of light bridge formation in a rising flux region was presented in Toriumi, Cheung, and Katsukawa (2015), demonstrating the interplay between magnetic fields and convective motions within the light bridge.

## 1.3 Magnetic and Flow Structure of Sunspots and Pores

The magnetic and flow structures in and around sunspots and pores are complex and have been the subject of extensive observational studies (Zwaan 1985; Hirzberger *et al.* 2005; Balasubramaniam, Pevtsov, and Olmschenk 2008; Balthasar and Gömöry 2008; Verma *et al.* 2016a; Bharti *et al.* 2016; Joshi *et al.* 2017; Verma, Kummerow, and Denker 2018a) and theoretical research (Leka and Steiner 2001; Cameron *et al.* 2007; Rempel and Cheung 2014; Rempel 2015; Panja, Cameron, and Solanki 2021). Observations with advanced ground-based solar telescopes, such as the 1.5-meter GREGOR Solar Telescope (Schmidt *et al.* 2012; Kleint *et al.* 2020), the 1.6-meter Goode Solar Telescope (GST, Cao *et al.* 2010b), the 0.7-meter Vacuum Tower Telescope (VTT, von der Lühe 1998), the 4-meter Daniel K. Inouye Solar Telescope (DKIST, Rimmele *et al.* 2020), among others, along with space-based observations from satellites, such as the Solar Dynamics Observatory (SDO, Pesnell, Thompson, and Chamberlin 2012) or the Hinode Solar Optical Telescope (SOT, Tsuneta *et al.* 2008), have provided high-resolution images and spectra of these structures, revealing details that have improved our understanding of the Sun's small-scale processes and have enabled validating theoretical models.

The Evershed effect, an inherent characteristic of a sunspot's penumbra at photospheric levels, was first observed by Evershed (1909). This effect describes a radial outflow of plasma along the penumbral filaments with observed velocities of $1-6$ km s$^{-1}$ (Sheeley 1972; Molowny-Horas 1994; Márquez, Sánchez Almeida, and Bonet 2006; Scharmer *et al.* 2013; Verma *et al.* 2018b; Wang *et al.* 2018b) and $1-4$ km s$^{-1}$ as seen in simulations (Kitiashvili *et al.* 2009; Rempel 2015). Furthermore, this radial flow motion is associated with a small upward component in the inner penumbra and a small downward component in the outer penumbra (Schlichenmaier and Schmidt 2000; Schmidt and Schlichenmaier 2000; Tritschler *et al.* 2004; Langhans *et al.* 2005), whereby radially oriented up- and downflows can coexist on small scales (Sainz Dalda and Bellot Rubio 2008; Franz and Schlichenmaier 2010). This flow is driven by a combination of magnetic and pressure forces, with the plasma following magnetic field lines as they fan out from the sunspot (Thomas *et al.* 2002; Weiss *et al.* 2004; Brummell *et al.* 2008). Recent observations have shown that the Evershed flow is initiated when the magnetic field strength reaches a critical point, where it is strong enough to bend the magnetic field lines to the point where they dip below the photosphere again, thereby initiating magnetoconvection (Murabito *et al.* 2016). Observations have revealed the existence of a divergent region in the middle of the penumbra, with inflows in the inner part and outflows in the outer part (Deng *et al.* 2007; Verma and Denker 2011).

In the chromosphere, the surroundings of sunspots are typically characterized by a reverse flow towards the sunspot, called the inverse Evershed effect (Moore and Rabin 1985; Beck, Choudhary, and Ranganathan 2020; Beck and Choudhary 2020). Despite the implications of the nomenclature, this phenomenon is not related to the Evershed effect observed in the photosphere and begins at a height of

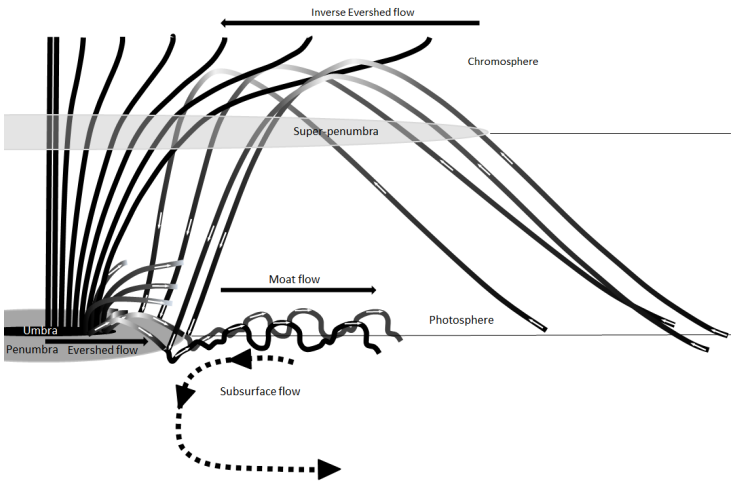


**Figure 1.3** Schematic view of the flows and motions connected to sunspots. Initially vertical magnetic field lines extend from the umbra (*black*) in the photosphere to a canopy structure at higher atmospheric layers. The umbra is surrounded by the penumbra (*grey*), in which magnetic field lines are more inclined and the Evershed flow transports material and magnetic features radially outward. At the periphery of the penumbra, the moat region starts, where material is transported by the moat flow towards the supergranular boundary. Consecutively, material is lifted into the chromosphere and transported towards the umbra by the inverse Evershed effect, thereby forming the superpenumbra. The material subsequently drains towards the penumbra.

about 500 km above the solar surface (Boerner and Kneer 1992). The chromospheric inverse Evershed effect describes a radial structure surrounding sunspots in which material is lifted from the supergranular boundaries at photospheric heights into the chromosphere, where it flows back towards the sunspot at velocities of 3 – 15 km $s^{-1}$ (Choudhary and Beck 2018; Jing *et al.* 2019). Subsequently, the inward motion transforms into downflows at the umbral boundaries. The driving mechanism of the inverse Evershed effect is a siphon flow along individual magnetic flux tubes (Meyer and Schmidt 1968). Another common chromospheric feature of sunspots are running penumbral waves (Sobotka *et al.* 2013; Freij *et al.* 2014). These upward propagating magneto-acoustic waves are guided by the inclined magnetic field of the penumbra (Jess *et al.* 2013) and run mainly from the inner to the outer penumbra boundaries (Giovanelli 1972; Zirin and Stein 1972).

At the photospheric level, a second flow structure known as the moat flow (Vargas Domínguez *et al.* 2008; Löhner-Böttcher and Schlichenmaier 2013; Rempel 2015) is observed which encircles the sunspots. This flow motion was first reported by Sheeley (1969) who tracked photospheric bright points, which were later identified as moving magnetic features (MMF, Harvey and Harvey 1973). This horizontal radial flow connects the outer penumbra (Rempel 2015) to its surroundings and extends to the supergranular network (Vargas Domínguez *et al.* 2008; Verma, Kummerow, and Denker 2018a). The moat flow can extend several times the radius of the sunspot, with typical values in the range of 4 Mm to 20 Mm (Sheeley 1972; Brickhouse and Labonte 1988; Balthasar and Muglach 2010; Löhner-Böttcher and Schlichenmaier 2013; Verma, Kummerow, and Denker 2018a; Strecker and Bello González 2018), where the flow field is axially symmetric around sunspots with a fully developed penumbra (Löhner-Böttcher and Schlichenmaier 2013). However, a significant east-west asymmetry has been reported as a consequence of the relative motion of the sunspot with respect to its environment (Verma, Kummerow, and Denker 2018a). This is in contrast to supergranular flows, which are radially symmetric (Švanda, Sobotka, and Bárta 2014). In addition, (Švanda, Sobotka, and Bárta 2014) described the moat cell as a downflow region, in contrast to supergranules, which are characterized by an upflow–downflow behavior. In addition, the tilt angle of the active region and the presence of plage in its vicinity can also modify this asymmetry. Another suggestion is that supergranules have characteristic convective flow patterns that contribute to the modulation of the magnetic field distribution around sunspots, thereby generating large-scale phenomena such as the observed moat flow. This link suggests that sunspots and supergranular flows are part of a larger magnetic and convective system that regulates the dynamics of the sunspot's evolution. The moat flow intensifies if the active region is centered in its supergranule, with typical velocities ranging from 0.5 km $s^{-1}$ to 1.2 km $s^{-1}$ (Sheeley 1972; Löhner-Böttcher and Schlichenmaier 2013; Strecker and Bello González 2018; Kamlah *et al.* 2024).

Along with the typical large-scale outward moat flow, the presence of inward horizontal flows towards umbral cores (Sankarasubramanian and Rimmele 2003; Sobotka *et al.* 2012) has been observed, which convert to downward flows at the borders of strong magnetic features such as pores (Haugen 1969; Roudier, Bonet, and Sobotka 2002; Hirzberger 2003; Guglielmino and Zuccarello 2011; Verma and Denker 2014; Chae *et al.* 2015; Kamlah *et al.* 2023). These inflows are driven by the strong magnetic

field gradients in these regions. Furthermore, observations have revealed the transport of plasma and small-scale magnetic features from the surrounding area towards the sunspot or pore boundary (Brants and Steenbeek 1985; Stein *et al.* 2011).

Figure 1.3 summarizes the main magnetic and flow structures around sunspots. It schematically illustrates the photospheric and chromospheric flows and magnetic field lines associated with a sunspot. Note that the image is not to scale. From the umbra (black region), vertical magnetic fields extend into the canopy structure after penetrating the photosphere. The surrounding penumbra (gray region) is characterized by the Evershed flow. This is a radially outward flow along penumbral filaments, in the inner penumbra, and downflows in the outer penumbra. Outside the penumbra, a decrease in velocity marks the onset of the moat flow, along which plasma and magnetic features are transported to the supergranular boundary, where the sunspot is typically centered. At the supergranular boundary, the material is lifted into the chromosphere and flows back to the penumbral boundary along the superpenumbra where the characteristic inverse Evershed effect occurs. At the penumbral boundary, the upflows become downflows. The extent of the penumbra and superpenumbra is also shown in the sketch.

## 1.4 Comparison between Observations and Simulations

Advances in observational capabilities have facilitated a more detailed understanding of both small- and large-scale solar processes, aided by advances in magnetohydrodynamics (MHD) simulations (Cameron *et al.* 2007; Nordlund, Stein, and Asplund 2009; Rempel, Schüssler, and Knölker 2009a; Cheung *et al.* 2010; Rempel and Schlichenmaier 2011; Siu-Tapia *et al.* 2018; Panja, Cameron, and Solanki 2021). However, discrepancies between observations and theoretical models remain unresolved. One of the important discrepancies is related to the flows in the penumbra. While it is possible to resolve individual filaments, the inherent turbulence within these filaments cannot be resolved. In contrast to turbulent flows, MHD simulations use laminar flows. Another limitation is the form of initialization, which is rather arbitrary (Rempel and Schlichenmaier 2011), so self-consistent simulations of sunspot formation are not feasible. Furthermore, the Evershed flow can be simulated with a peak velocity close to $\tau = 1$, followed by a rapid decrease. This contradicts the results of Rimmele (1995) and Stanchfield, Thomas, and Lites (1997). However, bisector analysis of the spectral data indicates the presence of outflows that decrease with height (Schlichenmaier, Bellot Rubio, and Tritschler 2004; Bellot Rubio, Schlichenmaier, and Tritschler 2006).

In particular, the formation of the penumbra cannot be adequately simulated due to the insufficient grid resolution used for the flux emergence simulation. An artificial upscaling of the magnetic field strength during the simulation is required to achieve sufficient flux concentrations as demonstrated by (Stein *et al.* 2012). In addition, an artificial increase in the magnetic field inclination at the upper boundary is required to produce an extended penumbra as demonstrated by (Rempel 2011). The much longer time- and spatial scales involved in sunspot evolution make obtaining realistic MHD simulations much more challenging than obtaining realistic MHD simulations on granular scales. The latter facilitates comparison with high-resolution observations (e.g., Nordlund, Stein, and Asplund 2009). However, the aforementioned observed flow patterns around sunspots, such as the inward flows at their borders and the detailed structure and flow of the penumbral filaments, are not fully consistent with the MHD simulations. Due to the high computational cost, another limitation of current simulations is that chromospheric or even coronal processes are not adequately considered. Consequently, only the buoyant rise is modeled, with the effects of convection either absent or represented in a simplified manner (Tortosa-Andreu and Moreno-Insertis 2009). These limitations highlight the complex interplay between magnetic fields and plasma flows associated with sunspots, which cannot be fully reproduced even with current mathematical and computational advances. Observations are reaching unprecedented resolution and revealing further details of the complex interaction between plasma and magnetic fields. To improve our understanding of small-scale features as well as the global structure of sunspots, a holistic approach combining high-resolution and synoptic observations with simulation is needed.

Some of the issues raised and addressed in this work regarding plasma and magnetic field interactions are listed in this box.

- What are the characteristics of typical plasma flows, such as Evershed and moat flow, and how are they connected to penumbral filaments? Is the presence of a penumbra a prerequisite for these flows? Where do these flows terminate?
- How do penumbral filaments form and stabilize in sunspots?
- What is the role of the magnetic field of the surroundings in the formation, evolution, and decay of the penumbra? Is the formation of the penumbra a prerequisite for the formation of the superpenumbra, or vice versa?
- How do magnetic and flow fields interact at the borders of pores across the photosphere and chromosphere, and what are the typical flows between opposite polarity features?
- Is the interaction of pores and subsequently sunspots with the surrounding supergranular cell a prerequisite for penumbra formation?
- How do light bridges influence the formation or decay of a penumbra, and how do their physical properties (temperature, magnetic field, and plasma flows) evolve during sunspot evolution?
- How does the weakening of the magnetic field in light bridges lead to field-free regions, and how does the low-lying magnetic canopy over light bridges affect the umbral magnetic field and plasma flows?
- Why do chromospheric flows sometimes align with the magnetic field and sometimes not?

## 1.5 Instruments

### 1.5.1 Goode Solar Telescope

The GST (Cao *et al.* 2010b), operated by the New Jersey Institute of Technology (NJIT), is part of the Big Bear Solar Observatory (BBSO) in California, USA. The all-reflecting, off-axis Gregory system provides the opportunity for state-of-the-art solar observing capabilities using six facility-class scientific instruments, installed at different telescope foci. The GST has a 1.6-meter clear aperture and a parabolic primary mirror made of Zerodur that reflects the incoming light beam to the primary focus field stop and the heat reflector (heat-stop). The heat-stop has a 120″ circular opening. This provides an observable square FOV of $80'' \times 80''$. The secondary mirror is elliptical and redirects the incoming beam towards the diagonal flats M3, M4, and M5.

**Figure 1.4** The 1.6-meter GST at the BBSO in Big Bear Lake, California, USA. Image credit: cuna.nso.edu

The Broad-band Filter Imager (BFI, Cao *et al.* 2010b) is set up at the Nasmyth focus and enables high spatial resolution photometry in TiO $\lambda$706 nm, H$\alpha$ $\lambda$656 nm, G-band $\lambda$430 nm, and the near-infrared (NIR). The BFI uses 14-bit pco.2000 CCD cameras with $2048 \times 2048$ pixels to capture bursts of 100 images every 15 s to 30 s, from which the best 70 images are kept. Post-facto speckle masking image restoration (Wöger and von der Lühe 2008) provides data quality that approaches the diffraction limit, i.e., 0.09″ at TiO. In addition, G-band observations are possible. The observation of spectral lines at different wavelengths

is carried by the Visible Imaging Spectrograph (VIS, Varsik *et al.* 2014). This narrow-band imaging spectrometer is based on a Fabry-Pérot etalon that has a bandpass of 0.007 nm over a FOV of 70″. The VIS is equipped with a CCD camera with 2048×2048 pixels and is capable of observations with a cadence of 10 s. Spectral lines observable with this setup are H$\alpha$, Fe I $\lambda$630 nm, and Na I $D_2$ $\lambda$589 nm. Longer exposure times are required for observations in the line wings due to narrow-band interference filters, which serve as order sorters for the Fabry-Pérot etalon. Thus, the number of photons are reduced in the lines wings, which counterintuitively leads to longer exposure times in the line wings as compared to the line core. Therefore, wing observations are the determining factor in cadence.

Additional instruments are the InfraRed Imaging Magnetograph (IRIM, Cao *et al.* 2012), the Visible Imaging Magnetograph (VIM), the Fast Imaging Solar Spectrograph (FISS, Chae *et al.* 2013), and the CrYogenic solar spectrogRAph (CYRA, Yang *et al.* 2020). Real-time image correction is achieved by the adaptive optics system (AO). The AO-308 system (Shumko *et al.* 2014) consists of a deformable mirror (DM) with 349 actuators, a wavefront sensor (WFS) with 308 sub-apertures, a fast camera, an new-generation high-speed digital signal processors.

### 1.5.2 GREGOR Solar Telescope

The 1.5-meter GREGOR solar telescope, located at the Observatory del Teide (OT), Izaña, Tenerife, Spain, started routine observations in 2012 (Schmidt *et al.* 2012; Kleint *et al.* 2020). The GREGOR solar telescope features a 1.5-meter aperture and forms a powerful observational alliance with the neighboring 0.7-meter VTT (von der Lühe 1998). GREGOR is operated by a German consortium, led by the Institut für Sonnenphysik (KIS) in Freiburg, together with the Leibniz-Institut für Astrophysik Potsdam (AIP), and the Max-Planck-Institut für Sonnensystemforschung (MPS) in Göttingen. The Institut für Astrophysik of Göttingen Universität was a member until 2008. Other international partners are the Instituto de Astrofísica de Canarias (IAC) and the Astronomical Institute of the Academy of Sciences of the Czech Republic (ASU).

The GREGOR adaptive optics system (GAOS, Berkefeld *et al.* 2012) provides real-time image correction using a tip-tilt mirror and a DM, which enables diffraction limited observations in a central radius of approximately 5 – 10″, depending on local seeing conditions and the observed wavelength. A spatial resolution of up to 50 km at 400 nm on the solar surface can be achieved. GREGOR is equipped with mechano-optical elements for polarimetric calibration enabling precise measurements of the solar magnetic field and plasma motions in the photosphere and chromosphere. GREGOR does not follow the typical design of a vacuum telescope. Instead, an open construction design is used, where wind flushing avoids the major degradation caused by ground seeing. This open design became necessary due to the technical limitations of entrance windows. The thickness required for entrance windows larger than 1 m would have caused a significant degradation in transmission, in addition to birefringence effects, and therefore would have negatively affected the polarimetric characteristics.

**Figure 1.5** The 1.5-meter solar telescope GREGOR at the OT, Izaña, Tenerife, Spain with closed tent dome.

A foldable tent dome (Hammerschlag *et al.* 2012) is used to protect the telescope and the main mirror. GREGOR is a double Gregory system with three imaging mirrors. The 1.5-meter main mirror, made of Zerodur, requires active cooling from the rear (Schmidt *et al.* 2012; Soltau *et al.* 2012). The incoming beam is reflected to the elliptical M2, and M3, which eventually form the science beam. This final image is directed by folding mirrors into the optical laboratory located one floor below the telescope

and distributed to the desired instruments. The two instruments currently used for routine scientific observations, the improved High-resolution Fast Imager (HiFI+, Denker *et al.* 2023a) and the GREGOR infrared spectrograph (GRIS, Collados *et al.* 2012), are described in below. The image processing and restoration techniques, which are required to process and evaluate the HiFI+ data, are provided by the "sTools" data processing pipeline (Kuckein *et al.* 2018).

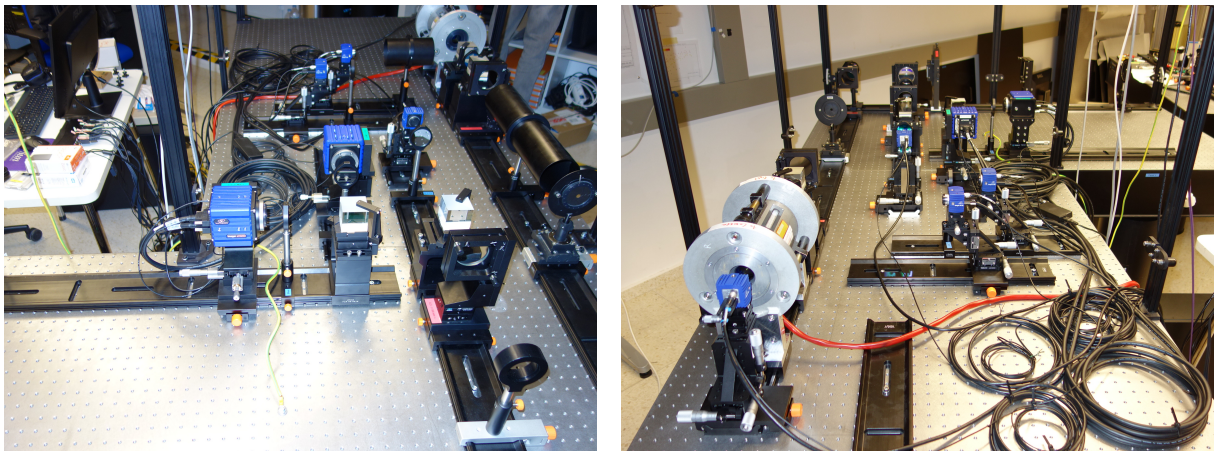

**Figure 1.6** The red imaging channel (*left*) includes an H$\alpha$ Lyot filter and three Imager M-lite 2M cameras. The blue imaging channel (*right*) includes two Imager sCMOS cameras (*foreground*) and one of the Imager M-lite 2M cameras (*background*). Image credit: Carsten Denker (AIP).

The multi-wavelength imaging filtergraph HiFI+ (Denker *et al.* 2023a) had its science verification in April 2022, after which it has been used for routine observations. This new system upgrades the former High-resolution Fast Imager (Denker *et al.* 2018b), which enabled synchronized high-resolution, high-cadence observations in two channels. The new setup has been expanded to six cameras operated by three camera control computers. Two of the channels use Imager sCMOS cameras, while the remaining four channels are equipped with Imager M-lite 2M CMOS cameras, all controlled by the DaVis control software from LaVision GmbH in Göttingen, Germany. The HiFI+ system observes in six channels featuring various spectral filters, enabling synchronized high-cadence observations over a wide spectral range. HiFI+1 consists of two Imager sCMOS cameras with a detector size of $2560 \times 2160$ pixels, where each pixel has a size of 6.5 $\mu$m $\times$ 6.5 $\mu$m with an image scale of 0.028″ pixel$^{-1}$, covering a FOV of $71.6'' \times 60.5''$. The data are recorded at a frame rate of 49 Hz, corresponding to a cadence of 12 s, which includes some overhead for saving the data. Cameras 1 and 2 observe in the G-band $\lambda_1 = 450.5$ nm and in the blue continuum $\lambda_2 = 430.7$ nm, respectively. HiFI+2 and HiFI+3 feature Imager M-lite 2M cameras with a detector size of $1936 \times 1216$ pixels, where each pixel has a size of 5.86 $\mu$m $\times$ 5.86 $\mu$m. Both detectors of HiFI+2 have an image scale of 0.05″ pixel$^{-1}$ for capturing images in H$\alpha$ narrow band $\lambda_3 = 656.3$ nm and broad band $\lambda_4 = 656.7$ nm. HiFI+3 uses the same image scale of 0.05″ pixel$^{-1}$ for TiO $\lambda_5 = 705.8$ nm observations, while the Ca II H $\lambda_6 = 396.8$ nm channel has an image scale of 0.025″ pixel$^{-1}$. Only the Ca II channel uses the full detector size of $1936 \times 1216$ pixels, corresponding to a FOV of $48.4'' \times 30.4''$. The remaining three channels are limited to $1536 \times 1216$ pixels, corresponding to a FOV of $76.8'' \times 60.8''$. HiFI+2 and HiFI+3 record data at a frame rate of 100 Hz, corresponding to a cadence of 6 s, which again includes some overhead for saving the data. From a recorded burst of 500 images, only the best 100 images are stored as flexible image transport system (FITS, Wells, Greisen, and Harten 1981; Hanisch *et al.* 2001) data using FITS image extensions (Ponz, Thompson, and Munoz 1994). These data are available for further analysis by the principal investigators and their team. In general, all data become available after an embargo period of one year.

One of the first-light instruments of the GREGOR solar telescope is the GRIS (Collados *et al.* 2012), a slit-spectrograph capable of full Stokes vector polarimetry. It has undergone various updates most recently in 2022 (Regalado Olivares *et al.* 2022; Quintero Noda *et al.* 2022b) adding a new spectral channel that receives light below 900 nm to the already existing channel which takes regular spectropolarimetric observations in 1000 – 1800 nm and only spectroscopic observations in the 2000 – 2300 nm band.

The original light path of the GRIS instrument receiving light from 1000 – 2300 nm is maintained and labeled channel 1. The new channel 2 works as a baseline at 854 nm. Light with a wavelength shorter

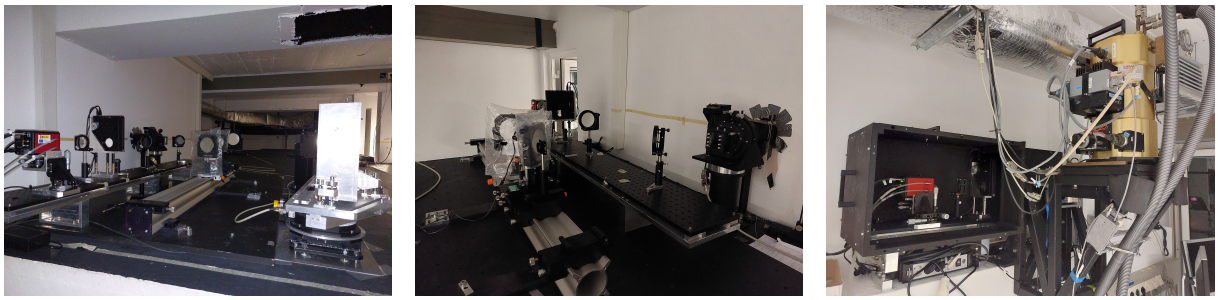

**Figure 1.7** Two views of the GRIS setup (*left and middle*) on the optical bench in the optical laboratory in the 4$^{th}$ floor of the GREGOR building. The cryostat and the camera system (*right*) are located in a separate room outside the laboratory, where the electronics cannot provide a heat load inside the laboratory.

than 900 nm is directed by a dichroic beamsplitter behind a collimator lens of the reimaging system. The desired spectral range is narrowed with a filter wheel in the beam path. A further channel 3 will be dedicated to observe wavelengths below 800 nm. The spectral and spatial information is matched between the channels using $2304 \times 2304$ pixel Hamamatsu Orca Fusion BT sensors. A re-imaging lens system located in front of the sensor produces a pixel scale that matches the original GRIS channel (channel 1), enabling observations with a spatial sampling of 0.135″ pixel$^{-1}$. Observations can be performed in long-slit or Integral Field Unit (IFU, Vega Reyes *et al.* 2016; Dominguez-Tagle *et al.* 2022) mode. The IFU mode was added in 2018 enabling simultaneous spectro-polarimetry of a two-dimensional FOV and the spectral region of interest. Both spectral windows of GRIS contain various lines sensitive to the photosphere (e.g., Si I $\lambda$1082.7 nm, Ca I $\lambda$1083.9 nm) and chromosphere (e.g., He I triplet $\lambda$1083.0 nm, Ca I $\lambda$854.2 nm) enaling simultaneous observations of different layers of the Sun.

### 1.5.3 Vacuum Tower Telescope

Another facility at the OT, next to GREGOR, is the VTT. The telescope consists of two 0.8-meter Celoestat mirrors and a spherical 0.7-meter main mirror installed in an off-axis configuration inside the vacuum tank. The focal length of the 0.7-meter mirror is 45.64 m, providing an image scale of 4.52″ mm$^{-1}$ at the primary focus. This potentially enables observations of a FOV of 600″ if a detector is placed at this location. Real-time image correction is enabled by the Kiepenheuer Adaptive Optics System (KAOS, von der Lühe *et al.* 2003; Berkefeld *et al.* 2010).

The VTT has an Echelle spectrograph with a grating that has 79 grooves mm$^{-1}$ and achieves a spectral resolution of 0.6 pm at 500 nm. The blaze angle is typically in the order of 63°. The rotation of the grating can be adjusted depending on the spectral line selection. The slit size is typically 80 $\mu$m, corresponding to 0.36″ on the solar surface. For simultaneous observations in multiple spectral ranges covering the photosphere and chromosphere, the Echelle spectrograph was originally equipped with three pco.4000 cameras. Overlapping spectral orders that might interfere with the observations are removed by broad-band filters mounted directly in front of the cameras. Multiple setups were used in the past with VTT Echelle spectrograph using the pco.4000 cameras (e.g., Verma *et al.* 2012, 2020; Kontogiannis *et al.* 2020; Dineva *et al.* 2020). The most common spectral lines observed are H$\alpha$, Cr I, and H$\beta$. One of the setups with the pcso.4000 cameras used a 4-pixel binning in the spatial and 8-pixel binning in the spectral direction, resulting in a pixel size of 0.36″ along the slit and a spectral resolution of 1.5 pm pixel$^{-1}$. The slit width of 80 $\mu$m also determined the length of the scan steps of 0.36″. Operating the VTT with this setup provides the opportunity to acquire fast time series of spatial scans in a few tens of seconds up to a few minutes while enabling a very high spectral resolution.

Recently, VTT's camera system has been updated and has undergone science verification in 2023. This new camera system, named Fast Multi-Line Universal Spectrograph (FaMuLUS) camera system, enables high-cadence observations of high-resolution spectra. FaMuLUS consists of four IMAGER MX 50M cameras that can be equipped with a variety of spectral filters, enabling observations combining many different spectral lines. In addition, settings for on-disk and off-disk observations are available. The observed FOV can be selected depending on the number of scan steps, which in combination with the

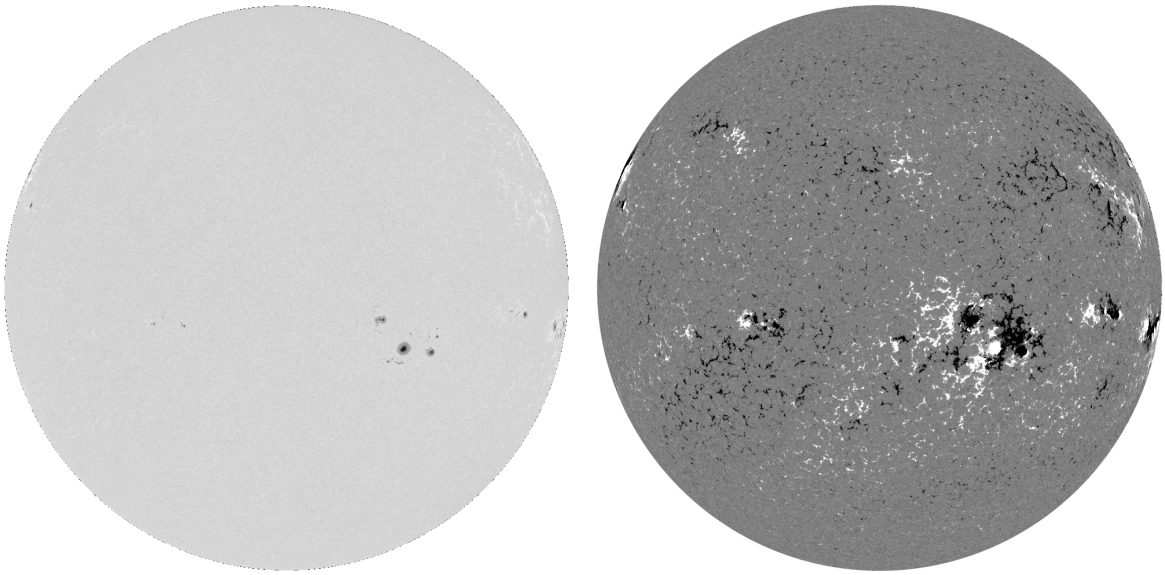

**Figure 1.8** Full-disk limb-darkening corrected continuum image (*left*) and LOS magnetogram (*right*) obtained with SDO/HMI at 10:04:30 UT on 2024 May 24. The LOS magnetogram is displayed in the range of ±100 G.

longest exposure time consequently determines the time required to complete a full scan and the cadence at which time series can be captured.

### 1.5.4 Solar Dynamics Observatory

The SDO (Pesnell, Thompson, and Chamberlin 2012), launched on 2010 February 11, is the space weather mission in NASA's *Living With a Star* (LWS) program. It is in a geosynchronous orbit inclined by 28° about the longitude of the SDO's dedicated ground station in New Mexico. The primary objectives of SDO are to determine how the solar magnetic field is generated and structured, and how the magnetic energy is released into the heliosphere and the solar system. By monitoring the formation and topology of the magnetic field and linking processes from the interior of the Sun, through the photosphere and chromosphere, to the corona, the prediction of solar activity is foreseen. This includes the occurrence of flares (Toriumi and Wang 2019), CMEs (Kilpua *et al.* 2017), and the solar activity of future solar cycles. Over the past decade, SDO has provided countless data and observations of all types of solar events, providing new insights. The large SDO data volume with the addition of synoptic data from ground-based observations enables statistical analysis of solar activity on time scales ranging from minutes to the length of the solar cycle.

The variety of instruments that SDO provides is well suited to evaluate the evolution of magnetic features from growth to decay. Relevant data includes images, magnetograms, and spectra, which are delivered as FITS data (see Pence *et al.* (2010) for more information). These data are continuously gathered and made available to the scientific community through constant contact with the spacecraft. The instruments on board SDO include the Helioseismic and Magnetic Imager (HMI, Scherrer *et al.* 2012; Schou *et al.* 2012), the Atmospheric Imaging Assembly (AIA, Lemen *et al.* 2012), and the Extreme Ultraviolet Variability Experiment (EVE Woods *et al.* 2012). However, only data from HMI are included in this doctoral thesis.

HMI acquires maps of the magnetic and velocity fields on the solar surface. The observations consist of full-disk images taken at a cadence of 45 s and an image scale of about 0.5″. The Doppler shift of the Fe I $\lambda$617.3 nm spectral line is used to determine the photospheric surface velocity over the entire visible solar disk. The line-of-sight (LOS) component of the magnetic field is also produced every 45 s, which complements the Doppler-velocity observations used for helioseismology. Stokes vectors at six wavelength positions across the line are acquired every 90 – 135 s. These recordings are assembled into various data products with a 12-minute cadence using Milne–Eddington inversions (Borrero *et al.* 2011).

## 1.6 Methods

### 1.6.1 Local Correlation Tracking

Horizontal proper motions on the solar surface can be estimated using Local Correlation Tracking (LCT) as introduced by November and Simon (1988). This work uses the implementation described in Verma and Denker (2011) and evaluated in Verma, Steffen, and Denker (2013). Displacement vectors are calculated from consecutive images of time-series through cross-correlation of small regions. Before the application of LCT, the basic image calibration such as subtraction of dark current, gain correction, and removal of spikes by high-energy particles are performed. Then, the images are aligned by the computation of cross-correlations. A sub-sonic filter with a cut-off frequency of $c_s \approx 10$ km $^{-1}$, corresponding to the photospheric sound speed is used to remove the signature of the 5-minute oscillation. Furthermore, a high-pass filter, implemented as a Gaussian function with a full-width-at-half-maximum (FWHM) corresponding to the size of the granule, is applied to remove the image gradients. The localized displacements are computed on small image tiles of consecutive image pairs using FFT-based cross-correlations, which are converted to localized horizontal velocity vectors by dividing by the time between the cross-correlated images. Hence, the core of LCT code, where the the cross-correlation $c_l(x,y,x',y')$ is computed over a image tiles centered on the coordinates $(x,y)$ for each pixel in the image pairs $i_{l-1}(x,y)$ and $i_l(x,y)$, is given by

$$\begin{aligned} c_l(x,y,x',y') &= \Re\{\mathcal{F}^{-1}[\mathcal{F}(i_{l-1}(x,y,x',y')g(x',y'))\cdot \\ &\quad \mathcal{F}^*(i_l(x,y,x',y')g(x',y'))]\}d(x',y'), \end{aligned} \tag{1.1}$$

where $g(x',y')$ denotes a weighting function serving as an apodizing window, which has the same form as the Gaussian kernel used for high-pass filtering, and it ensures that the displacement vectors are computed without preference in azimuthal direction (see details Verma and Denker (2011)).

Verma and Denker (2011) highlighted the systematic error introduced by the LCT algorithm with short cadence and the dependence of accuracy on the duration of the averaging maps. Their evaluation concluded that the datasets used for LCT should have a cadence of 60 – 90 s, and the computed maps should be averaged for an hour to minimize contributions by individual granules and to reveal persistent flow patterns. Based on these recommendations, the data in this work, namely data from GST, the LCT map was averaged for 30 min and 60 min, while the GREGOR time series maps were averaged for 40 min. The 60-second cadence suggested by Verma and Denker (2011) has been deliberately chosen shorter in this work because of the improved time resolution of the present data. Therefore, a cadence of 30 s was chosen for GST BFI data. For the analysis of GREGOR HiFI+ data, images were separated in time by $\Delta t = 6\times 6$ s $= 36$ s (Ca II H, broad- and narrow-band H$\alpha$, and TiO) and $\Delta t = 3\times 12$ s $= 36$ s (blue continuum and G-band). This work presents the first application of the LCT algorithm of (Verma and Denker 2011) to high-resolution chromospheric H$\alpha$ line-core and line-wing images (Kamlah *et al.* 2023).

### 1.6.2 Background-subtracted Solar Activity Maps

Another tool to trace the variation in the solar images is a so called Background-subtracted Solar Activity Map (BaSAM). The initial concept was introduced in Verma *et al.* (2012) to trace the movement of MMFs in the last stages of a decaying sunspot. Denker and Verma (2019) established that the BaSAMs are an efficient tool for analyzing the properties of the global magnetic field and solar activity in general. They visualized variations in intensity and magnetic fields and applied the technique to both full-disk solar data and smaller regions-of-interest (ROIs). BaSAMs require three-dimensional data cubes with two spatial dimensions and a time coordinate to determine variability. Temporal variations are visualized in the spatial domain, providing an opportunity to investigate the interaction between magnetic flux and surrounding plasma motion.

BaSAMs are implemented as the mean absolute deviation within a time series calculated for each pixel of the solar image. This involves computing the background-subtracted variation of a time-dependent quantity $S(t)$, such as magnetic field strength or intensity, based on individual images of a time series $S(t_i)$. This can be formally written as

$$\langle |S - \langle S \rangle| \rangle = \frac{1}{N}\sum_{i=1}^{N} |S(t_i) - \langle S \rangle| \quad \text{with} \quad \langle S \rangle = \frac{1}{N}\sum_{i=1}^{N} |S(t_i)|\,. \tag{1.2}$$

Before computing BaSAMs, the time series should be properly aligned, the Center-to-limb-variation (CLV) removed, and, if required, geometric foreshortening corrected. The parameters that directly affect the appearance and morphology of the BaSAMs are determined by the science case. Longer durations result in more pronounced smoothing of the background, which enhances the visibility of larger variations. Conversely, shorter durations may not provide enough time for significant evolutionary changes to occur, but they can reveal fine structural details. For example, Denker and Verma (2019) presented UV BaSAMs that showed brightenings between opposite-polarity sunspots. These brightenings became stronger as the duration of the sliding average increased. BaSAMs can be used to highlight the stretching, separating, and rotational motions of solar features. The first application of BaSAMs on high-resolution chromospheric images at different wavelength points was presented in Kamlah *et al.* (2023). The idea was further expanded by the Denker *et al.* (2023b) who showed the high-resolution spectral BaSAMs in two chromospheric spectral lines.

### 1.6.3 Computing Line-of-sight Velocity and Magnetic Fields

Information about the solar process can be derived from the spectral line characteristics of the elements found in the solar atmosphere. These lines result from the absorption and emission of photons. The absorption of a photon excites the corresponding electron, which is then lifted to a higher energy level. The subsequent relaxation process by which the electron returns to its initial state is a key aspect of this phenomenon. Several physical parameters of the plasma can be determined from the solar spectral lines. Magnetic fields and LOS velocities are derived using line fitting (e.g., Kamlah *et al.* 2024) and the SIR (Ruiz Cobo and del Toro Iniesta 1992) code.

Information about the environment is contained in the shape of the spectral line. Several broadening mechanisms affect the shape of line profiles. According to Heisenberg's Uncertainty Principle, natural broadening occurs due to the blurring of energy which subsequently broadens the observed line. The lines are further blurred by pressure or collision-induced broadening, which is comparable in magnitude to the natural broadening. A more pronounced effect is caused by Doppler broadening, which results from the motion of atoms, where the speed of the atoms determines the random Doppler shift introduced to the emitted and absorbed photons. To achieve an accurate fitting of spectral lines, different models can be applied in combination with different weighting factors. The most common model is a Gaussian profile, which is typically used in statistics to represent normal distributions, and the Lorentzian profile, which describes a dampening profile. In many cases, a combination of these two models is employed to accurately fit spectral lines. This combination is referred to as the Voigt profile. Another modification of the Lorentzian profile is the Moffat profiles. These different profiles are given by

$$
\begin{aligned}
&\text{Gaussian:} && G = a_0 \exp(-1/2\, u^2) + a_3 \\
&\text{Lorentzian:} && L = a_0/(u^2+1) + a_3 \\
&\text{Voigt:} && V = G * L \\
&\text{Moffat:} && M = a_0/(u^2+1)^{a_4} + a_3 \\
&\text{with} && u = (x - a_1)/a_2,
\end{aligned}
$$

where the $a_i$ are fitting coefficients and the symbol "$*$" indicates the convolution of two profiles. In this work, the photospheric and chromospheric spectral lines are fitted with Gaussian profiles.

The magnetic properties of the solar atmosphere can be determined from the Zeeman splitting of polarized light. The strength and orientation of the magnetic fields determine the degree of polarization and separation of the line components. The polarization states can be described by the four Stokes parameters. Stokes $I$ represents the intensity, while Stokes $Q$ and $U$ represent two independent states of linear polarization. Stokes $V$ describes the circular polarization of the light. The Landé $g$-factor is an effective measure of the magnetic sensitivity of a spectral line. Higher values indicate greater sensitivity. In this work, the magnetic properties of the atmosphere were determined using the SIR code. The response functions represent the partial derivatives of the Stokes parameters.

The SIR code is an analysis tool for solar spectra under local thermal equilibrium (LTE) conditions. One of the modes is the synthesis package, which solves the radiative transfer equation (RTE) for polarized light by calculating Stokes spectra from defined model atmospheres. These atmospheres can consist of two components that can be magnetized or unmagnetized. In addition, the inversion mode facilitates the

analysis of the thermal, dynamical, and magnetic structure of the solar atmosphere corresponding to the formation height of the observed spectral profiles. The user-provided model atmosphere is iteratively adjusted to fit the synthetic Stokes profiles to the observed profiles. To minimize the discrepancies between the observed and synthetic spectra, a Marquardt nonlinear least squares algorithm (Press, Flannery, and Teukolsky 1986) is implemented in the inversion module. Subsequently, a modified singular value decomposition (SVD) algorithm (Ruiz Cobo and del Toro Iniesta 1992) is applied to solve the fitting problem. The details of the SIR application to GREGOR GRIS data are given in Chapter 3.

# Chapter 2

# High-resolution Imaging of Solar Pores

## 2.1 Introduction

High-resolution observations of the solar photosphere facilitate investigating the interaction between magnetic fields and convective processes. Dark features formed by a sufficiently strong magnetic field vary in size and lifespan whereby the critical differentiation between pores and sunspots is the absence or presence of a penumbra, respectively. The main difference besides size and lifetime is the higher field strength of 1 800 – 3 700 G in the darkest parts of sunspot umbra (Livingston 2002) as compared to 600 – 1 800 G (Sütterlin 1998; Verma and Denker 2014) in pores, which is about the same as for the outer parts of penumbrae (Livingston 2002).

The transition of a pore to a sunspot is characterized by a variety of flows. A radial outward flow is the Evershed flow, starting at the penumbra. It is correlated with the inclination angle and horizontal strength of the penumbral magnetic field. Extensions of the penumbral Evershed flow may appear as moving magnetic features in the moat flow. Verma, Kummerow, and Denker (2018a) described the formation of significant asymmetries in flows around unipolar axisymetric sunspots. The asymmetry of the moat flow is due to sunspot motion across the solar disk and gets further disturbed by surrounding plasma motion.

Quintero Noda *et al.* (2016) inferred temperature, LOS velocity, and LOS magnetic field of a pore at photospheric levels ($\tau = 1$) and extended them to higher atmospheric layers ($\tau = -2$). The temperature was coolest inside the pore and hotter in surrounding quiet-Sun region, which is consistent across all evaluated heights. In addition, quiet-Sun temperatures were exceeded in neighboring plage regions. The LOS velocity inside the pores was close to zero, however, with downward motions at the edges, which were only detectable in lower photospheric layers, i.e., below $\tau = -1$. The LOS magnetic field was strongest in the central part of the pore, where the canopy effect results in a decrease of field strength with increasing height.

A feature commonly connected to formation and decay of pores or sunspots are light bridges. These bright, long, and narrow structures, which cross or penetrate the umbra, present a structure different from the surrounding umbra, exhibiting weaker and more inclined fields (Liu and Liu 2015). Light bridges extend in a canopy-like structure to higher atmospheric layers. However, the formation and magnetic properties of light bridges remain a subject of investigations. Studies indicate that the formation of light bridges is a result of intruding umbral dots and relate them to plasma ejections or chromospheric H$\alpha$ surges along the light bridges. Thus, they may act as a heat source in the chromosphere. According to Louis (2015), the interaction of umbral dots and intruding penumbral filaments, which is generally observable during light bridge formation, further confirms magneto-convection in sunspots and pores. The author emphasizes that the pronounced chromospheric activity, which is caused by convective disruptions, becomes more vigorous and apparent as compared to the rest of the sunspot. Consequently, light bridges and the surrounding umbra should be treated as two different systems. In recent simulations, Panja, Cameron, and Solanki (2021) showed that light bridges form at a certain depth by intrusions of plasma that are transported to the surface by upflows.

Based on observations and numerical models Toriumi, Cheung, and Katsukawa (2015) presented a physical picture of the formation of light bridges in an emerging region. According to these authors, emerging magnetic fields rising from convection zone (Zwaan 1985) split into multiple bundles of two

polarities. The local weakly magnetized plasma with upflows is carried along between these flux bundles and shows up as a light bridge in the photosphere. The light bridge has in its center a deep convective upflow, which brings horizontal magnetic flux to the surface. Interaction between this horizontal flux with the vertical field of the neighboring pores leads to the formation of a strong electric current layer at the border of the light bridge. The strong downflows at the borders of the light bridge form concave dips, where the internal horizontal field of the light bridge is connected to external vertical fields. In higher atmospheric layers, these external fields fan out and form a canopy structure. The continuous convection creates upflows, which turn into bi-directional flows along the length of the light bridge, transporting plasma and magnetic field towards the connection points of the surrounding granulation.

Small-scale inhomogeneities in the magnetic field and velocity are present in the light bridge, which have opposite polarities to the rest of the light bridge and umbra, and they also exhibit large Doppler shifts (Louis 2015). However, supersonic downflows are also encountered in the more unipolar parts of light bridges (Louis *et al.* 2009). High-resolution observations of the fine structure at the border of pores reveal downflow rims including filamentary structures near the rims. Positive divergence structures with localized divergence centers are often related to exploding granules (Bonet *et al.* 2005). Typically, not necessarily symmetric inflows are detected in the pores' interior and outflows at their periphery. Whereby a low velocity and negative divergence is detected inside pores, and distinct G-band bright points appear in the magnetic flux system in proximity to the border of the pore (Verma and Denker 2014).

In a one-to-one comparison with observations and numerical simulation of pores, Leka and Steiner (2001) confirmed enhanced Stokes-V asymmetry in the encircling magnetic elements including pores and azimuth centers, which are the result of strong downflows at their borders. However, in the interior of magnetic elements, they find evidence for intermingled up- and downflows. Furthermore, they notice that even magnetic features that are not visible as a dark structure in continuum harbor a canopy, caused by the same physical effects. In magnetohydrodynamics (MHD) simulations of pores, which included a realistic, predominantly vertical field, adjacent granules presented an edge-brightening, and the pores were surrounded by downflows (Cameron *et al.* 2007). Here, the decay is connected to a loss of magnetic flux from the periphery to the adjacent intergranular lanes. Certain differences exist between the leading and trailing polarities of an active region. Rempel and Cheung (2014) identified some of them in simulations covering the whole life cycle of the flux emergence system, i.e., from spot formation to decay. In their simulations both leading and trailing spots reach around half their peak flux at the same time. However, the formation of the trailing spot starts before the leading part and extends further. Furthermore, they report delay timescales of the order of a few days, where the decay is mostly driven by convective motions.

This study takes a closer look at a strong light bridge within a solar pore by combining multi-wavelengths observations of the photosphere and chromosphere. Section 2.2 presents the observations and the data processing. The necessary techniques are discussed, which were applied to time-series of images and data from imaging spectroscopy to investigate flows and magnetic fields in and around pores. The observational results from different instruments are presented in Sect. 2.3 and discussed in Sect. 2.4, where the present results are interpreted in context with contemporary literature and standard works on this subject. Section 2.5 summarizes noteworthy observational findings and highlights their importance for future studies of light bridges in pores.

## 2.2 Observations and Data Reduction

In this section, recording, reduction, and analysis of the high-resolution GST and synoptic SDO data are described, including relevant details on instruments, observing settings, and methods.

### 2.2.1 Observations

The observations were carried out with the 1.6-meter aperture Goode Solar Telescope (GST, Cao *et al.* 2010b) at the Big Bear Solar Observatory (BBSO) from 18:00 UT to 22:35 UT on 2015 April 1. The local seeing environment at this mountain-lake-site observatory are described in Verdoni and Denker (2007). Recording of flat-field frames interrupted the observations from 18:34 – 18:56 UT, 20:39 – 20:49 UT, and 22:01 – 22:18 UT. The Adaptive Optics (AO) system AO-308 provided real-time image correction,

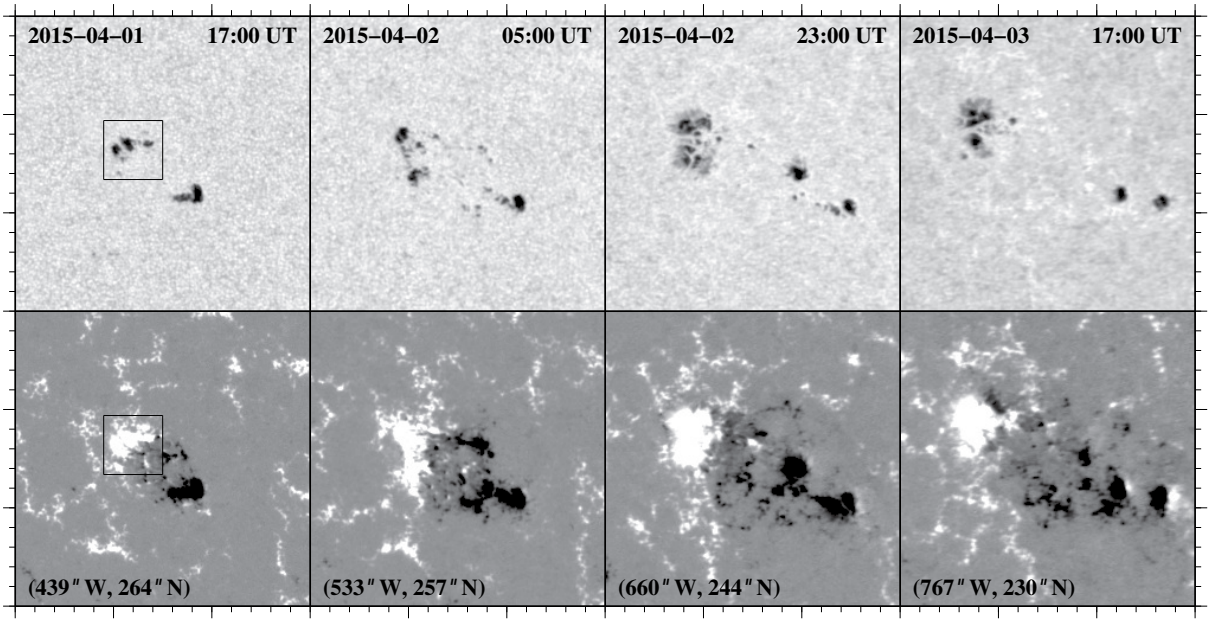


**Figure 2.1** Continuum images and magnetograms showing the evolution of active region NOAA 12317 from 17:00 UT on 2015 April 1 (*left*) to 17:00 UT on 2015 April 3 (*right*). The FOV covers $150'' \times 150''$, and the coordinates in the lower left corners refer to the FOV's center. The black boxes in the left panels corresponds to an ROI of $30'' \times 30''$, which is used in the analysis of the high-resolution H$\alpha$ and TiO time-series. Magnetograms are displayed in the range ±400 G.

utilizing a 100-millimeter diameter Xinetics deformable mirror driven by 357 actuators. The wavefront sensor has 308 subapertures, where a 800×600-pixel Phantom V7.3 camera records images at a frame rate of 2000 Hz, selecting a region-of-interest (ROI) of $416 \times 400$ pixels. The design and implementation of the AO-308 system is described in detail by Shumko *et al.* (2014).

The Broadband Filter Imager (BFI, Cao *et al.* 2010a) at the Nasmyth focus consists of the several filtergraphs, which enable high-spatial resolution photometry. However, only the TiO $\lambda$706 nm interference filter with a bandpass of 10 Å was used during observations. Time-series of 14-bit, 2048×2048-pixel TiO images were captured using a pco.2000 camera. The exposure time was 1.1 ms, and sets of 100 images were acquired at a cadence of 15 s. After frame selection, only the best 70 images of a set were used for speckle masking image restoration (Wöger and von der Lühe 2008). In this process, the original image size is reduced to $1844 \times 1844$ pixels. An image scale of $0.034''$ pixel$^{-1}$ yields a field-of-view (FOV) of $63'' \times 63''$. Thus, the images are oversampled by a factor of 1.6, considering that the diffraction limit of the telescope at the wavelength of TiO is $\alpha = 1.22\,\lambda/D = 0.11''$ according to the Rayleigh criterion, where $D$ is the diameter of the telescope. The full time-series consists of 836 speckle-restored images covering the trailing part of the active region NOAA 12317.

The Visible Imaging Spectrometer (VIS) captured data in the chromospheric H$\alpha$ $\lambda$656.3 nm line (Cao *et al.* 2010a). Filtergrams with a bandpass of 0.8 Å were taken with a single Fabry-Pérot etalon in telecentric mount. The camera has $2560 \times 2160$ pixels, and the instrument covers a circular FOV with a diameter of $70''$, i.e., only about 80% of the detector is illuminated with an image scale of $0.029''$ pixel$^{-1}$. An H$\alpha$ dataset consists of $5 \times 40 = 200$ filtergrams covering the line core and four wavelength points in the wings, which are nominally placed at ±0.4 Å and ±0.8 Å from line center. However, the exact locations of the filtergrams in the spectrum may differ from the nominal settings. Frame selection based on the highest image contrast reduces the data volume to $5 \times 25 = 125$ filtergrams. Exposure times of 9, 15, and 20 ms (line wing to line core) are sufficiently short for image restoration with the speckle masking technique (Wöger and von der Lühe 2008). The filtergrams were recorded with a frame rate of 20 Hz and a delay time of 20 s, which results in a cadence of 30 s for 440 speckle-restored datasets of line core and line-wing images.

The GST data are complemented by observations from the Solar Dynamics Observatory (SDO, Pesnell, Thompson, and Chamberlin 2012). Full-disk continuum images and line-of-sight (LOS) magnetograms were provided by the Helioseismic and Magnetic Imager (HMI, Scherrer *et al.* 2012; Schou *et al.* 2012). The nominal image scale of HMI is $0.5''$ pixel$^{-1}$, which is increased to $0.6''$ pixel$^{-1}$ in the image

registration (rotation, translation, and scaling), i.e., in the Level 1 to Level 1.5 data conversion. An ROI with a size of $150'' \times 150''$ ($250 \times 250$ pixels) was selected, which tracks the active region during its disk passage. Continuum images and magnetograms are both recorded with a cadence of 45 s, and four images illustrating the evolution of active region NOAA 12317 over a 48-hour period are displayed in Fig. 2.1, in which the black boxes correspond to an ROI of $30'' \times 30''$, which is used in the analysis of the high-resolution H$\alpha$ and TiO observations. The temporal evolution of photometric area and magnetic flux is shown in Fig. 2.2 for a 6½-hour window on 2015 April 1, which includes the observing period at BBSO with a 1-hour margin. The processing of continuum images and magnetograms was described in Beauregard, Verma, and Denker (2012) and Verma (2018), which includes correcting differential rotation using 20:19:30 UT as the reference time for aligning the time-series. However, geometrical foreshortening was not corrected due to the small size of the ROI.

The data analysis in the following sections is based on four types of time-series data: high-resolution *TiO images*, high-resolution *Hα filtergrams*, cutouts from full-disk *continuum images*, and cutouts from full-disk LOS *magnetograms*. This nomenclature is subsequently used to uniquely label the data types.

### 2.2.2 Data Reduction and Analysis

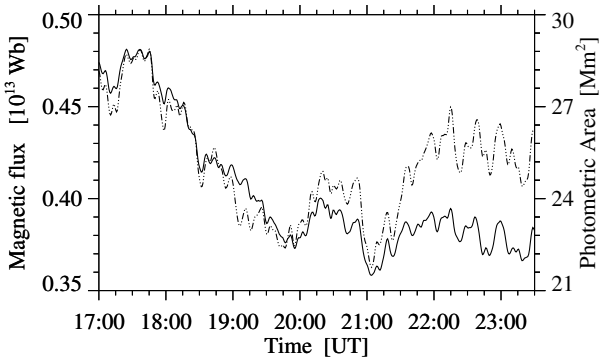


**Figure 2.2** Evolution of the magnetic flux (*solid*) and photometric area (*dashed*) on 2015 April 1 for a FOV of $95'' \times 95''$ covering positive-polarity pores in active region NOAA 12317.

The TiO image quality was determined using the Median Filter Laplacian Similarity (MFLS), which is a variant of the Median Filter Gradient Similarity (MFGS, Deng *et al.* 2015). The MLFS was computed for a FOV of $63'' \times 63''$ ($1844 \times 1844$ pixels) and for the central ROI of $42'' \times 35''$ ($1224 \times 1024$ pixels) containing only the pore. The values for both FOVs are comparable throughout the TiO time-series, which covers 4½ hours but with three interruptions. In Fig. 2.3, TiO images of the central ROI are presented, which have the best image quality within a certain time interval. These images follow the evolution of three pores in active region NOAA 12317. Because of its equatorial mount and coudé feed to the optics laboratory, the GST exhibits an image rotation rate of 15° per hour in the focal plane. Thus, all images of the time-series have been rotated, aligned, and matched with sub-pixel accuracy. The H$\alpha$ images were subsequently aligned to match the $30'' \times 30''$ ROI of the TiO images. The aligned H$\alpha$ line core images are shown in Fig. 2.4 demonstrating the chromospheric evolution above the three pores. The slight mismatch of the observing time between TiO and H$\alpha$ images results from applying the image quality metrics independently to the two time-series.

Taking flat-field frames interrupts data recording of both TiO images and H$\alpha$ filtergrams. Observations in H$\alpha$ blue line wing at −0.535 Å from line core consistently yields the highest MFLS values during the time-series. The values of the other wavelength points are lower and show a larger scatter. In any case, even though metrics such as MFGS and MFLS are less dependent on the structural contents of the images, the different morphology of the H$\alpha$ contrast features easily explains these differences. Higher MFLS values in the time period 19:00 – 22:00 UT are indicative of better seeing conditions, which can occur at the mountain-lake site BBSO at any time of the day.

The aligned TiO images are the basis for computing the horizontal proper motions. For this purpose, Local Correlation Tracking (LCT, November and Simon 1988; Verma and Denker 2011) is applied to three datasets covering the time periods (i) 18:00 – 18:30 UT, (ii) 19:00 – 20:00 UT, and (iii) 20:50 – 21:50 UT. Continuous data are available for these three datasets, avoiding the aforementioned data gaps. The focus is on the central ROI $30'' \times 30''$ ($878 \times 878$ pixels). A subsonic filter is applied with a cut-off velocity $v_c = 4$ km s$^{-1}$ to remove the intensity variations caused by the five-minute oscillation from the time-series. Since computing cross-correlations is sensitive to intensity gradients, the images are treated with a high-pass filter. The LCT velocities are computed over image tiles with the size of $2.2'' \times 2.2''$ ($64 \times 64$ pixels), which corresponds to about 1600 km × 1600 km on the solar surface. A Gaussian

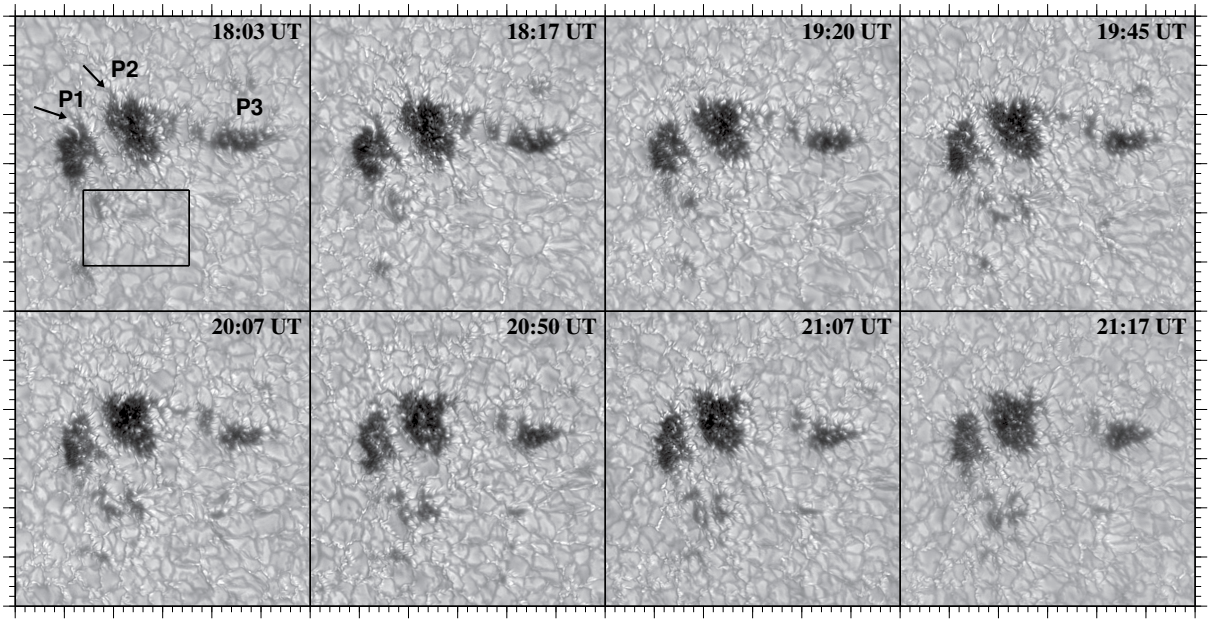


**Figure 2.3** Temporal evolution of pores observed in the TiO $\lambda$706 nm bandhead images on 2015 April 1. The best images were selected, hence they are not equidistant in time. The ROI has a size of $30'' \times 30''$. In the upper left panel the three major pores are labeled P1, P2, and P3, and the plage region is enclosed within the rectangular box.

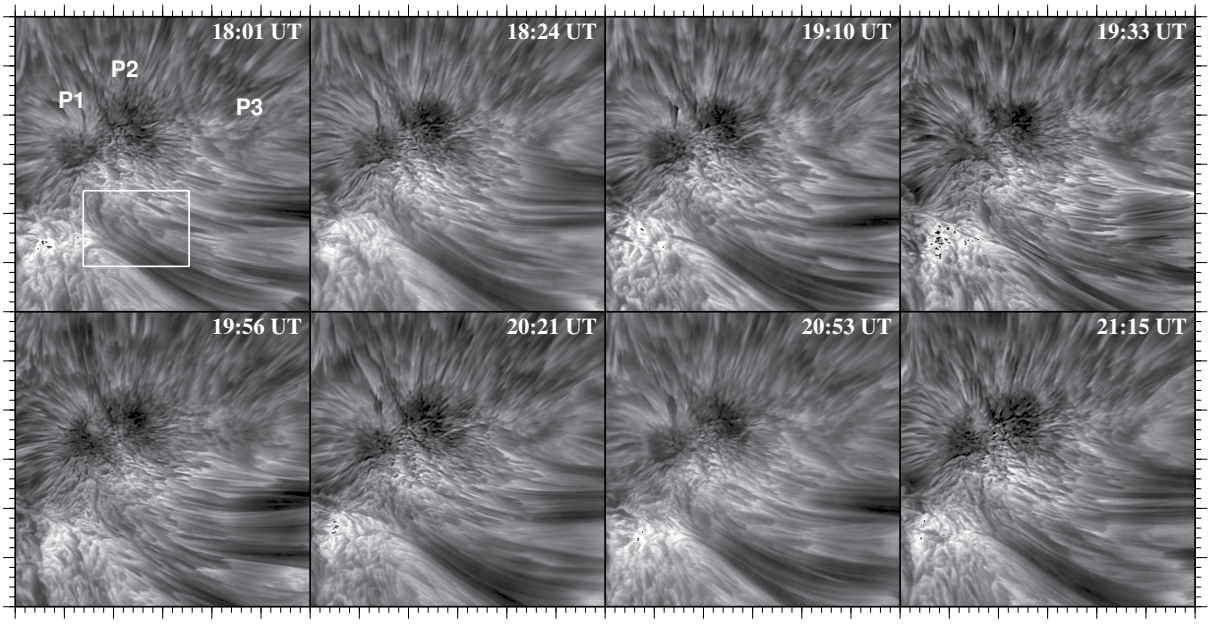


**Figure 2.4** Temporal evolution of pores observed in the H$\alpha$ $\lambda$656.3 nm line core images on 2015 April 1 (otherwise same as in Fig. 2.2).

kernel with full-width-and-half-maximum (FWHM) of 1200 km is applied to the image tiles to track on granule-size structures. Consecutive image tiles, separated by $\Delta t$ = 30 s in time, are used for the cross-correlations to compute the local flow vectors. These flow vectors are averaged over the duration of each time-series, i.e., 30 min for the first time-series and 60 min for the other two.

The same LCT algorithm was used to compute the chromospheric horizontal proper motions. Because of artifacts impacting image quality and time gaps the H$\alpha$ time-series is divided into four datasets of which three are used in the following data analysis. They cover the time periods (i) 18:01 – 18:31 UT, (ii) 18:56 – 20:00 UT, and (iii) 20:03 – 20:39 UT. The first two datasets are closely matched with those of the TiO time-series. However, the third dataset contains images, which were recorded before last TiO dataset started. This selection provides data with highest image quality. The H$\alpha$ datasets comprise (i) 60, (ii) 126, and (iii) 72 filtergrams, respectively. The focus is again in the central part of ROI with a size of $30'' \times 30''$

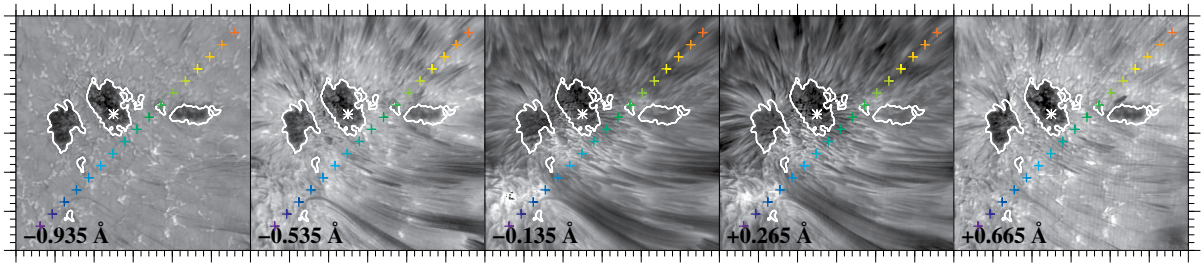


**Figure 2.5** Speckle-restored H$\alpha$ filtergrams of each wavelength point of the H$\alpha$ line scan. The wavelength positions with respect to the H$\alpha$ line core are given in the lower left corner of each panel. Neighboring wavelength points are separated by 0.4 Å. The white contour outlines the umbra seen in corresponding TiO images for intensities lower than 0.8. The ROI has a size of $30'' \times 30''$. The colored crosses indicate the location of extracted H$\alpha$ line profiles shown in Fig. 2.6.

(1038 × 1038 pixels). The cut-off velocity for the subsonic filter had to be increased to $v_c = 20$ km s$^{-1}$ because the chromosphere is rich in dynamic and fast-moving features, which should be preserved. The high-pass filter is also essentially the same, as is the chosen tile size of $2.2'' \times 2.2''$ (76 × 76 pixels).

Five speckle-restored filtergrams of an H$\alpha$ line scan are shown in Fig. 2.5, which were obtained at 18:01 UT. The superimposed white contours refer to the corresponding TiO image, where an intensity threshold of $I_{\rm umbra} < 0.8$ is used to outline the umbra. Visual inspection of the filtergrams in the red line wing suggests that they are closer to the H$\alpha$ line core as compared to the filtergrams in the blue line wing. Low correlation values for the inner and outer line-wing filtergrams corroborates this observation. An estimate of the wavelength position can be derived using the following procedure: (i) assume that neighboring filtergrams are separated by 0.4 Å, (ii) normalize the filtergrams so that quiet-Sun intensity (i.e., at the corners of the ROI) matches the intensity of the H$\alpha$ spectrum at this wavelength position, (iii) compute the linear correlation between the line-wing pairs, (iv) repeat this procedure for various wavelength shifts using linear interpolation, and (v) find the wavelength shift that results in the highest value for the linear correlation. This procedure yields a wavelength shift of 0.135 Å, which can be reproduced for other H$\alpha$ line scans of the time-series. Thus, the corrected wavelength position of H$\alpha$ filtergrams are −0.935 Å, −0.535 Å, +0.135 Å, +0.265 Å, and +0.665 Å, when scanning from the blue to the red line wing. Note that in step (ii), the center-to-limb variation of the H$\alpha$ spectral line was taken into account using interpolated versions of the tabulated profiles by David (1961). The heliocentric angle of the active region was $\mu = 0.83$. The shifted wavelength positions are displayed in the lower left corners of Fig. 2.5.

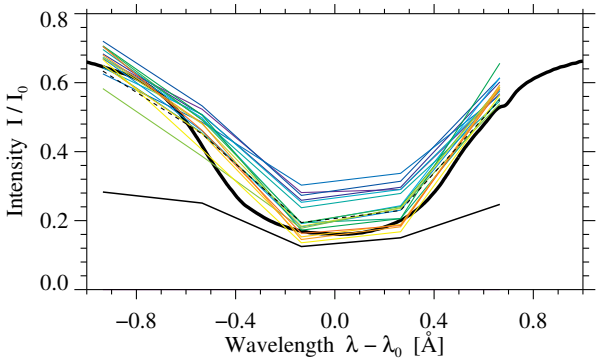


**Figure 2.6** Color-coded H$\alpha$ line profiles, which are marked by matching crosses in Fig. 2.5. The dashed and solid black lines represent the average and umbral spectral profiles, respectively. The thick solid line refers to the Kitt Peak FTS disk-center spectral atlas (Neckel and Labs 1984; Neckel 1999) and served as a reference in the wavelength calibration.

The ability to compute H$\alpha$ Doppler maps is another important result of this procedure. The Doppler shifts are estimated using Gaussian fits to the five-point spectral profiles. The average Doppler velocity around the quiet-Sun region around the pores was $-0.18 \pm 1.33$ km s$^{-1}$, whereas the average Doppler velocity inside the pores was $1.00 \pm 1.78$ km s$^{-1}$. The standard deviation refers to the variation within the region rather than to a formal error estimate. A sample of H$\alpha$ line profiles is shown in Fig. 2.6 for the locations marked by color-coded plus signs, which trace the upward diagonal in Fig. 2.5. The mean profile of all plotted lines is added as dashed black line, while the solid black line represents typical profiles of the pores. These sample profiles are derived according to the procedure outlined above and trace different features in the vicinity of major pores, for example, filaments, a small pore, and plage regions.

## 2.3 Results

In this section, morphology and temporal evolution of the pores are investigated based on high-resolution and synoptic data. The connectivity of the pores to their surroundings is analysed and photospheric and chromospheric horizontal proper motions are discussed. Furthermore, the evolution of chromospheric Doppler velocities is examined.

### 2.3.1 Morphology and Temporal Evolution

The photospheric and chromospheric morphology and evolution of the pores is very different, which will be discussed accordingly based on TiO images, continuum images, and magnetograms for the photosphere and based on H$\alpha$ line scans for the chromosphere.

#### Photospheric Evolution

Cutouts from full-disk continuum images and magnetograms with a size of $150'' \times 150''$ show the overall evolution of the active region NOAA 12317 in Fig. 2.1. Unfortunately, because of technical issues, SDO data are not available for the initial emergence of the region. The continuum images and magnetograms are displayed in non-uniform time steps from 17:00 UT on 1 April 2015 to 17:00 UT on 3 April 2015.

Active region NOAA 12317 developed as a typical bipolar region containing pores. The first continuum image and magnetogram show the region one hour before the BBSO high-resolution observations. At 17:00 UT on 1 April 2015, two opposite-polarity region separate along a line, which forms an angle of about 45° with respect to the equator (type B sunspot region according to the Zurich classification). The light bridge's orientation remains stable over the high-resolution observations while showing a counter-clockwise rotation at later stages. The region between the two polarities is a site of ongoing flux emergence with mixed polarities, which is typical for an emerging region (Verma *et al.* 2016b). The leading negative-polarity pore has a very dark, elongated core with a smaller, less dark, elongated core extending at a right angle to the west. The trailing positive-polarity region comprise two dominant pores separated by a strong light bridge accompanied by several smaller pores nearby. The light bridge leaves also a clear signature in magnetograms.

The transition from type B to type D region is characterized by the continuous separation of the two polarities and an increase in area and magnetic flux caused by coalescence of same-polarity flux as is evident in continuum images and magnetograms on 2 April 2015. Another negative-polarity pore appeared in the middle of the bipolar group at 11:00 UT on 2 April 2015. This pore belonged to another flux system which developed alongside the primary flux system. The secondary region contributed new flux and interacted with already existing system. This region moved towards the leading negative-polarity and developed a rudimentary penumbra by 23:00 UT on 2 April 2015. The trailing positive-polarity becomes more complex and two sunspots with partial penumbrae and complex light bridges are present at 23:00 UT on 2 April 2015. Both polarities reached the maximum extent in area and magnetic flux by 23:00 UT on 2 April 2015. At 05:00 UT on 3 April 2015, the overall appearance of both polarities had already simplified and the region's decay started. The two remaining negative-polarity pores shrunk further and almost vanished at 11:00 UT on 4 April 2015 leaving only dispersed magnetic flux in their wake. In contrast, the two major positive-polarity flux concentrations visible at 05:00 UT on 2 April 2015 merged and formed a single sunspot by 23:00 UT on 3 April 2015. The active region NOAA 12317 had an atypical evolution, because the trailing polarity evolved into a mature sunspot, while the leading polarity only produced a small rudimentary penumbra on 2 April 2015.

The high-resolution TiO images are compiled in Fig. 2.3. They trace the evolution of the trailing positive-polarity pores separated by a light bridge as observed on 1 April 2015 with the GST. The labels P1 and P2 refer to these pores. The label P3 denotes another dark feature caused by the emergence of the magnetic flux next to pore P2.

At 18:03 UT, the pore P1 had a smaller umbral core, i.e., compared to pore P2, with a curved filamentary extrusion at the top, which resembled a rudimentary penumbra. The filamentary extrusion existed only for about 15 min but disappeared by 19:20 UT. The pore P1 was full of umbral dots and had continuous flux emergence in its bottom part, which was visible as two faint magnetic knots (Beckers and

Schröter 1968), as indicated by the rectangle in the top-left panel of Fig. 2.3. The umbral dots within the pore P1 formed a faint light bridge by 19:45 UT, which remained until the end of the GST observations at 21:17 UT. Out of the two magnetic knots in the bottom one slowly decayed, whereas the other developed further and grew in size by merging with new magnetic knots so that it developed into a pore by 19:45 UT.

The largest pore in the ROI is labeled P2. This pore is filled with umbral dots and is separated from pore P1 by a thick light bridge. The borders of pore P2 are also rugged. Thin dark hair-like extrusions are present all around pore P2. A larger extrusion is present at the top, which remains visible until 19:45 UT. Over the period of GST observations, the pore P2 decreased in size and became more circular in shape. However, this is the only pore which survives through the complete evolution of the active region. Next to pore P2, another elongated pore P3 is situated. At 18:03 UT, pore P3 is closest to pore P2 with a small magnetic knot placed between them. Over time pore P3 moved away from P2, and eventually became compact.

The light bridge between pores P1 and P2 was already present at the start of the GST observations. It contained a few granules, which continuously evolved throughout the next few hours. Its orientation only slightly changed over time. Apart from the smaller pores in the bottom half of FOV, many extending granules were observed. These granules connected the positive-polarity pores and magnetic knots in the ROI to the negative-polarity pores outside the ROI but covered by the FOV of the continuum images and magnetograms. The lower-right quadrant of the ROI is the site, where flux with mixed polarities emerges as can be seen in the lower-left panels of Fig. 2.1.

To quantify the growth of the pores, their area and the magnetic flux within the active region is computed over the period 17:00 – 23:30 UT on 1 April 2015 17:00 UT, which correspond to 520 continuum images and magnetograms. The FOV was reduced to $95'' \times 95''$ ($160 \times 160$ pixels) encompassing the trailing pores. A binary template pre-selecting the area covered by the positive-polarity magnetic flux was created by applying a Lee filter (Lee 1986) to the magnetograms. Furthermore, a flux threshold of 100 G was applied, along with morphological erosion using a kernel with a width of 0.5 Mm, followed by dilation using a kernel with a width of 3 Mm. Regions with less than 200 pixels were removed from the binary template. Finally, a threshold of 80% of the normalized continuum intensity and a threshold of 10 G are used for computing the photometric area and the magnetic flux of the pores, respectively. The measured magnetic field strength and area were taken at face value. The only correction that is carried out concerns the cosine of heliocentric angle $\mu$. The results are compiled in Fig. 2.2. The photospheric area and magnetic flux decay rates are determined by linear fits after convolution with a smoothing kernel. During the first half of observations, i.e., from 17:00 UT to 20:00 UT both photospheric area and magnetic flux decrease linearly with $-2.74$ Mm$^2$ h$^{-1}$ and $-0.044$ Wb h$^{-1}$, respectively. This matches with the visual impression of shrinking pores as seen in the TiO images. Between 20:00 UT and 21:00 UT, a slight increase occurs in both photospheric area and magnetic flux before the minimum is reached at 21:00 UT. After 21:00 UT, the photometric area increased, which coincided with newly forming pores in the lower part of the ROI. However, the increase in magnetic flux is not very pronounced.

### Chromosphere

The eight line-core H$\alpha$ filtergrams in Fig. 2.4 depict snapshots of the region's chromospheric evolution. In addition, the first H$\alpha$ scan with five wavelength points shown in Fig. 2.5 demonstrates different morphology of the region at different chromospheric heights. In the line core, which traces higher atmospheric layers (Cauzzi *et al.* 2009), the umbrae of the three pores P1, P2, and P3 are hard to visualize under overlaying chromospheric radial filaments. Contours computed using simultaneous TiO images assist in following the evolution in and around the pores. The light bridge separating the pores P1 and P2 is discernible in all H$\alpha$ wavelength settings. The newly emerging pores in the bottom of the ROI are marked by an rectangular box.

In the H$\alpha$ line core, the pores P1 and P2 are surrounded by radial superpeumbral filaments except for the lower part, which faces the newly emerging pores of opposite polarity. These filaments originate directly at the border of the pores and appear more penumbral in nature than superpenumbral. However, a counterpart of these filaments is absent in the photosphere. Along these penumbral filaments, the running penumbral waves propagate outwards. In addition, the individual filaments display more dynamic motion. Filaments in the upper part of pores P1 and P2, i.e., at the tip of the light bridge (marked by arrows

in Fig. 2.2), demonstrate twisting motions accompanied by the apparent ejection of material. Pore P3 is mostly obscured in H$\alpha$ line-core filtergrams. The region connecting both polarities of primary and secondary flux systems shows an elongated arch filament system with two major filaments. These arch filaments appear to be stretched out and connect to the bottom of pores P1 and P2. Even though the arch filament system is continuously changing its appearance, it survives until the end of the high-resolution observations.

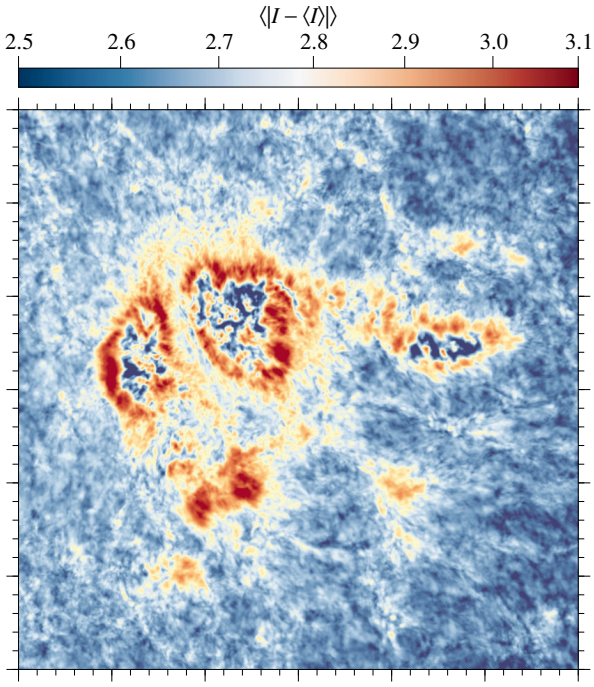


**Figure 2.7** BaSAM of the entire TiO time-series of 836 images covering the time period 18:00 – 22:34 UT. The ROI has a size of $30'' \times 30''$. The color bar indicates the variations in intensity on logarithmic scale.

Time-series of the four red- and blue-wing filtergrams also demonstrate the ever-changing appearance of the active region. Chromospheric fibrils are already significantly suppressed in the outer line-wing filtergrams at −0.935 Å and +0.665 Å. As mentioned Sec. 2.2.2, a slight asymmetry appears in the five wavelength positions. The features at the third and fourth wavelength position are virtually identical and must be located close to the H$\alpha$ line core. In any case, in the outer red-wing and both blue-wing filtergrams, small-scale brightenings are present in the vicinity of the pores. Conspicuous bright plage regions are visible in the lower left corner of the filtergrams close to the H$\alpha$ line core, where one end of the arch filament system is rooted. In this region, continuous interaction between magnetic features can be traced in the time-series of magnetograms. The bright H$\alpha$ plage region is a persistent feature throughout the high-resolution observations. Furthermore, the presence of the ever-changing chromospheric fibrils is clearly seen in the H$\alpha$ line-wing filtergrams – and even more in close vicinity to the pores. These chromospheric fibrils and filaments show much stronger absorption in the H$\alpha$ line-core filtergrams.

### 2.3.2 Background-subtracted Solar Activity Maps – Connectivity

Background-subtracted Solar Activity Maps (BaSAMs) are a new tool to analyze the connectivity of pores to their surroundings. Thus, a brief description of this method is provided. Furthermore, BaSAMs are for the first time applied to high-resolution photosphere images and chromosphere images

#### Background-subtracted Solar Activity Maps – TiO images

To follow variations in and around the pores and to identify locations where most changes occur, so called Background-subtracted Solar Activity Maps (BaSAMs, Denker and Verma 2019) are computed. As explained in Denker and Verma (2019), this technique relies on the computation of an average, two dimensional map for the entire time-series, which is then subtracted from the individual maps, followed by computing an average, two-dimensional map of the modulus of these difference maps. The two-dimensional BaSAMs are a good and quantitative visualization tools to identify location of significant changes in SDO magnetograms and UV images (e.g., Verma *et al.* 2012, 2020). However, this is the first application of BaSAMs to images with high-spatial resolution, i.e., a spatial resolution of one tenth of an arcsecond or better.

The BaSAM of the entire TiO time-series is compiled in Fig. 2.7. The extent of changes in solar surface within a certain time interval is indicated by changing intensity, whereby blue colors point towards less to almost no changes, and strong variations are depicted in red colors. The strongest variations occur at the borders of the three pores and their immediate surroundings. The most extended variations

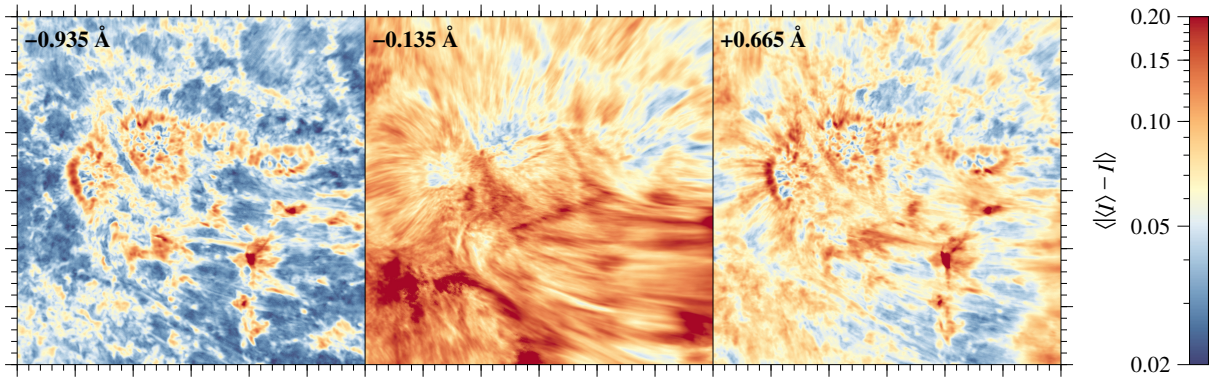


**Figure 2.8** Two-dimensional BaSAMs with an ROI of 30″ × 30″ derived from H$\alpha$ blue line-wing, line core, and red line-wing filtergrams (*left to right*). The color bar indicates the variations for the three wavelength settings on logarithmic scale.

takes place at borders of pores P1 and P2, where in later stages of the sunspot evolution a rudimentary penumbra is formed. In addition, variations around pore P3 are less intense. This pore dissolves before the penumbra formation sets in. The interior of the pores shows little to no variation, and the spatial scale of the variations corresponds to that of umbral dots. This is in stark contrast to the borders of the pores, where horizontal plasma motions and the dynamic interface between the magnetic flux tube and convection contributes to the strong signal in the BaSAM. The variations along the spine of the light bridge are significantly diminished but the interface with the neighboring pores exhibits strong variations connected to diverging motions away from the spine of the light bridge and to outward motions at the ends of the light bridge. The region below pores P1 and P2, which is marked by a black rectangle in Fig. 2.3, has also a strong signal in the BaSAM. This indicates significant variations related to ongoing flux emergence at that location. Elongated features can be seen below the three pores indicating the interaction of positive-polarity pores with the leading negative-polarity pores, which are not covered in the ROI of the TiO images. All things considered, the pores are embedded and connected to an extended magnetic flux system, where continuous interactions are driven by plasma motions.

### Background-subtracted Solar Activity Maps – H$\alpha$ Filtergrams

The average BaSAMs for the H$\alpha$ line-core and two outer line-wing positions are compiled in Fig. 2.8 using the same color scheme as before. In the H$\alpha$ line-core BaSAM, only minor variations are observed inside the pores. However, it is difficult to visualize the pores beneath the overlaying chromospheric filaments. In contrast, the light bridge causes a strong signal in this BaSAM indicating major changes related to this dynamic feature. The changes along the light bridge differ from those of the photospheric TiO BaSAM, pointing to a distinct chromospheric structure of the light bridge. Along the border of pore P1, variations in form of (super-)penumbral filaments are seen in the H$\alpha$ line-core BaSAM, which are not as clearly seen around pores P2 and P3. However, the strongest variations appear in the region below the pores along the elongated arch filaments are rooted as seen in the bright plages in the H$\alpha$ line-core filtergrams (see Fig. 2.5). The strong variations in the arch filaments is a clear indication of ongoing flux emergence lifting plasma during the ascent of the flux tubes, which subsequently drains towards the footpoints. The dynamics in the bright plage region also points to the interaction of small-scale, mixed-polarity features, which contribute to local heating and lead to the strongest variation in the H$\alpha$ line-core BaSAM.

The overall appearance of the outer blue line-wing BaSAM resembles that of the TiO BaSAM. The pores P1, P2, and P3 have a patchy red and blue appearance indicating only small variations, whereas the borders of all three pores are characterized by significant variations, which outlined the pores clearly and formed a ring-like structure encircling the pores. This feature is similar to what is seen in the photospheric TiO BaSAM. The region with flux emergence below the pores i.e., the black rectangle marked in Fig. 2.3, also has high values. The spine of the light bridge shows low values suggesting a rather stable configuration.

The outer red line-wing BaSAM has an appearance drawing from features of H$\alpha$ line-core, H$\alpha$ blue line-wing, and TiO BaSAMs. The main difference with respect to the H$\alpha$ blue-wing BaSAM is the

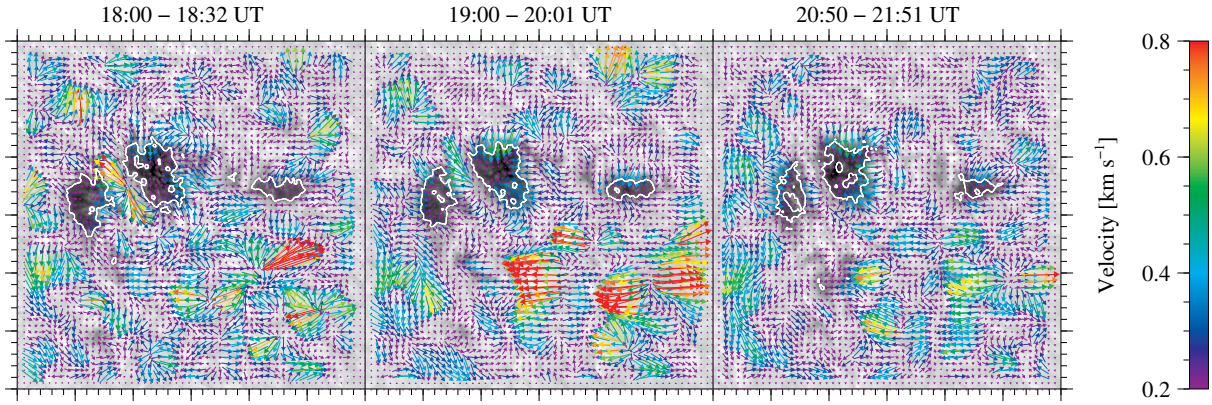


**Figure 2.9** Two-dimensional LCT maps with an ROI of 30″ × 30″ show the photospheric horizontal proper motions for the three time periods indicated above each panel. Rainbow-colored arrows refer to magnitude and direction of the average flow vectors, which are superposed on a time-averaged TiO image. The white contour outlines the umbra seen in corresponding TiO image for intensities lower than 0.8.

presence of penumbra-like filamentary structure around pores and the arch filament in the region below the pores. Here, the pores have also strong variations encircling them. The periphery of the light bridge also exhibits strong variations at the interface to pores P1 and P2. The footpoint region of the arch filaments shows also strong variations in the BaSAMs. The web-like structure as seen in TiO is also faintly visible in the region below the arch filaments due to the low opacity in the outer H$\alpha$ line-wing filtergrams.

### 2.3.3 Velocity Structure in and around Pores

The velocity structure in and around the pores P1, P2, and P3 is traced in the photosphere and chromosphere using LCT to derive horizontal proper motions. However, only for the chromospheric H$\alpha$ line scans, the velocity structure can be expanded to three dimensions based on Doppler velocities. Accordingly, the observational results regarding the height dependent horizontal proper motions along with the chromospheric Doppler velocities are presented in the following sections.

#### Photospheric Horizontal Proper Motions in TiO Images

In Fig. 2.9, averaged LCT velocities derived from TiO time-series are superposed on the corresponding time-averaged TiO image. The rainbow-colored arrows indicate speed and the direction of the proper motions. As described in Sect. 2.2, the three time periods refer to the different stages of pore's evolution. The surroundings of the pores have the usual granulation flow pattern characterized by divergence centers. However, typical inflows are detected at the boundaries of all pores in all three time-series. The ubiquitous inflows around pore P1 reach a maximum during the third time-series. The pore P2 shows strong inflows during the entire time-series, especially at the right side facing P3. The inflows are also strong on the right side of pore P3. In general, the inflows around all pores are persistent throughout the observations.

The TiO and H$\alpha$ BaSAMs help to identify the locations of strong variations, which coincide with the locations of significant proper motions. The most interesting flow features belong to pores P1 and P2. Along the light bridge, between pores P1 and P2, diverging motions are present. This flow pattern runs along the light bridge and is directed towards the interface with the pores on both sides. This also leaves a strong variation in average BaSAMs. This flow pattern remains present in all three time-series but is most prominent in the first, where it has a mean velocity of $(0.40 \pm 0.23)$ km s$^{-1}$. The corresponding average velocity decreases over the next hours, dropping to $(0.27 \pm 0.14)$ km s$^{-1}$ for the third time-series. The standard deviation in these measurements refers to the variation in the observed region rather than presenting a formal error of the measurement.

Another prominent flow feature is associated with newly emerging flux at the bottom of pores P1, P2, and P3. This region also has a strong signal in the TiO and H$\alpha$ BaSAMs. In all three LCT maps, this appears as a large diverging flow pattern. This region expands over time. In the first time-series, the region has three divergence centers at coordinates (15″, 8″), (21″, 10″), and (26″, 6″), which coincides

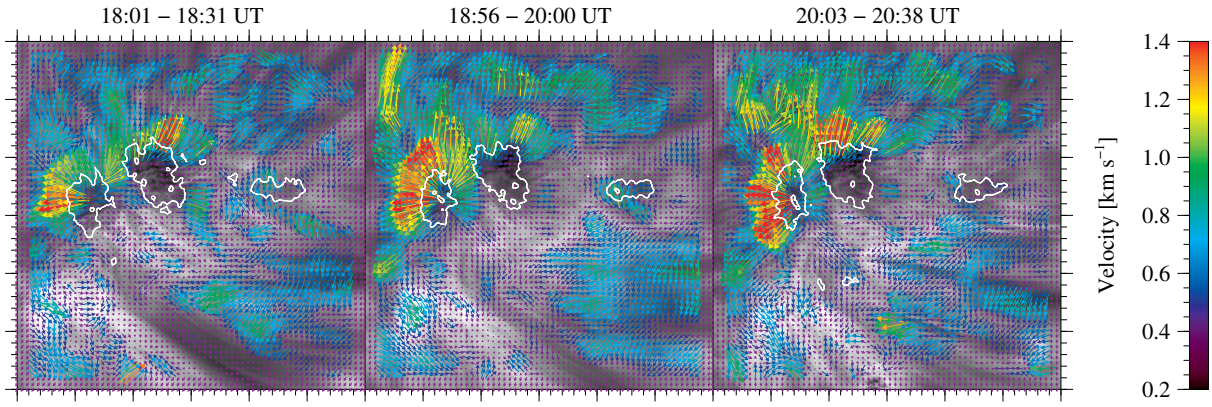


**Figure 2.10** Two-dimensional LCT maps with an ROI of $30'' \times 30''$ show the chromospheric horizontal proper motions for the three time periods indicated above each panel. Rainbow-colored arrows refer to magnitude and direction of the average flow vectors, which are superposed on a time-averaged H$\alpha$ line core filtergram. The white contour outlines the umbra seen in corresponding TiO images for intensities lower than 0.8.

with strong BaSAM signals in TiO and the H$\alpha$ blue and red wings. When referring to coordinates, the origin of the coordinate system is always assumed to be at the lower-left corner.

During the second time-series, the flow fields become more extended and strong. Especially, the region, which connects both polarities of the active region exhibits considerably large velocities associated with the expanding granules. The average LCT velocity in the region increases from $(0.30 \pm 0.19)$ km s$^{-1}$ to $(0.37 \pm 0.25)$ km s$^{-1}$ from the first to the second time-series. By the end of the high-resolution observations, the flow feature is still present but with a significantly reduced average velocity of $(0.27 \pm 0.14)$ km s$^{-1}$.

### Chromospheric Horizontal Proper Motions in H$\alpha$ Filtergrams

The application of LCT and its shortcomings with regard to H$\alpha$ images are discussed and demonstrated in Chae *et al.* (2000). The results of applying LCT to H$\alpha$ line-core images are presented in Fig. 2.10. The visual appearance of the H$\alpha$ LCT maps is very different compared to the TiO LCT maps. The ROI is devoid of divergence centers in the surroundings of the pores. The inward motions towards the pores boundary, as seen in the TiO maps, are absent in the chromospheric counterpart. Instead strong radial outflows originate from the center of the pores and encircle the pores P1 and P2 with an average velocity of $(0.68 \pm 0.27)$ km s$^{-1}$ and $(0.51 \pm 0.32)$ km s$^{-1}$, respectively. The radial outward flow increases and extends further during the second time-series, where the average velocity around both pores increases to $(0.84 \pm 0.32)$ km s$^{-1}$ and $(0.53 \pm 0.23)$ km s$^{-1}$, respectively. The radial outward motions persist during the third time-series with average values of $(0.65 \pm 0.34)$ km s$^{-1}$ and $(0.62 \pm 0.35)$ km s$^{-1}$, respectively. For both pores, at the location where the outward motion terminates, a second row of outward flow starts, which continues further even extending beyond the edge of the ROI. In contrast, small inward motions are seen around pore P3. On the southern side, where P1 and P2 face the new flux emergence, well-ordered motions are absent.

The southern part of the ROI, which has large diverging motions in the photosphere, displays a different pattern in the H$\alpha$ flow maps. The horizontal proper motions are diminished along the dominant arch filament joining the positive and negative polarity of the active region. However, strong proper motions are traced in the region to the left of the arch filament. The overall orientation of the flow pattern is towards the dominant arch filament. This flow pattern is along the smaller and fast-evolving filaments. In contrast, the region on the right side of the arch filament, which showed brightenings in line core images, exhibits flows directed toward the newly emerging pores, which becomes more streamlined during the second time-series.

### Chromospheric H$\alpha$ Doppler Velocity

The H$\alpha$ Doppler velocities are yet another facet of the dynamic environment encompassing the pores. The exact location of pores is difficult to locate under the veil of the chromospheric filamentary structure. Thus, the contours extracted from the TiO images are added to the H$\alpha$ Doppler maps to improve the

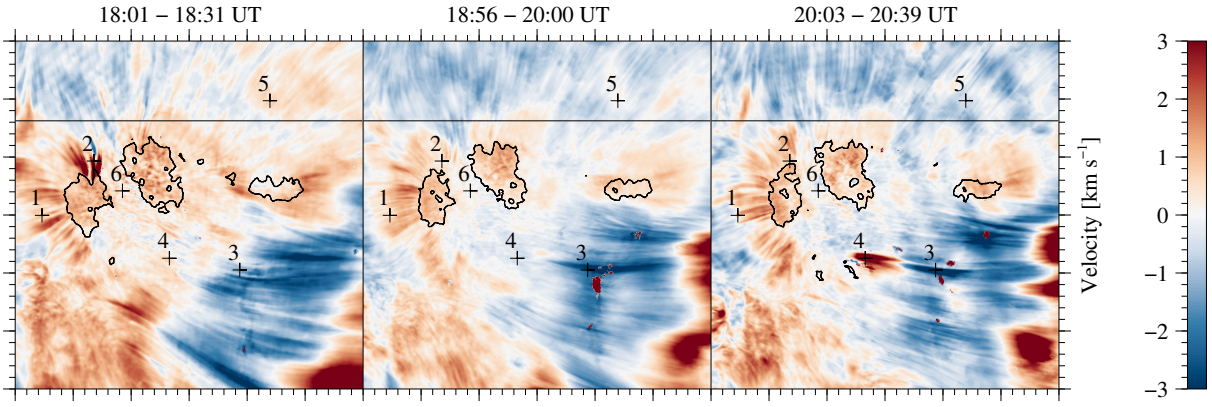


**Figure 2.11** Two-dimensional maps with an ROI of 30″ × 30″ show the chromospheric H$\alpha$ Doppler velocities for the three time periods indicated above each panel. The velocities are clipped at ±3 km s$^{-1}$. The positions labeled 1 – 6 refer to H$\alpha$ Doppler velocities listed in Table 2.1. The black contour outlines the umbra seen in corresponding TiO images for intensities lower than 0.8. The region above the black horizontal line is used to compute the average quiet-Sun Doppler velocity.

| Time | Position | Mean velocity |
|---|---|---|
| 18:01 – 18:31 UT | 1 | (0.89 ± 0.47) km s$^{-1}$ |
| | 2 | (2.06 ± 1.30) km s$^{-1}$ |
| | 3 | (−1.32 ± 0.42) km s$^{-1}$ |
| | 4 | (0.53 ± 0.79) km s$^{-1}$ |
| | 5 | (0.70 ± 0.34) km s$^{-1}$ |
| | 6 | (0.19 ± 1.38) km s$^{-1}$ |
| 18:56 – 20:00 UT | 1 | (0.35 ± 0.52) km s$^{-1}$ |
| | 2 | (0.16 ± 0.48) km s$^{-1}$ |
| | 3 | (−2.90 ± 0.76) km s$^{-1}$ |
| | 4 | (−0.31 ± 0.69) km s$^{-1}$ |
| | 5 | (0.09 ± 0.29) km s$^{-1}$ |
| | 6 | (0.09 ± 0.97) km s$^{-1}$ |
| 20:03 – 20:39 UT | 1 | (0.82 ± 0.89) km s$^{-1}$ |
| | 2 | (0.90 ± 0.74) km s$^{-1}$ |
| | 3 | (−3.33 ± 0.98) km s$^{-1}$ |
| | 4 | (6.08 ± 2.21) km s$^{-1}$ |
| | 5 | (−0.56 ± 0.37) km s$^{-1}$ |
| | 6 | (−0.14 ± 0.85) km s$^{-1}$ |

**Table 2.1** H$\alpha$ Doppler velocities for six selected regions with a size of about 3″ × 3″. The positions are marked in Fig. 2.11

visualization. The average Doppler velocity maps for three time-series are displayed in Fig. 2.11. The velocities are scaled between ± 3 km s$^{-1}$. The inner borders of pores P1, P2, and P3 are predominantly characterized by blue shifts. In all three-time averages, radial redshifts along filamentary structures can be seen, i.e., around pore P1, except for the side facing the light bridge, and not so prominent around pores P2 and P3. At the upper end of the light bridge and at pore P1, a twisting filamentary structure is revealed by alternating red- and blueshifts. This feature is associated with a jet that is eventually ejected. A similar jet-like feature is seen at the upper edge of pore P2. However, the velocity pattern along the light bridge appears to be more or less of granular nature.

The lower part of the ROI is dominated by blueshifts along the arch filaments, which connect the trailing and leading pores of the active region. The footpoints, which coincide with the flux emergence site at the bottom of pores P1 and P2, show strong redshifts in the first and third time-series depicted in Fig. 2.11, respectively. The location of these redshifts matches the strong variations in the TiO and H$\alpha$ BaSAMs.

To demonstrate variations in chromospheric Doppler velocities, Tab. 2.1 compiles mean values and standard deviation for six regions. The labeled plus signs in in Fig. 2.11 mark these regions with a

size $3'' \times 3''$. Regions 1 and 2 belong to two of the chromospheric penumbral filaments of pore P1. Throughout the observations, the Doppler velocity in both regions remains strongly redshifted. The velocity in region 1 changes from $(0.89 \pm 0.47)$ km s$^{-1}$ to $(0.82 \pm 0.89)$ km s$^{-1}$ from the first to the third time-series. Region 2 starts with a high velocity $(2.06 \pm 1.30)$ km s$^{-1}$ in first time-series, which drops in the second time-series but rises again in the third time-series to $(0.90 \pm 0.74)$ km s$^{-1}$. Regions 3 and 4 are situated in the region with continuously emerging flux below the pores. Region 3 is located at the apex of one of the arch filaments, whereas region 4 marks the location of the footpoint. As expected from an arch filament system, the Doppler velocity remains blue and redshifted in regions 3, where the rising flux tube is loaded with plasma, which subsequently drains towards the footpoint in region 4. The Doppler velocity in region 3 more than doubles from $(-1.32 \pm 0.42)$ km s$^{-1}$ to $(-3.33 \pm 0.42)$ km s$^{-1}$ from first the first to the third time-series. This increase in upflow coincides with the rapid increase in downflows at region 4 indicating plasma draining from the flux tube at the footpoint. By the third time-series, the Dopler velocity in region 4 reaches up to $(6.08 \pm 2.21)$ km s$^{-1}$. Region 5 is located in the region, where the second layer of outward motions begins in the H$\alpha$ flow maps. This region starts with a redshift in the first time-series $(0.70 \pm 0.34)$ km s$^{-1}$, which drops somewhat in the second time-series finally, before changing to a blueshifted velocity of $(-0.56 \pm 0.37)$ km s$^{-1}$. Region 6 belongs to the inner part of the light bridge and has throughout the observations very low Doppler velocities.

## 2.4 Discussion

The presented data show a dynamic interplay of magnetic fields and plasma flows. The region contains dark pores lacking a penumbra, where a thick light bridge with a granulation-like pattern separates two dark cores. The FOV covers the trailing part of an active region, which later develops into sunspots surrounded partially by penumbrae. This is an atypical behaviour because usually the trailing part decays first. In addition, the light bridge stays in its original location and retains its overall appearance.

The pores did not develop a penumbra during the GST observations. Over the three-hour peroid, TiO images display no obvious indication of penumbral filaments around any of the pores. However, pores P1 and P2 have corrugated borders. Furthermore, the upper half of both pores P1 and P2 does show extended filamentary extrusions. Sobotka *et al.* (2013) presented similar observation but for an isolated pore. They concluded based on photospheric and chromospheric data that a photospheric penumbra is not a necessary prerequisite for the formation of a superpenumbra. In the present case, superpenumbral filaments are evident in H$\alpha$ filtergrams. However, the pores are part of a larger magnetic system with continuous flux emergence. The formation of a sunspot penumbra is a slow process (e.g., Schlichenmaier *et al.* 2010b), whereas penumbral decay can either be rapid (e.g., flare induced, Wang *et al.* 2004; Deng *et al.* 2005; Verma 2018) or slow (e.g., Verma *et al.* 2018b). Penumbra formation around the pore can be either assisted or hampered by the changes in the surrounding magnetic field. For example, Verma *et al.* (2016a) found that newly emerging flux and intruding positive polarity hampered the formation of penumbra around a negative-polarity sunspot, and the penumbra formed once the flux emergence ceased. The pores P1 and P2 also developed the penumbra at the later stages of evolution, which was unfortunately not covered by the high-resolution observations.

Apart from continuous flux emergence the overlaying magnetic canopy also plays a role in the appearance of penumbrae in the photosphere. In H$\alpha$ filtergrams, superpenumbral filaments or fibrils appear around the pores, which subsequently develop penumbrae. Shimizu, Ichimoto, and Suematsu (2012) conclude based on chromospheric Ca II H filtergrams, which show an annular structure even before the appearance of a photospheric penumbra, that the magnetic canopy plays an important role in the formation of penumbrae. Jing *et al.* (2019) find that the flows in these fibrils do not arise from an oscillation or wave phenomenon but are rather similar to the inverse Evershed flow in the chromosphere. Using a three-dimensional potential field model, they conclude that the pore and the encircling fibrils are part of the magnetically confined system, which maintains the dynamics of superpenumbral fibrils. In the present case, the pore is not simple but two pores with a granular light bridge are involved. The superpenumbral filaments around pores P1 and P2 display inverse Evershed flows, as derived from LOS velocities, at least on the side that is not facing the leading negative polarity. The inverse Evershed flows are a completely different physical phenomenon as the Evershed flow (e.g., Beck, Choudhary, and

Ranganathan 2020). Murabito *et al.* (2016) observed the penumbra is formed by magnetic flux dragged down from the overlaying canopy surrounding the initial pore. In addition, they noticed that the Evershed flow starts when the sinking magnetic field dips below the solar surface and magnetoconvection sets in.

Light bridges can be broadly categorized into two types: narrow light bridges more like penumbral filaments (Louis *et al.* 2008; Rimmele 2008; Bharti 2015; Hou *et al.* 2020) and granular light bridges (Sobotka *et al.* 2013; Lagg *et al.* 2014). A statistical study of light bridges by Li *et al.* (2021) based on SDO data summarizes three ways of light bridge formation. Of these three, the one which fits the observed light bridge best is the scenario, where the merging of two sunspots results in the formation of a light bridge. Once the pores develop into a sunspot, it never formed a penumbra at the location of the light bridge. This is very well in agreement with the conclusions of Künzel (1969), who reported that same-polarity sunspots facing each other never develop a penumbra in between, and often the interface between the spots is marked with a thick granular light bridge. The morphology of the present light bridge matches these descriptions. Granular light bridges usually exhibit vigorous convective motions as described by, for example, Lagg *et al.* (2014). They found that the field-free regions of a granular light bridge are dominated by upflowing plasma with velocities of up to 2 km $s^{-1}$, whereas the interface with the umbrae was dominated by downflows of up to 10 km $s^{-1}$.

The formation of a light bridge in an emerging flux region is discussed in Toriumi, Cheung, and Katsukawa (2015) using numerical simulations and observations. The authors constructed a physical picture of light bridge formation (see Fig. 9 in Toriumi, Cheung, and Katsukawa 2015). In the present observations, making statements about the convective upflow in the center of the light bridge is difficult due to the lack of photospheric spectropolarimetric data. However, convective motions, which further lead to diverging bi-directional horizontal flows in the light bridge as suggested by Toriumi, Cheung, and Katsukawa (2015), are seen in the high-resolution TiO horizontal flow maps. Horizontal velocities of up to 0.89 km $s^{-1}$ (first time-series) were measured. This diverging flow pattern recedes in the next two time-series indicating that the convective upflows decrease over time. In chromospheric horizontal flow maps, confirming these motions is difficult due to the chromospheric filamentary structure overshadowing the photospheric light bridge.

Even though the light bridge displays a granular structure, signs of photospheric convection (e.g. Lagg *et al.* 2014) cannot be confirmed because only chromospheric LOS velocities are available, which show granular patterns to some extent but not as clearly as in slit-reconstructed Doppler maps of photospheric spectral lines. Light bridges are also marked as the location of various types of small-scale energetic activity such as jets (e.g., Tian *et al.* 2018; Robustini *et al.* 2016; Louis 2015). In photospheric as well as in three chromospheric BaSAMs, various small-scale variations along the observed light bridge are evident. However, jet-like phenomena are absent. Yet, the upper edge of the light bridge coincides with the borders of pores P1 and P2, where twisted motions are visible along two superpenumbral filaments.

The BaSAMs were created to follow the intricate changes in pores and their surroundings. The BaSAMs are computed for the first time for high-resolution images from ground-based telescopes. In earlier applications, they were applied to space mission data namely from Hinode and SDO. The photospheric BaSAMs reveal the location of the strongest variations at the borders of pores, the region along the light bridge, and the region below pores with continuous flux emergence. The usual spoke-like structure seen around pores and sunspots connecting them to surrounding sunpergranular cells, as seen by (Verma and Denker 2012; Verma, Kummerow, and Denker 2018a), was absent in the present observations. However, the FOV is small and the supergranular cell, where the pores are situated, is not covered in the observations. Furthermore, the generated BaSAMs cover only four hours of observations rather than the 12 hours used to create BaSAMs in previous work. However, the chromospheric BaSAMs show especially the chromospheric fibrils arching out from the borders of pores. The blue and red line-wing BaSAMs are virtually identical to photospheric BaSAMS except for the presence of fibrils. The arch filament system connecting the pores to the leading polarity is conspicuous in the line core BaSAMs. Comparing the four BaSAMs exposes different features. The changes along the borders of the pores (photospheric BaSAMs) extend as fibrils emanating from the borders (line-wing BaSAMs) further to superpenumbral fibrils (line-core BaSAMs). Changes in BaSAMs also expose the canopy effect.

The photospheric horizontal proper motions around pores show more inward motions at their borders. These inflows are seen in numerical models (e.g., Cameron *et al.* 2007) as well as in observations (e.g.,

Sankarasubramanian and Rimmele 2003; Sobotka *et al.* 2012). However, in the absence of photospheric LOS velocities such downflows cannot be confirmed at the borders of pores. Pores are expected to advect flux from the surroundings, which is transported into the pore by horizontal flows (Stein *et al.* 2011). In photospheric LCT maps, large diverging cells related to expanding granules are present in the light bridge and at the lower-right region of the FOV. In the light bridge, the diverging motion subsides slowly over the course of the observations. In contrast, expanding granules are a common feature in the region connecting the pores to the leading polarity. These diverging motions and expanding granules are closely tied to the region with emerging flux and indicate that new flux rises to the surface (Cheung *et al.* 2010; Verma *et al.* 2016b).

Opposite to the inward horizontal proper motions in the photosphere, chromospheric LCT maps exhibit strong radial outflows around pores P1 and P2. These are associated with the running penumbral waves, where contrast changes give the impression of horizontally propagating plasma (Sobotka *et al.* 2013; Freij *et al.* 2014). In individual maps, the chromospheric LOS velocities trace the superpenumbral fibrils around pores. Average maps show the inverse Evershed flow around pores. The average LOS velocities around pores P1 and P2 are predominately redshifted with $(0.79 \pm 0.63)$ km s$^{-1}$ and $(0.15 \pm 0.54)$ km s$^{-1}$, respectively. This agrees with the previous work and observations, e.g., Haugen (1969) found inflows and downflows near sunspots with an average velocity of 6.8 km s$^{-1}$. Using the Cloud Model (Beckers 1964) to compute the H$\alpha$ velocities for three different heights, Georgakilas and Christopoulou (2003) found that velocities increase with increasing heights. The average velocities close to the H$\alpha$ line core ($\lambda_0 \pm 0.35$ Å) are around 5 km s$^{-1}$. The authors also proposed that the H$\alpha$ velocities are underestimated because of integrating the velocity values over substantial viewing angles. Chae *et al.* (2015) also reports downflows around pores in the range $\pm 3$ km s$^{-1}$ based on H$\alpha$ observations. In addition, two locations with penumbral filament-like intrusions at the upper part of pores P1 and P2, where they meet the light bridge, show twisting motions and even jet-like ejections (Hou *et al.* 2020; Zhang *et al.* 2017). Furthermore, the lower region, where the pores are connected to leading polarity, has a typical arch filament with the typical LOS flow structure, i.e., strong downflows at the footpoints and upflows at the apex of the filament (e.g., González Manrique *et al.* 2018).

Placing the results of this study in context with literature offers the following comprehensive description for consideration. This investigation covered a complex active region, where two flux systems interacted with each other. One was a non-Hale active region with a highly inclined sunspot group tilt angle, in which the other smaller region with a much shallower tilt angle emerged. Despite continuous flux emergence in its proximity and advection of flux, the pore P2 can be traced throughout the time-series of magnetograms. This pore seems to anchor the trailing part of the active region, thus providing a sufficiently stable environment for penumbra formation. Furthermore, it attracted much of the positive-polarity flux of the second emerging flux system, while the negative-polarity flux of both flux systems evolved in isolation, which is assisted by the fast break off of the leading pores and sunspots. The interaction of the two flux systems also explains that a larger, compact umbra could not be formed, i.e., the umbral cores maintained their identity and light bridges are a common feature in the evolution of the trailing pores and sunspots. This fragmented appearance is also evident in the rudimentary penumbrae and in the abundance of umbral dots (Watanabe *et al.* 2012), which are all signs that convection significantly interacts with the flux system.

The penumbra formation is not covered by the high-resolution observations. Nevertheless, they provide important clues that penumbra formation is imminent. Photospheric BaSAMs show first indications that the trailing pores begin to interact with the surrounding supergranular cell, which is very similar to observations by Verma, Kummerow, and Denker (2018a) for axis-symmetric sunspots, where such a connection was clearly established. The question "Is the interaction of pores and subsequently sunspots with the surrounding supergranular cell a prerequisite for penumbra formation?" is a worthwhile endeavor and warrants future scrutiny in a statistical study based on SDO data. The chromospheric H$\alpha$ observations further suggest impending penumbra formation, e.g., curved filamentary extrusions with indications of twist and more importantly a semi-circular region with superpenumbral filaments, which already starts at the border of the pores and exhibits the inverse Evershed flow.

Counter-agents of penumbra formation are also present in the trailing part of the active region, namely continuous flux emergence and strong light bridges. While studies found that penumbral formation is being hampered at the flux emergence site (Schlichenmaier *et al.* 2010a; Schlichenmaier, Rezaei, and González

2012; Rezaei, Bello González, and Schlichenmaier 2012), other studies found penumbra formation at the side facing flux emergence (Lim *et al.* 2013; Murabito *et al.* 2017). Thus, high-resolution case studies leave an inconclusive picture for this aspect of penumbra formation. Again, future statistical studies based on SDO could resolve this ambiguity. The fine structure of strong light bridges, however, evades scrutiny of full-disk observations with moderate spatial resolution. Strong light bridges are characterized by diverging motions perpendicular to the axis of the light bridge and strong horizontal outward motions at their ends. Due to the deep convective upflow in the center of the light bridge (Toriumi, Cheung, and Katsukawa 2015), upwelling material is almost squeezed outwards into the surrounding granulation. The two components of horizontal proper motions inside the light bridge become weaker towards the end of the high-resolution time-series, so that their impact on penumbra formation is diminished. Time-series of magnetograms also imply that the strong light bridge becomes thinner with time. In addition, time-series of SDO/HMI vector magnetograms were consulted to validate that the field-free gap between the pores, i.e., the strong light bridge, thins out with time. This holds true for both the horizontal and vertical components of the magnetic field. The omnipresent thin hairlines, first mentioned by Scharmer *et al.* (2002), at the interfaces between light bridge and pores could be considered as an attempt to form a penumbra. However, the extremely limited space within the light bridge makes it impossible to establish flux tubes carrying the Evershed flow. Note that such hairlines were absent at the border between the pores and the surrounding granulation.

## 2.5 Summary and Conclusions

Combining ground-based high-resolution GST observations with synoptic SDO/HMI data enables scrutinizing important phases in the evolution of active regions. The bipolar region NOAA 12317 presented a rather atypical behavior, as the leading pore decayed, while the trailing part evolved further into a sunspot. Its evolution in terms of plasma flows and connectivity was followed and analyzed using LCT and BaSAMs, whereby the latter method was applied for the first time to high-resolution.

The emergence and evolution of active regions result in very dynamic behavior. In the photosphere, converging and diverging motion can be observed in close proximity. At the boundaries of pores with strong magnetic fields, inflows can be observed that can be related to downflows as indicated by the Doppler velocity maps. Despite the downward movement detected above the dark umbral cores at the photosphere, an asymmetric radial outflow was identified by LCT analysis of chromospheric H$\alpha$ filtergrams.

The photospheric divergence centers recognized by LCT are evidence of exploding or expanding granules, usually observed in proximity to pores and sunspots with region of ongoing flux emergence. Especially the area connecting both polarities exhibits strong structural changes induced by exploding granules. In the chromosphere, where divergence centers are no longer traceable, this region is characterized by upflows. However, horizontal proper motions appear to be the main driver of structural change at this location, as is evident in chromospheric BaSAMs.

The current work includes the high-resolution photospheric images and chromospheric filtergrams in addition to synoptic continuum images and magnetograms. Their combination addresses important aspects of active region development. However, for a better understanding and a comprehensive description of the three-dimensional flow and velocity structure, more high-resolution observations of newly emerging flux regions are needed – if possible even well before the formation of stable magnetic features has started. Thus, a detailed analysis of the photospheric and chromospheric response becomes possible, i.e., the evolution of velocity and magnetic fields with height in the atmosphere.

# Chapter 3

# Impact of Magnetic and Flow Fields on Penumbrae and Light Bridges of Three Leading Sunspots in an Active Region

## 3.1 Introduction

Solar active regions consist of a variety of features caused by rising magnetic flux with various field strengths, lifetimes, and spatial dimensions. Magnetic knots are granule-sized dark patches caused by relatively weak field strengths in the order of several 100 G and up to kilo-Gauss fields (Frazier and Stenflo 1978; Solanki 1993). Pores are larger in size with stronger fields in the range of 600 G – 1800 G (Sütterlin 1998; Verma and Denker 2014), which is approximately the observed field strength at the outer edge of the penumbra (Livingston 2002). The penumbra is the differentiating feature between pores and sunspots (Rucklidge, Schmidt, and Weiss 1995; Leka and Skumanich 1998). The field strength in the umbral cores of sunspots is in the range of 1800 G – 3700 G (Livingston 2002). Inflows can be observed at the borders of the pores, and the region connecting positive and negative-polarity typically contains large divergence centers caused by expanding granules. The transition from pore to sunspot is characterized by a variety of flows. For example, the moat flow (Vargas Domínguez *et al.* 2008), where the flow field is axially symmetric for sunspots with a fully developed penumbra (Löhner-Böttcher and Schlichenmaier 2013), exhibits a significant east–west asymmetry because of the sunspot's motion as a whole relative to the surroundings (Verma, Kummerow, and Denker 2018a). This asymmetry can be modified by the tilt angle of the active region and the presence of plage in the surroundings. Even in light of these detailed descriptions of sunspot penumbrae, many questions remain open: How do penumbral filaments become a stable feature of sunspots? How are Evershed and moat flows connected to penumbral filaments and where do the flows terminate? Does the magnetic field topology have an impact on penumbra formation and decay?

Light bridges appear as bright, long, and mostly narrow structures in the umbra. They are associated with the formation or decay of active regions, and recent simulations have shown that they form as a consequence of plasma intrusions at a certain depth, which are successively transported to the surface by upflows (Panja, Cameron, and Solanki 2021). According to Liu and Liu (2015), light bridges can be distinguished from the surrounding umbra by their weaker and more inclined fields. Therefore, it is necessary to consider the umbra and light bridges as two different systems. Jing *et al.* (2023) emphasized that the appearance and magnetic properties of light bridges depend on how much they are squeezed by the surrounding umbral magnetic field. The formation of light bridges has been linked to plasma ejections and chromospheric H$\alpha$ surges (Roy 1973; Bharti, Joshi, and Jaaffrey 2007; Pietrow *et al.* 2022), adding them to the list of possible chromospheric heating mechanisms. After becoming visible at the surface, light bridges extend as a canopy structure into higher atmospheric layers. Several questions related to the relationship between sunspots and light bridges require further investigation: How do the appearance and evolution of light bridges affect the formation or decay of a penumbra? How do the physical properties of light bridges such as temperature change with the evolutionary stage of the sunspot?

This study investigates flows and magnetic fields in a complex active region with three leading sunspots containing light bridges, observed in several spectral regions covering the photosphere and chromosphere. Besides imaging data, spectropolarimetric data are analyzed. The observations and data processing are described in Section 3.2. The results of the data analysis are presented in Section 3.3, and their discussion follows in Section 3.4. Section 3.5 summarizes the findings of this study and emphasizes the need for further investigations of magnetic and flow fields in and around active regions.

## 3.2 Observations and Data Reduction

This section describes the recording, reduction, and analysis of high-resolution data from the 1.5-meter GREGOR solar telescope (Schmidt *et al.* 2012; Kleint *et al.* 2020) and synoptic data from the Solar Dynamics Observatory (SDO, Pesnell, Thompson, and Chamberlin 2012). In addition, it includes details on instruments, observing settings, and methods.

### 3.2.1 Observations

The high-resolution observations were carried out with the GREGOR telescope at Observatory del Teide, Izaña, Tenerife, Spain from 07:44 UT to 09:14 UT on 2022 September 9. The GREGOR Adaptive Optics System (GAOS, Berkefeld *et al.* 2012) provided real-time image correction of images and spectra. The updated "sTools" data processing pipeline (Kuckein *et al.* 2017) was used for image processing and image restoration. The observations focused on the leading part of the active region NOAA 13096. The region was classified by the *SolarMonitor* (Gallagher, Moon, and Wang 2002) web service[1] as a $\beta$-region according to the Mount Wilson classification (Hale *et al.* 1919). The GREGOR observations covered the three leading, positive-polarity sunspots with a partial penumbra, while the trailing negative-polarity sunspot with a complete penumbra was not included because of the limited field-of-view (FOV) of the GREGOR instruments and the required high cadence, which ruled out taking a mosaic of the active region. At the time of the observations, the active region was located at a heliocentric angle corresponding to $\mu = \cos\theta = 0.77$.

Synoptic data were provided by the Helioseismic and Magnetic Imager (HMI, Scherrer *et al.* 2012; Schou *et al.* 2012) onboard SDO. Standard data processing routines were used for the conversion of Level 1.0 to Level 1.5 data. Accordingly, the initial pixel scale of $0.5''$ pixel$^{-1}$ of HMI data was adjusted to $0.6''$ pixel$^{-1}$. Further processing of HMI continuum images and magnetograms was carried out as described in Beauregard, Verma, and Denker (2012) and Verma (2018), which includes the correction for solar differential rotation. Figure 3.1 displays continuum images and magnetograms at the beginning and end of the high-resolution observations. The FOV is $120'' \times 120''$ or $200 \times 200$ pixels, and the heliocentric-Cartesian coordinates are given for the center of the FOV. The continuum and magnetograms were recorded at a cadence of 45 s. The magnetograms are displayed in the range of $\pm 1000$ G. Geometrical foreshortening was not corrected, since the FOV is small.

#### Improved High-resolution Fast Imager

The improved High-resolution Fast Imager (HiFI+, Denker *et al.* 2023a) has six imaging channels for high-resolution solar observations. The instrument successfully passed commissioning and science verification in early 2022 and has since then entered routine observations as one of GREGOR's facility instruments. This is one of the first case studies utilizing HiFI+ as a primary data source. The six channels feature various filters, which cover diagnostically important spectral regions, enabling synchronized high-cadence photospheric and chromospheric observations. Sets of 500 short-exposure images are acquired at frame rates of 49 Hz and 100 Hz depending on the camera model (Imager sCMOS and Imager M-lite 2M), but only the best 100 images are kept for image restoration. Details of the interference filters and of the detectors and their spectral coverage are listed in Table 3.1.

The two channels of the HiFI+ No. 1 Imager sCMOS camera system observe the photosphere in the Fraunhofer G-band (Sánchez Almeida *et al.* 2001) and in the blue continuum, which is strictly not pure

[1] www.solarmonitor.org

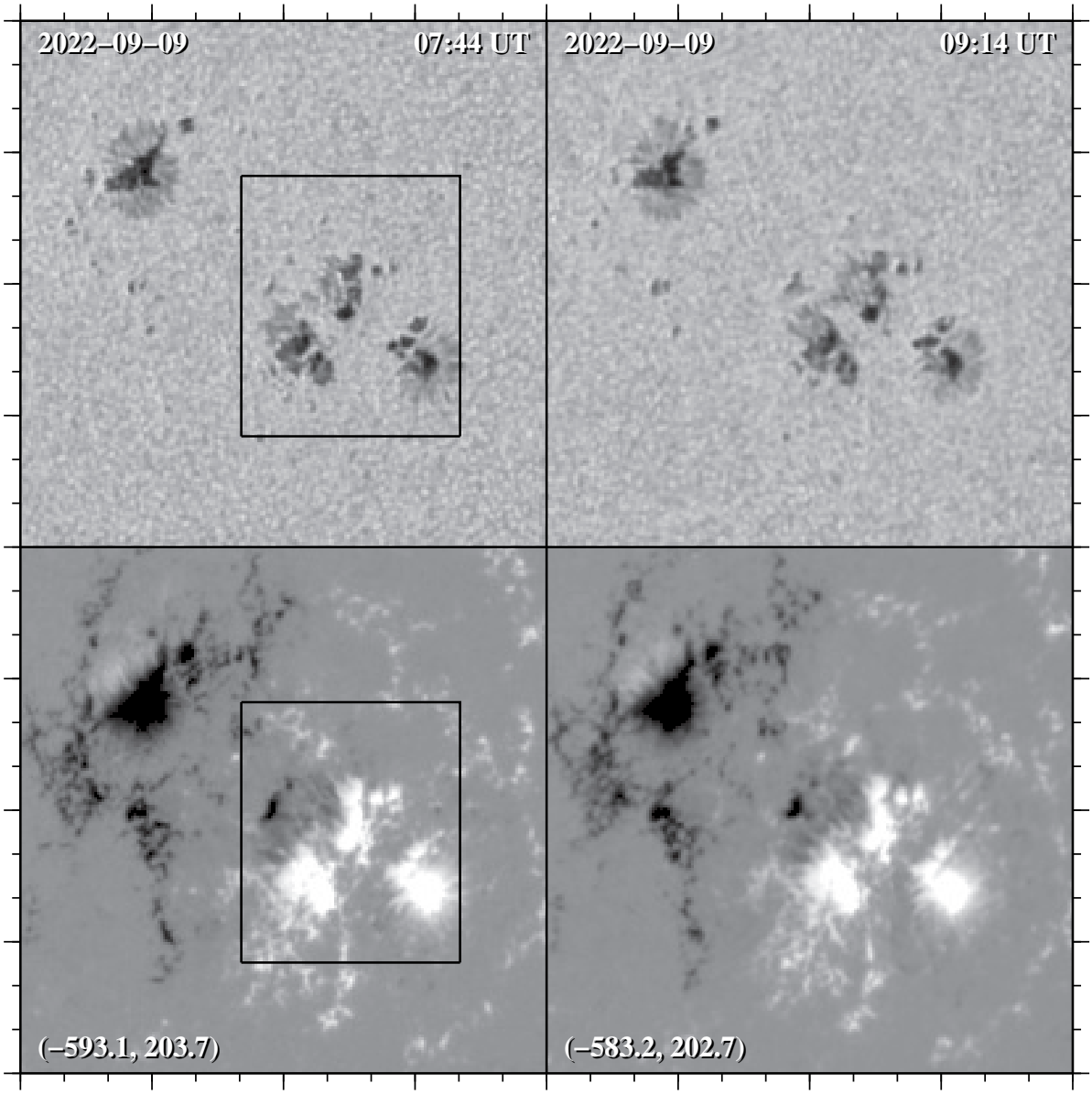


**Figure 3.1** Synoptic HMI continuum images (*top*) and magnetograms (*bottom*) showing the evolution of active region NOAA 13096 from 07:44 UT (*left*) to 09:14 UT (*right*) on 2022 September 9. The FOV is $120'' \times 120''$ (major tick marks are separated by $30''$), and the heliocentric-Cartesian coordinates provided in the bottom-left corners of the magnetogram panels refer to the center of the FOV. The magnetograms are displayed in the range of ±1000 G, where positive and negative polarities are shown in white and black, respectively. The black rectangles refer to the high-resolution observations with GREGOR (see Figure 3.2).

| | Ca II H | G-band | Blue continuum | H$\alpha$ | TiO |
|---|---|---|---|---|---|
| Wavelength $\lambda$ | 396.8 nm | 430.7 nm | 450.6 nm | 656.3 nm | 705.8 nm |
| Passband $\Delta\lambda$ | 1.080 nm | 1.120 nm | 1.150 nm | 0.750 nm | 0.946 nm |
| Diffraction limit $\lambda/D$ | 0.057″ | 0.062″ | 0.065″ | 0.094″ | 0.101″ |
| Max. transmission | 63.8% | 54.4% | 64.5% | 70.0% | 68.8% |
| Plate scale | | 4.25″ mm$^{-1}$ | | 8.50″ mm$^{-1}$ | |
| Pixel scale | 0.025″ pixel$^{-1}$ | 0.028″ pixel$^{-1}$ | | 0.050″ pixel$^{-1}$ | |
| FOV | 48.2″×30.8″ | 70.7″×59.6″ | | 76.5″×60.5″ | |
| Number of pixels | 1936×1216 | 2560×2160 | | 1536×1216 | |
| Frame rate | 100 Hz | 49 Hz | | 100 Hz | |

**Table 3.1** Characteristics of HiFI+ interference filters and cameras (see Tables 1 & 2 in Denker *et al.* 2023a).

continuum but a spectral region where the line density is small (Denker *et al.* 2023a). The larger detector format and the camera interface result in an image acquisition rate of 49 Hz, and thus the cadence is 12 s for datasets used in image restoration. The four channels of the HiFI+ No. 2 and No. 3 Imager M-lite 2M camera systems observe chromospheric Ca II H images (Carlsson, De Pontieu, and Hansteen 2019), broad-

and narrow-band chromospheric H$\alpha$ images (Cauzzi *et al.* 2009; Leenaarts, Carlsson, and Rouppe van der Voort 2012; de la Cruz Rodríguez *et al.* 2019), and photospheric TiO images (Riethmüller *et al.* 2008). The image acquisition rate for these cameras is 100 Hz, and thus the cadence is 6 s for datasets used in image restoration. The Ca II H camera is located in the blue arm of HiFI+ so that the full detector size can be used because of the smaller plate scale. In the red arm of HiFI+, a smaller part of the detector is used because the beam diameter is limited to 100″. A Halle Lyot filter with a bandpass of 60 pm is used to isolate the line core of the strong chromospheric H$\alpha$ absorption line.

An overview of HiFI+ observations is presented in Figure 3.2 displaying Ca II H, G-band, blue continuum, broad- and narrow-band H$\alpha$, and TiO speckle-restored images. The data were recorded at about 08:35 UT under good seeing conditions. The common region-of-interest (ROI), which encompasses three small sunspots with rudimentary penumbrae surrounded by various pores, is used for further data analysis.

#### GREGOR Infrared Spectrograph

The spectropolarimetric data were taken with the GREGOR Infrared Spectrograph (GRIS, Collados *et al.* 2012), a slit-spectrograph capable for full Stokes vector polarimetry. GRIS was updated in 2022, when two spectral channels for multi-wavelength observations were introduced, facilitating spectropolarimetric observations in the 1.0 – 1.8 $\mu$m range and spectroscopic observations in the 2.0 – 2.3 $\mu$m range (Quintero Noda *et al.* 2022b; Regalado Olivares *et al.* 2022). The spectropolarimetric observations on 2022 September 9 focused on the 1083 nm spectral range, which covers three magnetically sensitive spectral lines, that is, the photospheric Si I line at 1082.7 nm (Bard and Carlsson 2008), the deep photospheric Ca I line at 1083.9 nm, and the chromospheric He I triplet at 1083.0 nm (Avrett, Fontenla, and Loeser 1994). The observations were carried out using the long-slit mode. The number of spectral points was $n = 1010$, and the spectral sampling was 1.79 pm pixel$^{-1}$. Two scans were taken with 400 scan steps. The step size was about 0.13″. The pixel scale along the slit was about 0.13″ pixel$^{-1}$. This resulted in a FOV of about 52.0″ × 56.6″. The integration time used for each slit position was 100 ms with ten accumulations at each scan step. Each scan took approximately 40 min. The first and second scans began at 07:44 UT and 08:35 UT, respectively. However, only the second scan is discussed in the following because the AO lost lock during the scan, resulting in a displacement of the observed FOV.

### 3.2.2 Data Reduction

#### Improved High-resolution Fast Imager

The HiFI+ data were split into two time-series covering the time periods from 07:44 UT to 08:24 UT and from 08:35 UT to 09:14 UT due to a gap in the observations. Each set of 100 short-exposure images was restored with the triple correlation or speckle masking technique (Lohmann, Weigelt, and Wirnitzer 1983; Weigelt and Wirnitzer 1983; de Boer 1993; von der Lühe 1993). The sTools data processing pipeline provides an interface to the Kiepenheuer Institute Speckle Interferometry Package (KISIP, Wöger and von der Lühe 2008; Wöger, von der Lühe, and Reardon 2008). The restored HiFI+ images were normalized such that the quiet-Sun intensity is unity. Rigid image motion was removed using the two-dimensional cross-correlation between the images and the average image of the time-series. Applying a Lee filter (Lee 1986) smoothes these images and removes the signature of the granulation so that only the position of the major sunspots enters in the cross-correlation. Differential image motion was removed with a destretching algorithm using a 128×128-pixel kernel in the first pass and a 64×64-pixel kernel in the second pass. A sliding average of nine images, centered on the image to be destretched, was used as a reference. Finally, a subsonic filter is applied to the aligned and destretched image cube, taking into consideration the respective plate scales, cadences, and cut-off velocities. The cut-off velocities were chosen as 4 km s$^{-1}$ for photospheric time-series and 15 km s$^{-1}$ for chromospheric time-series. This step removes intensity variations caused by, for example, the five-minute oscillations.

The G-band time-series was used as a reference to align (translation and rotation) the blue continuum, broad-band H$\alpha$, and TiO time-series, since the information content of the mainly photospheric images is similar. Image restoration with Multi-Object Multi-Frame Blind Deconvolution (MOMFBD, Löfdahl 2002; van Noort, Rouppe van der Voort, and Löfdahl 2005) requires mechanical alignment of the broad-

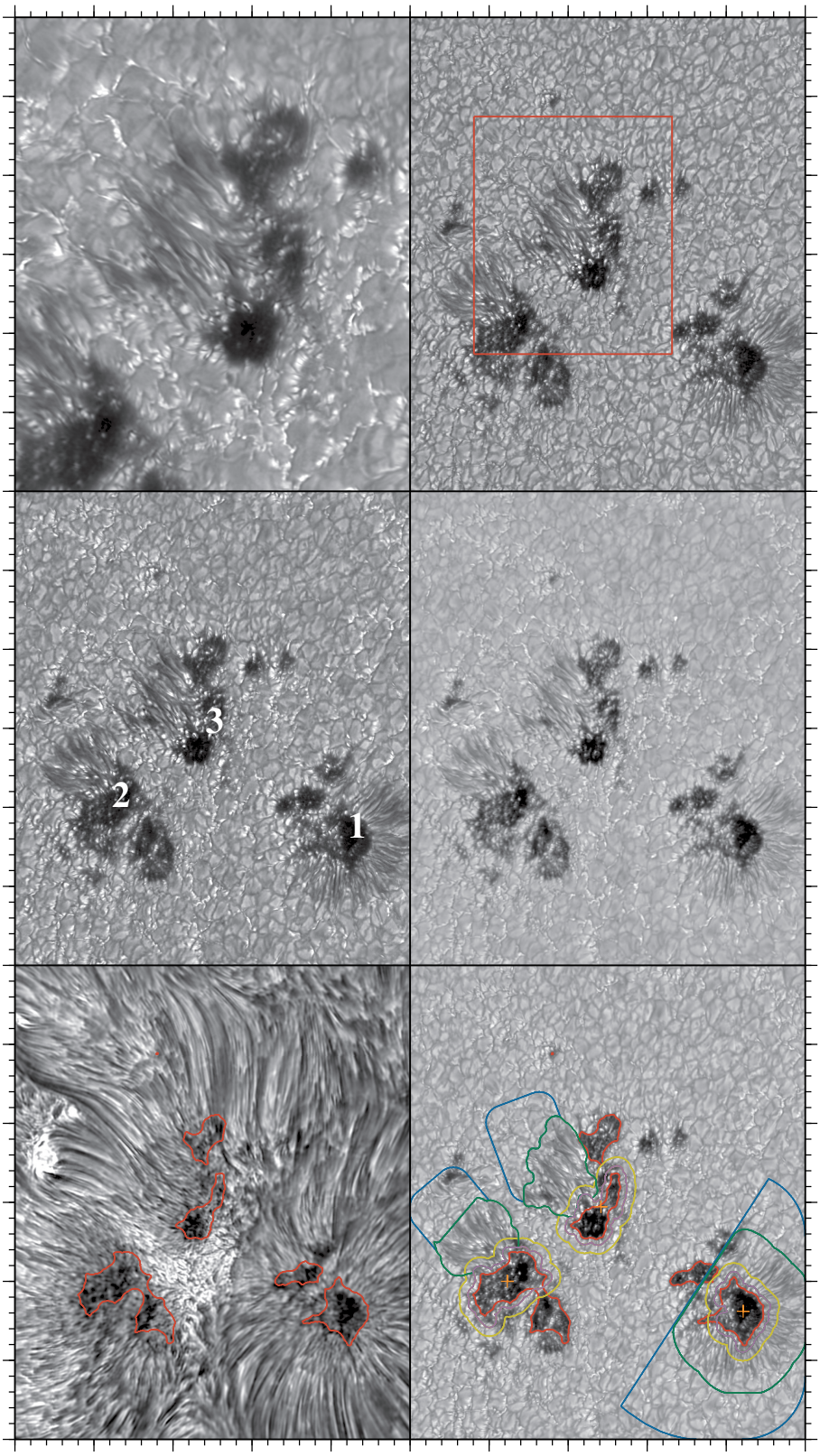


**Figure 3.2** Speckle-restored images of three sunspots obtained by the six HiFI+ cameras at about 08:35 UT on 2022 September 9, that is, Ca II H (*top-left*), G-band (*top-right*), blue continuum (*middle-left*), broad-band H$\alpha$ (*middle-right*), narrow-band H$\alpha$ (*bottom-left*), and TiO (*bottom-right*) images. A common ROI of $50'' \times 60''$ (major tick marks are separated by $10''$) was extracted from the full FOV, except for the Ca II H image, where the ROI covers only $25'' \times 30''$. The red rectangle in the G-band image indicates the location of the Ca II H FOV. The red contours in the narrow-band H$\alpha$ and TiO images outline the umbrae based on the TiO image, where an intensity threshold of $0.7\,I/I_0$ of the normalized quiet-Sun intensity was used. The contours in the bottom-right panel refer to umbra borders (*purple*), inflow regions at umbra borders (*yellow*), penumbrae (*green*), moat flow regions (*blue*), which were used to determine flow velocities. The orange crosses indicate the center of the umbrae.

and narrow-band H$\alpha$ channels with high accuracy. The technical details for the precise alignment of the cameras are described in Section 2.3 of Denker *et al.* (2023a). As a consequence, no additional alignment step is needed for the narrow-band H$\alpha$ time-series. Finally, the smaller FOV of the Ca II H time-series made use of the locations of two sunspots and one pore within the reduced FOV. In addition, the AO lock point jumped 10 min before the end of the first time-series, introducing a shift of the FOV larger than the cumulative shifts due to random image motions throughout the time-series. All these factors limited the common FOV of the time-series to $55'' \times 65''$. However, for display purposes, this FOV was further cropped to $50'' \times 60''$ and $25'' \times 30''$ for Ca II H as shown in Figure 3.2.

The concept of Background-subtracted Solar Activity Maps (BaSAMs) was introduced by Denker and Verma (2019). These maps are computed to detect variations in and around sunspots and pores and to identify locations, where significant intensity and magnetic field changes occur. This technique collapses an entire time-series into a two-dimensional map, subtracting an average map from individual maps before averaging the resulting maps. Two-dimensional BaSAMs are an effective quantitative tool for visualizing and identifying locations where significant changes occur, as demonstrated by Verma *et al.* (2012) and Verma *et al.* (2020), where BaSAMs were applied to HMI LOS magnetograms and ultraviolet images acquired with the Atmospheric Imaging Assembly (AIA, Lemen *et al.* 2012) on board SDO. Recently, Kamlah *et al.* (2023) showed the first application of BaSAMs to high-resolution data of three pores and a light bridge, and Denker *et al.* (2023b) extended the BaSAM concept to imaging spectroscopic data.

Horizontal proper motions are measured using Local Correlation Tracking (LCT, November and Simon 1988), which is applied to the high-resolution data as described in Verma and Denker (2011). The horizontal velocities for each pixel in the FOV are computed over image tiles with a size of $2.2'' \times 2.2''$, corresponding to about 1600 km × 1600 km on the solar surface. A Gaussian kernel with full-width-at-half-maximum (FWHM) of 1200 km is applied to the image tiles to track granule-sized structures. The size of the sampling window and the width of the Gaussian kernel were kept the same in this study, regardless of the observed solar features and the chosen wavelength channel. Images, separated in time by $\Delta t = 6 \times 6$ s = 36 s (Ca II H, broad- and narrow-band H$\alpha$, TiO) and $\Delta t = 3 \times 12$ s = 36 s (blue continuum and G-band), are used for the LCT computation. The computed flow vectors are averaged over the duration of each time-series, that is, $\Delta T = 40$ min, which minimizes contributions by granules, revealing persistent flow patterns.

### GREGOR Infrared Spectrograph

The initial GRIS data reduction takes place on-site using Version 8 of the GRIS data pipeline (Manuel Collados, private communication). This process includes several steps such as dark-frame subtraction, flat-field correction, crosstalk removal, and calibration of the polarization modulator (Collados 1999). Subsequent data reduction steps such as wavelength calibration and correction for the spectrograph profile, among others, follow the descriptions provided in Verma *et al.* (2016a, 2018b). The "Stokes Inversion based on Response functions" (SIR, Ruiz Cobo and del Toro Iniesta 1992) code was employed to invert spectra of the second scan. The data analysis focuses on the photospheric Si I line at 1082.7 nm ($g_{\rm eff} = 1.5$). The initial model for the Si I line encompasses the optical depth range of $+1.0 \leq \log \tau \leq -5.4$. A limb-darkening factor was incorporated in line with Equation 10 in Pierce, Slaughter, and Weinberger (1977). A constant macroturbulence value of 1 km s$^{-1}$ was assumed. In addition, a fixed stray light contribution of one percent was applied, with this choice acting as a lower limit (Balthasar *et al.* 2016). The inversions yielded the temperature stratification using three nodes $T(\tau)$, while the total magnetic flux density $B_{\rm tot}$, the magnetic field inclination $\gamma$ and azimuth $\phi$, and the Doppler velocity $v_{\rm LOS}$ remained constant with height, that is, each of these physical parameters has only one node. Pixels with a circular and linear degree of polarization below 0.2% were excluded from any subsequent magnetic field analysis. The magnetic azimuth ambiguity was solved by using the best matching Spaceweather HMI Active Region Patch (SHARP, Bobra *et al.* 2014) as initial estimate and then smoothing the azimuth map with iteratively larger windows from a size of $3 \times 3$ pixels up to a size of $23 \times 23$ pixels. Azimuth angles were flipped by 180°, if in 70% of the cases the scalar product between the azimuth angle and all other azimuth angles in the window was larger than 180°.

In addition to the SIR results, the LOS velocities and line-core intensities of the Si I, Ca I, and He I lines were derived using the Fourier phase method (Schmidt, Stix, and Wöhl 1999). For the He I triplet,

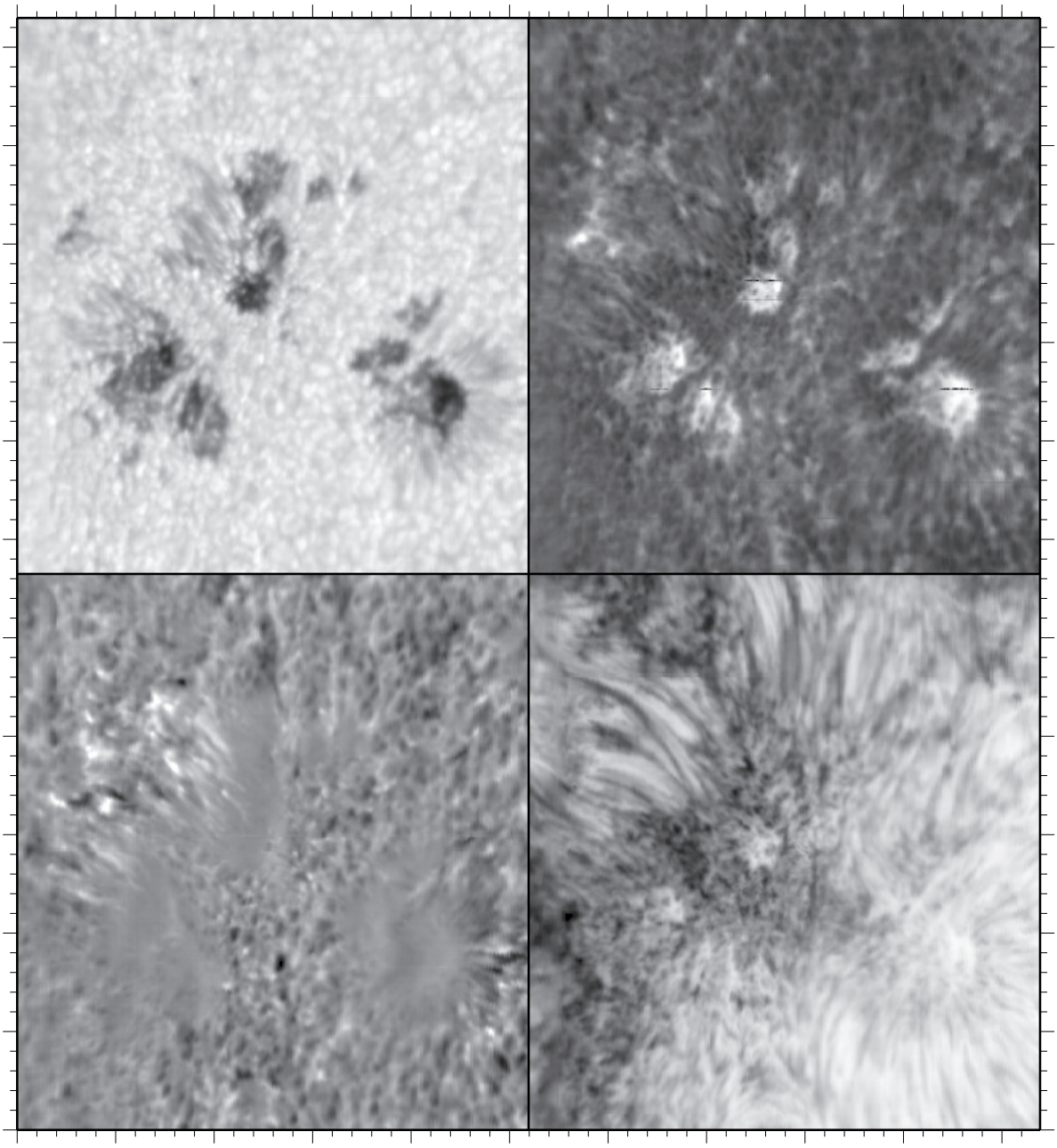

**Figure 3.3** Slit-reconstructed GRIS maps at 08:35 UT of the mean continuum intensity (*top-left*), the Si I line-core intensity (*top-right*), the Si I LOS velocity (*bottom-left*), and the He I line-core intensity (*bottom-right*). The physical parameters are scaled as follows: continuum intensity $I/I_0 \in [0.5, 1.1]$, Si I line-core intensity $I/I_0 \in [0.3, 0.6]$, Si I LOS velocity $\pm 2$ km s$^{-1}$, and He I line-core intensity $I/I_0 \in [0.5, 1.0]$. The FOV is $52.0'' \times 56.6''$, and major tick marks are separated by $10''$.

only the red component was fitted. The average velocity of dark umbral cores served as the reference for the zero point of the LOS velocities. Figure 3.3 compiles a sample of slit-reconstructed GRIS maps, depicting the mean continuum intensity, the Si I line-core intensity, the Si I LOS velocity, and the He I line-core intensity for the second GRIS scan starting at 08:35 UT. All three sunspots of leading polarity are contained in the GRIS FOV.

## 3.3 Results

In this section, the morphology and temporal evolution of the active region are studied using time-series of synoptic and high-resolution data. The magnetic connectivity of the active region is investigated, and

horizontal proper motions and LOS velocities are combined to study the three-dimensional flow field in and around the sunspots.

### 3.3.1 Morphology

The combination of spectral bands observed with HiFI+ allows us to analyze the solar atmosphere at different heights, ranging from the photosphere to the chromosphere. The inclusion of SDO HMI continuum images and magnetograms further extends the analysis. Doppler velocities can be studied by using spectropolarimetric GRIS data covering the deep photosphere, the photosphere, and the chromosphere.

On 2022 September 6, active region NOAA 13096 was close to the eastern limb and was identified as an $\alpha$-region according to the Hale classification (Hale *et al.* 1919) and as an Hsx-region according to the McIntosh classification (McIntosh 1990). The leading positive-polarity sunspot was almost completely encircled by a penumbra and was followed by two small pores of positive polarity. By the next day, the active region had grown in size, with the trailing negative-polarity sunspot forming a penumbra and new pores appearing in the leading part. The typical separation of opposite polarities, as seen in regions with new flux emergence, was present, with a clockwise rotation of the trailing sunspot.

On September 8, the continuous flux emergence between the two polarities of the active region led to its classification as a $\beta$- and Dso-region. Visual inspection of HMI and HiFI+ time series (see animations of Figures 3.1 and 3.2) already revealed that the leading positive-polarity sunspot was surrounded by the moat flow (Vargas Domínguez *et al.* 2008), which became more pronounced once the sunspot moved into the center of a supergranule at about 10:00 UT. The two smaller sunspots of leading polarity showed signs of the moat flow only where the rudimentary penumbra had formed. The trailing sunspot also appeared to be located in the center of a supergranule a day later, which was accompanied by an increase in moat flow. A C-class flare occurring in an adjacent active region at 17:00 – 18:00 UT coincided with a subsequent simplification of the magnetic configuration, that is, mixed polarities separated and a negative-polarity patch to the east of the leading sunspots started to decay.

By September 9, active region NOAA 13096 reached its maximum size, with 130 millionths of a solar hemisphere. The leading polarity had gained two more sunspots with rudimentary penumbra at about 02:00 UT. Throughout its entire evolution, from its appearance on the limb until the beginning of the high-resolution observations, no penumbra formed in the region between the leading sunspots of the same polarity facing each other (see Künzel 1969). The two polarities of the region continued to separate, leading to the formation of more pores of negative polarity. High-resolution GREGOR observations on September 9 followed the evolution of the region. By September 10, the region was classified as a Dai-region. On the following day, the leading-polarity sunspots had disappeared, leaving only a trailing sunspot with a partial penumbra. Pores in the trailing region persisted until September 12. By September 16, just before the region rotated off the disk, only patches of opposite polarity were still visible in magnetograms, with no evidence of dark features or pores in the continuum.

#### Photospheric Evolution

For a more structured discussion of the leading part of active region NOAA 13096, the high-resolution GREGOR observations on September 9 are divided into three smaller regions-of-interest (ROIs) highlighted in the middle-left panel of Figure 3.2. The overall appearance of the high-resolution photospheric observations (that is, G-band, blue continuum, H$\alpha$ broad-band, and TiO images) is quite similar. All dark umbrae show umbral dots, and the FOV is covered by small-scale bright points, as seen in all photospheric channels except the blue continuum channel. The umbral dots and bright points are more pronounced in TiO images, where bright points are seen extending from sunspot No. 3 towards the trailing negative polarity region, which is not covered by the FOV. In addition, the dynamics and variability in the FOV are also well captured by the H$\alpha$ broad-band channel, despite the lower contrast compared to the other photospheric channels.

The leading sunspot No. 1 is surrounded by a penumbra, except for the inner part facing sunspots No. 2 and 3. In the region between the three sunspots, none of them formed a penumbra at any time. In addition, two pores are located in the vicinity of sunspot No. 1, one in the north at coordinates (40″,

24″) and the other at (38″, 20″), separated from the sunspot by a light bridge. During the GREGOR observations, the penumbra remained stable and no major changes were observed.

Sunspot No. 2 at coordinates (12″, 20″) has a rudimentary penumbra, which formed along the eastern edge of the sunspot, limited to a segment of about 4″. The sunspot is separated from its neighboring pore at coordinates (14″, 17″) by a light bridge and has two dark knots below at coordinates (10″, 11″) and (6″, 14″), which remained stable during the GREGOR observations.

Sunspot No. 3 also developed only a rudimentary penumbra at the eastern edge of the sunspot. The sunspot umbra split up at 8:13 UT and formed a light bridge at coordinates (24″, 36″). Besides the formation of a light bridge, this ROI appears in a stable configuration and small features remain visible during GREGOR observations, that is, two tiny pores at coordinates (30″, 38″) and (34″, 38″).

#### Chromospheric Evolution

In the chromospheric broad-band Ca II H images, the typical photospheric granulation pattern is still visible. The FOV includes sunspot No. 3 and partially sunspot No. 2. The intergranular lanes appear mostly bright in regions directly associated with flux emergence (bottom-left quadrant of the FOV) or in the regions between the two sunspots (bottom-right quadrant of the FOV). The overall size and shape of the observed features in the lower chromosphere are consistent with the photospheric morphology, including a light bridge that is clearly visible in the umbra of sunspot No. 3. During the observations, the penumbral filaments of sunspot No. 3 became longer. The dark lane in the light bridge of sunspot No. 2, which is partially obscured, is also visible.

In narrow-band H$\alpha$ observations (see the bottom-left panel of Figure 3.2), the scene appears drastically different compared to the lower atmospheric layers. The sunspot umbrae, indicated by red contour lines, are barely visible. An intensity threshold of $0.7\,I_0$ for the TiO intensity was chosen for the umbral contours. The FOV is dominated by filamentary structures. Most prominent is the bright triangular central region between the three positive-polarity sunspots, that is, the spongy region between sunspots No. 1, 2, and 3 and a small bright region at coordinates (4″, 36″). The leading sunspot No. 1 is almost completely surrounded by radial superpenumbral filaments, which are not fully formed around the sunspots No. 2 and 3. In addition, a dark persistent filament is present in the region between sunspot No. 2 and 3, extending to the trailing negative-polarity sunspot. This dark filament constantly interacts with the small bright region mentioned above. To the south and west, where a more finely structured pattern was observed, elongated filaments are present, which are absent in the southeast. Similar to sunspots No. 1 and 2, the sunspot No. 3 never developed a filamentary structure towards the central region between the three sunspots. Chromospheric filaments extend to the east and north of the sunspot No. 3 at the location of the rudimentary penumbra. However, the filaments in this direction are cut off by the small bright region mentioned above. Despite the highly dynamic fine structure within the FOV, the overall position and shape of the dark cores, filamentary structure, and bright regions remain the same during the chromospheric high-resolution observations.

### 3.3.2 Background-subtracted Solar Activity Maps

The BaSAM results for the HiFI+ data $\langle |I - \langle I \rangle| \rangle$ are shown in Figure 3.4, using the same layout as in Figure 3.2. The angle brackets $\langle \ldots \rangle$ indicate a time-series average, and $I$ refers to the intensity. The color scale from red to blue highlights regions of large and small variations, respectively. The individual maps show the combined results of the first and second time-series in a single map covering an ROI of $50'' \times 60''$, except for the top-left panel, where the Ca II H BaSAM is shown with an ROI of $25'' \times 30''$. Larger BaSAM values shown in red indicate stronger variations at that locations, while blue colors point to quieter regions.

#### Photosphere

The overall appearance of the photospheric BaSAMs is similar in all four photospheric channels: blue continuum, G-band, broad-band H$\alpha$, and TiO (Figure 3.4). The quietest regions are the umbral cores of the three sunspots as well as their neighboring pores, except for the broad-band H$\alpha$ BaSAM. The granulation

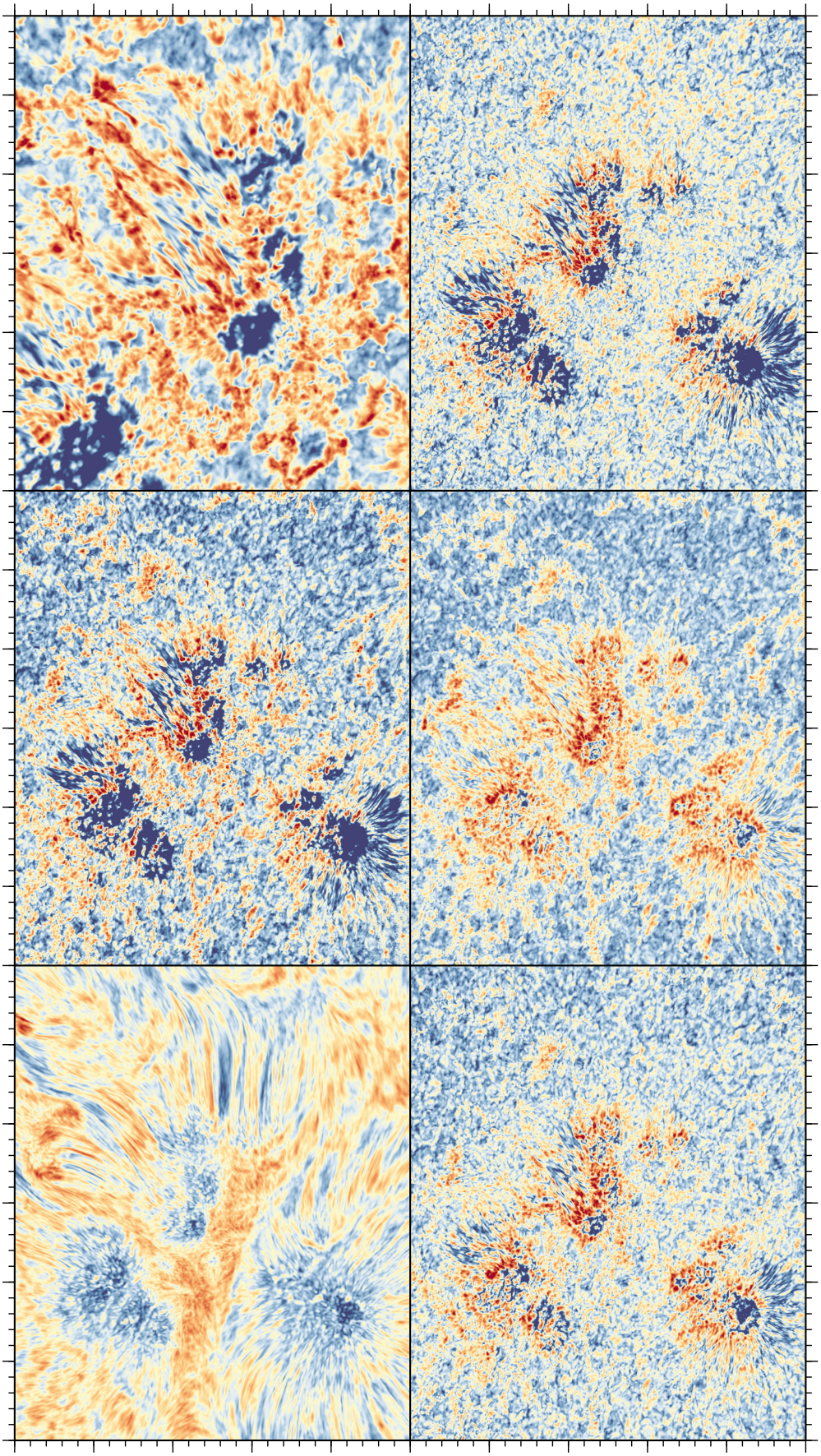

**Figure 3.4** Combined BaSAMs based on the first and second time-series (07:44 – 08:24 UT and 08:35 – 09:14 UT) of speckle-restored HiFI+ images: Ca II H (*top-left*), G-band (*top-right*), blue continuum (*middle-left*), broad-band H$\alpha$ (*middle-right*), narrow-band H$\alpha$ (*bottom-left*), and TiO (*bottom-right*). A common ROI of $50'' \times 60''$ (major tick marks are separated by $10''$) was extracted from the full FOV, except for the Ca II H image, where the ROI covers only $25'' \times 30''$.

pattern is visible in all four photospheric channels and shows low to medium BaSAM values, with the strongest variations occurring at the umbral borders. While the umbral regions in the TiO and broad-band H$\alpha$ BaSAMs are still the locations of the lowest values detected within the FOV, their patchy red and blue patterns make them appear more dynamic compared to the remaining photospheric observations.

The low signal within the penumbra on the western side of sunspot No. 1 indicates only small variations and therefore a stable configuration of the penumbra. The umbra of sunspot No. 1 does not contain many umbral dots or other features that could cause a signal in the photospheric BaSAMs. Only at the southern border of the sunspot No. 1, does the penumbra show a mixed pattern of high and low signals. In addition, large variations are associated with the neighboring pore at coordinates (35″, 20″), the light bridge separating the sunspot from the pore, and the small pore in the north at coordinates (40″, 24″).

The umbral borders of sunspot No. 2 and its neighboring pores are also locations of strong signals, while the rudimentary penumbra shows a mixed pattern of high and low signals. With increasing distance from the penumbra-umbra interface, parts of the rudimentary penumbra exhibit some of the lowest BaSAM values in the entire FOV. This is particularly evident in the G-band and blue continuum BaSAMs, where parts of the rudimentary penumbra are prominently displayed in dark blue color, while small patches associated with variations within the umbra are much more abundant and prominent in the broad-band H$\alpha$ and TiO BaSAMs. Strong variations were also detected at the location of the light bridge, especially near two small pores where the chevron-like light bridge begins on the eastern side of the sunspot.

The BaSAMs show that sunspot No. 3 contains the strongest variations in the FOV. In particular, the umbra-penumbra interface and parts of the penumbra are highlighted in dark red. However, the rudimentary penumbra also contains quieter areas in the middle of the penumbral filaments, which are highlighted in blue. In addition, the northern part of the umbra shows a very strong signal, indicating a highly dynamic interface with the penumbra at this location.

#### Chromosphere

The chromospheric Ca II H BaSAMs are very similar to the photospheric BaSAMs, with stronger signals mainly due to the higher contrasts of the small-scale brightenings, which are in most cases co-spatial in chromospheric and photospheric images (see Figure 3.2). The umbrae of sunspots No. 2 and 3 are clearly visible due to the very small variations. However, the umbral borders are characterized by strong BaSAM signals, indicating a very dynamic interface with the rudimentary penumbrae. In addition, the entire FOV of the zoomed-in Ca II H observations shows a mixed pattern of low, medium, and high signals, with strong variations appearing as filamentary extensions of the penumbral filaments. Alternating patterns of strong and weak signals characterize the rudimentary penumbrae of sunspots No. 2 and 3, especially at the penumbra-granulation interface.

Due to the drastic morphological differences observed in narrow-band H$\alpha$ observations, the corresponding BaSAMs give a very different picture of the chromospheric activity. The FOV is dominated by elongated filamentary structures with strong variations. The umbrae are clearly visible in all three ROIs due to very low BaSAM values. In addition, the broad and elongated filament at coordinates (26″, 46″) is a persistent feature during the GREGOR observations. A second low signal filamentary structure extends from sunspot No. 3 towards the trailing negative-polarity region. The southeast corner of the FOV contains a highly dynamic, fine-grained region, where elongated filaments are absent. The central region in between the three sunspots is characterized by a very strong signal and variations on small spatial scales. However, the regions with the strongest signals are located at coordinates (4″, 36″) and (1″, 53″) at the periphery of the FOV near the footpoints of filaments. The superpenumbra associated with the rudimentary penumbrae of sunspots No. 2 and 3 causes a mixed pattern of high and low BaSAM signals. In contrast, the extended superpenumbra of sunspot No. 1 is characterized by lower BaSAM signals, indicating a more stable configuration.

### 3.3.3 Local Correlation Tracking

Horizontal proper motions were determined using LCT (November and Simon 1988; Verma and Denker 2011) for time-series of of TiO, Ca II H, and narrow-band H$\alpha$ images. Local cross-correlations were computed for images separated in time by 36 s. Only persistent flows were measured by averaging

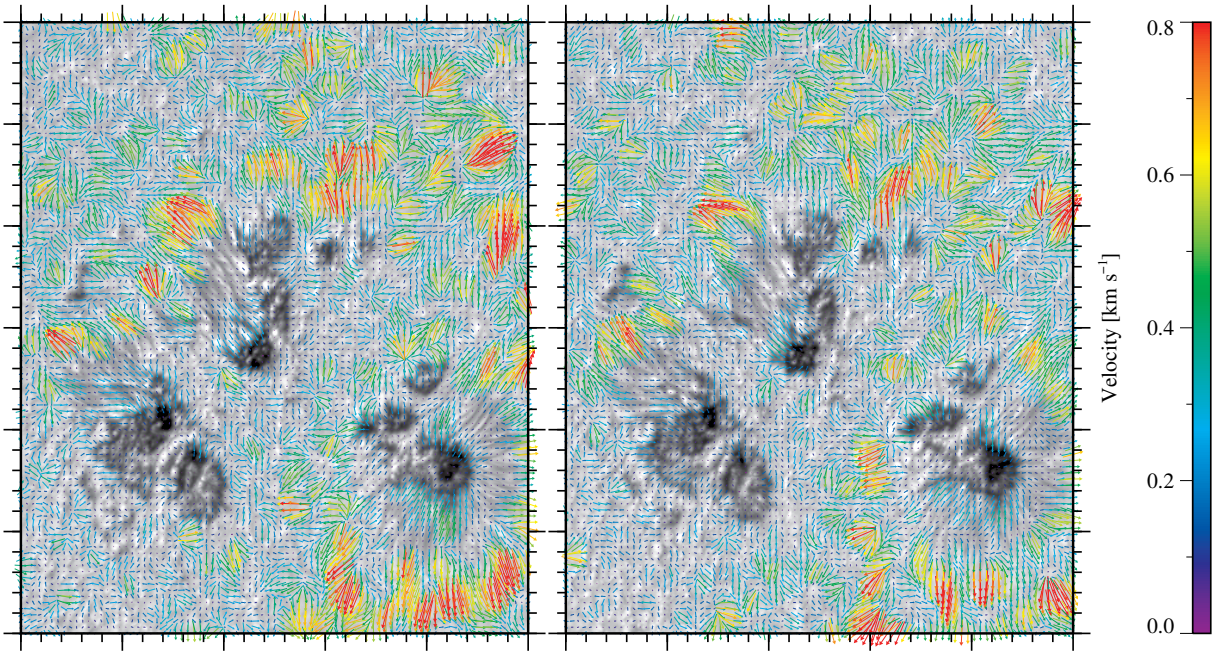


**Figure 3.5** Two-dimensional flow maps based on TiO first (*left*) and second (*right*) time-series. The ROI covers $50'' \times 60''$, and major tick marks are separated by $10''$. Flow speeds are displayed in the range $0.0-0.8$ km s$^{-1}$.

the individual flow maps over the duration of the time-series of approximately 40 min. Color-coded flow vectors are superimposed on the averaged image to indicate flow speed and direction. Since cross-correlations track contrast features in the sampling window, equating horizontal proper motions with plasma velocities has to be interpreted with caution. In the following, three flow maps are shown side by side for the first and second time-series, tracing the flow fields from the photosphere to the chromosphere.

### Photosphere

The LCT results based on photospheric observations are very similar. Therefore, only the TiO LCT maps are shown in Figure 3.5. The FOV covers $50'' \times 60''$ with average flow speeds displayed in the range of $0.0-0.8$ km s$^{-1}$. The flow vectors are superimposed on the averaged TiO images for the corresponding time-series. In general, the horizontal proper motions detected in the first time-series are also recovered in the second time-series. However, the flow pattern appears more fragmented at lower flow speeds. The moat flow is present at every location with a (rudimentary) penumbra. Even some locations without penumbra show signs of moat flow, for example, the two small pores to the west of sunspot No. 3 or the region on the eastern side of sunspot No. 1. Divergence centers caused by granulation are present around the sunspots. However, strong divergence centers, which are typical of exploding/expanding granules in opposite-polarity regions (Bonet *et al.* 2005), are absent. Patternless divergence centers with increased flow speeds are present in the northwest corner of the FOV. In contrast, the divergence centers in the southeast corner of the FOV are inconspicuous and have much lower flow speeds. The central region between the three sunspots is devoid of any well-ordered motions or divergence centers, and only low flow speeds are detected. The animated version of Figure 3.2 can be used to visualize the persistent flows captured in the LCT maps of Figure 3.5.

More quantitative results of the flow speeds are summarized in Table 3.2 for the umbra, the border of the umbra, the penumbra, and the moat flow regions. The regions for which the flow speeds are computed are outlined in the bottom-right panel of Figure 3.2. In addition to the total flow field, the radial flows were computed, with respect to the center of the umbral cores. The mean values of the flow speed are given with the standard deviation, which reflects the variation of the flow speeds in the selected regions and should not be taken as a formal error estimate.

The most prominent flow is the moat flow around sunspot No. 1, which just starts outside the penumbra. The averaged velocity maps show a radial outflow with velocities of $(-0.36 \pm 0.27)$ km s$^{-1}$. The moat flow is absent in the central region between the three sunspots. The Evershed flow in the penumbra

| | No. | Total flow field | Radial flows |
|---|---|---|---|
| Umbra | 1 | (0.18 ± 0.10) km s$^{-1}$ | (0.16 ± 0.10) km s$^{-1}$ |
| | 2 | (0.14 ± 0.06) km s$^{-1}$ | (0.10 ± 0.07) km s$^{-1}$ |
| | 3 | (0.14 ± 0.09) km s$^{-1}$ | (0.09 ± 0.08) km s$^{-1}$ |
| Umbral border | 1 | (0.19 ± 0.11) km s$^{-1}$ | (0.17 ± 0.12) km s$^{-1}$ |
| | 2 | (0.14 ± 0.08) km s$^{-1}$ | (0.08 ± 0.10) km s$^{-1}$ |
| | 3 | (0.17 ± 0.10) km s$^{-1}$ | (0.06 ± 0.11) km s$^{-1}$ |
| Penumbra | 1 | (0.23 ± 0.15) km s$^{-1}$ | (−0.06 ± 0.25) km s$^{-1}$ |
| | 2 | (0.20 ± 0.15) km s$^{-1}$ | (−0.06 ± 0.22) km s$^{-1}$ |
| | 3 | (0.16 ± 0.13) km s$^{-1}$ | (−0.03 ± 0.19) km s$^{-1}$ |
| Moat | 1 | (0.43 ± 0.23) km s$^{-1}$ | (−0.36 ± 0.27) km s$^{-1}$ |
| | 2 | (0.32 ± 0.20) km s$^{-1}$ | (−0.22 ± 0.26) km s$^{-1}$ |
| | 3 | (0.38 ± 0.22) km s$^{-1}$ | (−0.27 ± 0.26) km s$^{-1}$ |

**Table 3.2** Averaged horizontal proper motions of the umbra, umbral border, penumbra, and moat region for the three ROIs. Mean and standard deviation of the LCT results are based on the combined TiO observations of the first and second time-series. Details on the LCT setup are given at the end of Section 3.2.2.

of sunspot No. 1 has an average outflow speed of (−0.06 ± 0.25) km s$^{-1}$. Low inflow speeds of (0.17 ± 0.12) km s$^{-1}$ are measured at the umbra-penumbra interface, which continue into the umbra with speeds (0.16 ± 0.10) km s$^{-1}$. The light bridge is devoid of strong horizontal motions and no signs of convective upwelling were found in its center. The location, where the light bridge connects to the plasma surrounding the sunspot, shows small inward motions that are not detected in the second time-series. Both pores near sunspot No. 1 are characterized by inflows at the umbra-granulation interface.

Strong horizontal proper motions are detected only in the moat region of sunspot No. 2, which are restricted to a narrow region at coordinates (5″, 28″), where the average outflow speed is (−0.22 ± 0.26) km s$^{-1}$. Otherwise, only small outflows of (−0.06 ± 0.22) km s$^{-1}$ are measured in the penumbra, while inflows of (0.08 ± 0.10) km s$^{-1}$ and (0.10 ± 0.07) km s$^{-1}$ are determined at the border of the umbra and inside the umbra, respectively. The light bridge shows no signs of directed plasma motions, which excludes convective upwelling in the center of the light bridge. The small pore above the rudimentary penumbra of sunspot No. 2 at coordinates (6″, 34″) shows moderate inflows that become stronger during the second time-series.

Average outflows of (−0.27 ± 0.26) km s$^{-1}$) and (−0.03 ± 0.19) km s$^{-1}$) were measured for the moat flow and Evershed flow of sunspot No. 3, respectively. Average inflows of (0.06 ± 0.11) km s$^{-1}$) and (0.09 ± 0.08) km s$^{-1}$) were determined at the border of the umbra and within the umbra, respectively. The large horizontal proper motions north of the umbra of sunspot No. 1 and the neighboring two pores decreased during the second time-series.

### Chromosphere

The results of applying LCT to the chromospheric Ca II H observations are shown in Figure 3.6. In general, the Ca II H flow maps are similar to the photospheric flow maps, with divergence centers caused by granulation and significant inflows and outflows associated with sunspots. In contrast to the generally decreasing photospheric flow speeds during the second time-series, the chromospheric Ca II H flow maps give the impression of increased flows.

Due to the limited FOV of the Ca II H observations, only the flows at the northern and western border of the sunspot No. 2 can be studied. The light bridge is devoid of strong horizontal proper motions and outflows along the light bridge are missing. In agreement with photospheric flow maps, the strongest motions of sunspot No. 2 are located at the outer ends of the filaments in the rudimentary penumbra at coordinates (4″, 25″). The average flow speed decreases at this location in the second time-series. The flow speeds are moderate in the region between the sunspots No. 2 and 3 and decreased significantly during the second time-series.

The inflows at the border of the umbra of sunspot No. 3 are enhanced at the location where the rudimentary penumbra has formed and appear slightly increased in the second time-series. The moat flow begins at the periphery of the rudimentary penumbra, and even single, isolated penumbral filaments show evidence of moat flow at their tips. In particular, strong outflows in excess of 0.5 km s$^{-1}$ are associated with the small pore at coordinates (23″, 21″), which intensify and become more confined in the second time-series.

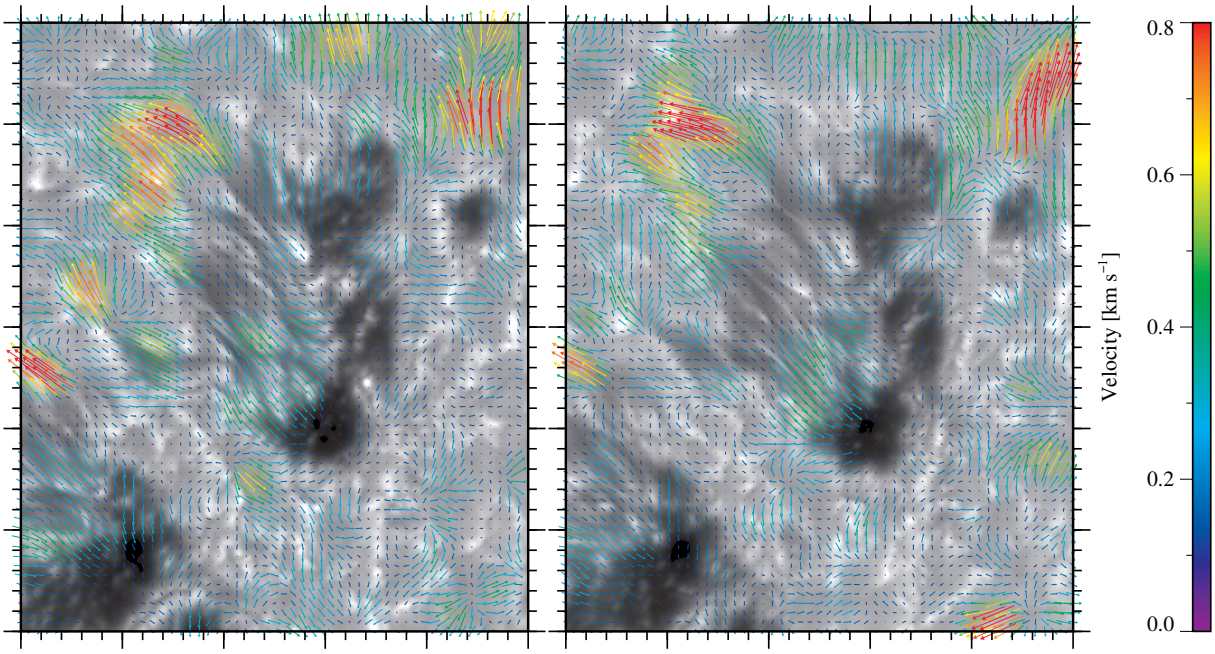


**Figure 3.6** Two-dimensional flow maps based on the first (*left*) and second (*right*) Ca II H time-series. The ROI covers $25'' \times 30''$, and major tick marks are separated by $5''$. Flow speeds are displayed in the range $0.0 - 0.8$ km s$^{-1}$

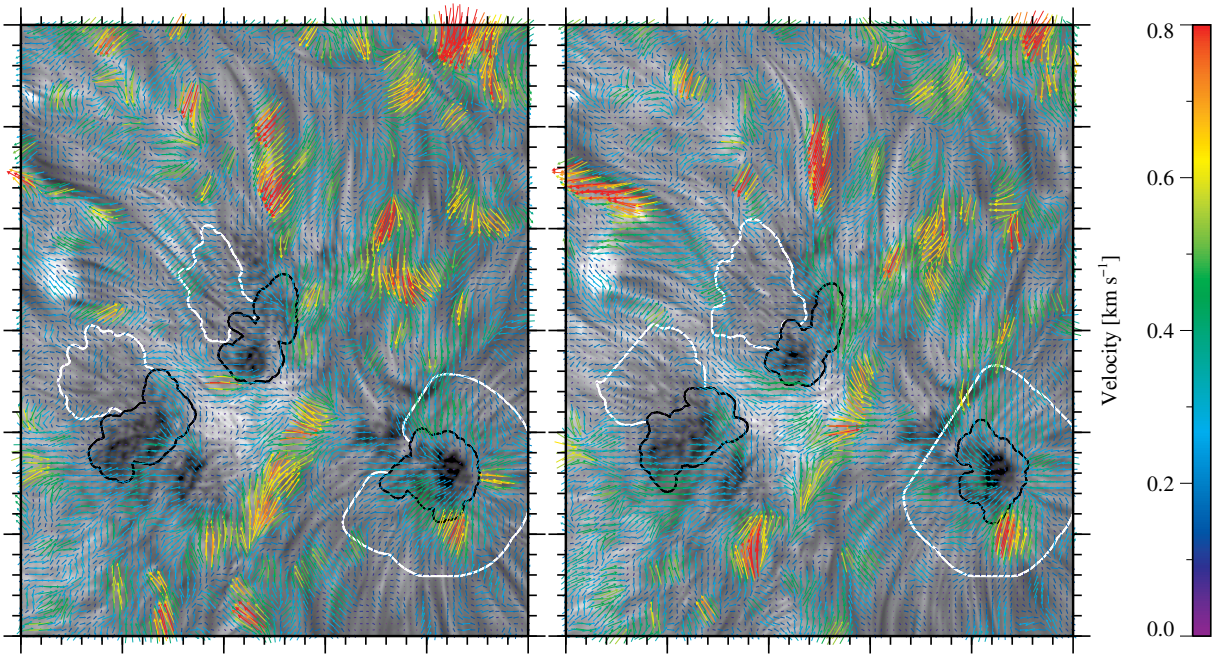


**Figure 3.7** Two-dimensional flow maps based on the first (*left*) and second (*right*) narrow-band H$\alpha$ time-series. The ROI covers $50'' \times 60''$, and major tick marks are separated by $10''$. Flow speeds are displayed in the range $0.0 - 0.8$ km s$^{-1}$. The black contours that outline the umbrae are based on the TiO image, where an intensity threshold of $0.7\,I/I_0$ of the normalized quiet-Sun intensity was used, and the white contours outline the penumbrae.

The appearance of the chromospheric narrow-band H$\alpha$ flow maps in Figure 3.7 differs significantly from the photospheric flow maps. Strong flows enter the FOV at coordinates ($43''$, $60''$), where they meet oppositely directed flows with moderate flow speeds at coordinates ($37''$, $54''$). Inflows surround the sunspot No. 1. The bright filament above the sunspot No. 3 at coordinates ($24''$, $47''$) shows strong and confined inflows that become even more confined in the second time-series. A strong eastward motion coincides with the bright patch at coordinates ($4''$, $36''$) and the associated dark filament at coordinates ($5''$, $44''$), where the flows increase significantly in the second time-series, especially along the dark filament. The bright central region between the three sunspots at coordinates ($22''$, $22''$) is characterized by low to moderate flow speeds, forming a front with flow vectors directed towards the sunspot No. 1.

| | No. | Total flow field | Radial flows |
|---|---|---|---|
| Umbra | 1 | $(0.26 \pm 0.11)$ km s$^{-1}$ | $(0.20 \pm 0.13)$ km s$^{-1}$ |
| | 2 | $(0.20 \pm 0.10)$ km s$^{-1}$ | $(0.03 \pm 0.12)$ km s$^{-1}$ |
| | 3 | $(0.23 \pm 0.10)$ km s$^{-1}$ | $(0.07 \pm 0.14)$ km s$^{-1}$ |
| Umbra border | 1 | $(0.33 \pm 0.15)$ km s$^{-1}$ | $(0.30 \pm 0.14)$ km s$^{-1}$ |
| | 2 | $(0.20 \pm 0.11)$ km s$^{-1}$ | $(0.03 \pm 0.12)$ km s$^{-1}$ |
| | 3 | $(0.27 \pm 0.14)$ km s$^{-1}$ | $(0.10 \pm 0.16)$ km s$^{-1}$ |
| Penumbra | 1 | $(0.28 \pm 0.13)$ km s$^{-1}$ | $(0.23 \pm 0.14)$ km s$^{-1}$ |
| | 2 | $(0.11 \pm 0.06)$ km s$^{-1}$ | $(-0.02 \pm 0.08)$ km s$^{-1}$ |
| | 3 | $(0.16 \pm 0.09)$ km s$^{-1}$ | $(-0.02 \pm 0.08)$ km s$^{-1}$ |
| Moat | 1 | $(0.18 \pm 0.11)$ km s$^{-1}$ | $(-0.03 \pm 0.11)$ km s$^{-1}$ |
| | 2 | $(0.18 \pm 0.10)$ km s$^{-1}$ | $(0.07 \pm 0.15)$ km s$^{-1}$ |
| | 3 | $(0.21 \pm 0.09)$ km s$^{-1}$ | $(-0.11 \pm 0.15)$ km s$^{-1}$ |

**Table 3.3** Averaged horizontal proper motions of the umbra, umbral border, penumbra, and moat region for the three ROIs. Mean and standard deviation of the LCT results are based on the combined narrow-band H$\alpha$ observations of the first and second time-series. Details on the LCT setup are given at the end of Section 3.2.2.

The superpenumbra that partially surrounds the sunspot No. 1 shows an inward motion, which is characteristic of the inverse Evershed flow (Moore and Rabin 1985). These flows are significantly larger in a small region at coordinates (44″, 10″). In general, the flows associated with the superpenumbra of this sunspot are the same in both time-series. The rudimentary penumbra of the sunspot No. 2 shows no signs of the inverse Evershed flow. Overall, the horizontal proper motions within this ROI are small, with stronger inflows at the location of the light bridge and the umbral core at coordinates (16″, 16″), with inflows becoming stronger in the second time-series. The flow pattern associated with the sunspot No. 3 shows much variation between the two time-series. The inverse Evershed flow is observed only in the northern part of the sunspot, mainly in locations with filamentary structure. In the southern part of the sunspot, the velocity vectors form streamlines around the umbra.

The chromospheric flow velocities corresponding to the photospheric ROIs outlined in the bottom-right panel of Figure 3.2 are summarized in Table 3.3. The velocities determined in the chromosphere are generally of lower magnitude than their photospheric counterparts. In particular, the radial flows in the direction of the center of the sunspots, indicated by the orange crosses in Figure 3.2, differ significantly in the moat flow region, with photospheric velocities exceeding those of the chromosphere. In contrast to the photospheric flows, the penumbral region of sunspot No. 1 and the moat region of sunspot No. 2 show an outward motion at chromospheric heights with very low velocities.

### 3.3.4 Magnetic Fields

Magnetic fields and the sensitivity of certain spectral lines to them provides access to different atmospheric and magnetic field parameters using inversion codes. In the following, the GRIS observations are studied with an emphasis on plasma temperatures and the orientation and strength of the photospheric magnetic field using the SIR inversion code.

The SIR code was used to derive the six physical parameters in Figure 3.8 for the Si I line. The slit-reconstructed continuum intensity image is very similar to the TiO observations discussed in Section 3.3.1 but the contrasts of the umbral dots and of the light bridges are reduced, giving the visual impression that the umbral cores are more densely filled by these features. The light bridges have predominantly umbral temperatures, with the exception of sunspot No. 1, where the temperatures of the light bridges are higher and reach quiet-Sun temperatures. The highest temperatures are found in the rudimentary penumbrae of sunspots No. 2 and 3, which even show small kernels of localized heating. The three sunspots are clearly separated in the map of the vertical component of the magnetic field strength $B_z$. An almost field-free region divides sunspots No. 2 and 3 from sunspot No. 1. This separation of the flux systems is repeated successively on the hierarchical level of the umbral cores, where light bridges serve as separators.

A patch of negative polarity region is present on the left side of sunspots No. 2 and 3, as also seen in the SDO magnetograms. Small-scale positive and negative polarity features are scattered around sunspot No. 1, which are the typical type II and III moving magnetic features (MMF, Harvey and Harvey 1973; Hagenaar and Shine 2005), respectively. The strongest horizontal component of the magnetic field strength $B_{\rm hor}$ is found around sunspots No. 2 and 3 in the region associated with the rudimentary penumbral filaments. In the region between sunspots No. 1, 2, and 3 $B_{\rm hor}$ is much stronger than $B_z$. The

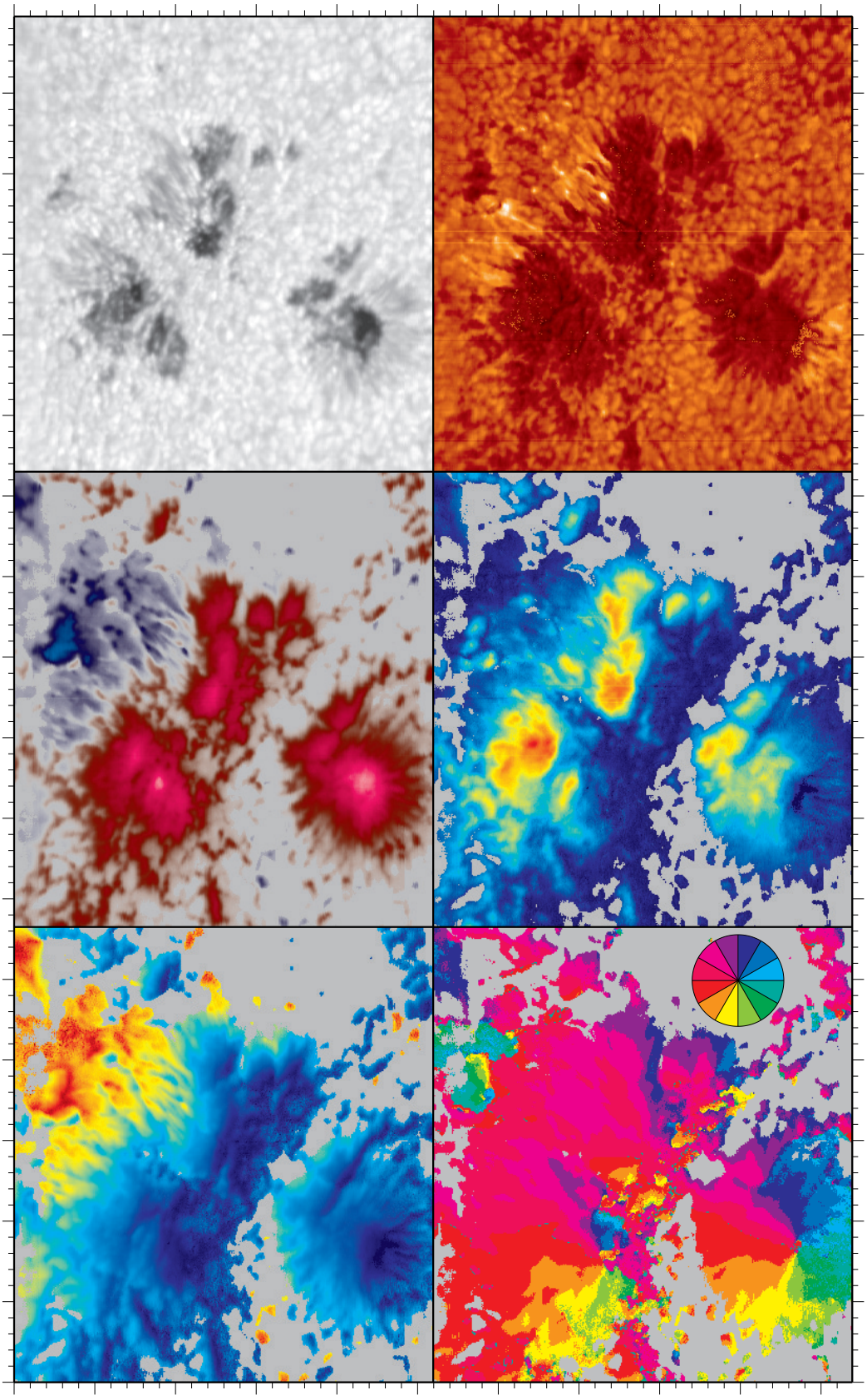

**Figure 3.8** Maps of six physical parameters derived for the Si I line (*from top-left to bottom right*): continuum intensity in the range of (0.5 – 1.1) $I_0$, temperature in the range of 5500 K – 6000 K, vertical magnetic field strength $B_z$ in the range of ±2000 G (blue/red corresponds to negative/positive magnetic fields), horizontal magnetic field strength $B_{\rm hor}$ in the range of 0 G – 1800 G (rainbow color table), inclination in the range of 0° – 180° (rainbow color table), and azimuth in the range of 0° – 360° (color wheel in the upper-right corner indicates the direction of the magnetic fields). Regions with a degree of polarization below 0.2% are displayed in gray. The FOV is 52.0″ × 56.6″, and major tick marks are separated by 10″.

field inclination is mostly vertical in the sunspots with a gradual decrease when going from the dark umbral core to the penumbra-granulation border. The negative polarity region shows the presence of inclined field lines. The orientation of the field lines can be followed in the azimuth map. However, only for sunspot No. 1 do the field lines follow the full compass rose.

## 3.4 Discussion

This case study addresses the dynamic interplay of magnetic fields and plasma flows associated with three positive-polarity sunspots with rudimentary penumbrae and light bridges in active region NOAA 13096. The high-resolution observations are interpreted in the context of active-region decay in the following days. The decay process was atypical, since the observed leading polarity was less compact and fragmented earlier than the single sunspot in the trailing part of the active region.

The penumbra formation begins in the leading part, followed by the trailing sunspot. The three positive-polarity sunspots show no signs of rotation, while the trailing negative-polarity sunspot rotated clockwise (Howard 1990; D'Silva and Howard 1994; Kutsenko, Abramenko, and Litvishko 2023) until a southward drift began. A magnetic flux concentration in a small, unnumbered active region to the south of the observed active region produced a C-class flare on 2022 September 8, which coincided with a subsequent simplification of the magnetic configuration of active region NOAA 13096. However, the system remained globally stable but with many small-scale changes. The region between the leading and trailing sunspots was devoid of exploding or expanding granules as often found in bipolar regions with flux emergence (Bonet *et al.* 2005; Kamlah *et al.* 2023).

Penumbra formation is still an elusive topic and depends strongly on the topology of the active region and the structure of the local plasma flows. At the beginning of the GREGOR observations, only one of the three leading sunspots had a penumbra while the other two had rudimentary penumbrae (Watanabe, Kitai, and Otsuji 2014). However, a penumbra never formed in the central region, where sunspots of the same polarity face each other (Künzel 1969; Murabito *et al.* 2021). Several studies (Shimizu, Ichimoto, and Suematsu 2012; Romano *et al.* 2013, 2014; Murabito *et al.* 2016; Romano *et al.* 2020) have emphasized that inclined photospheric magnetic field lines can be formed by shifting chromospheric field lines with typical tilts of $40° - 80°$ down to the photosphere. However, this penumbra formation scenario requires a canopy to confine the chromospheric field lines. The mostly vertical fields in the central region between the three sunspots prevent such a canopy and consequently preclude penumbra formation in this region (Murabito *et al.* 2021; Lindner *et al.* 2023). Furthermore, the latter authors showed that the analysis of the magnetic topology in the deep photospheric layers alone is not a reliable indicator for the presence of a penumbra, which is consistent with the missing horizontal magnetic field component of sunspot No. 1 (see the middle-right panel of Figure 3.8).

If the photospheric Evershed effect is driven by a siphon flow, magnetoconvection, or a mixture of both is still an ongoing debate, although recent observations favor magnetoconvection (Murabito *et al.* 2016). The three-dimensional topography of sunspots supports the theory of mass motion and wave propagation from the photosphere to the corona along field lines (Staude 1999; Solanki 2003; Khomenko and Collados 2015). The dominant drivers of mass motion are typically the Evershed and inverse Evershed flows in the photosphere and chromosphere, respectively, with the latter starting at a height of about 500 km (Boerner and Kneer 1992). The penumbrae of the three leading sunspots show the Evershed effect (Evershed 1909), which transports material from the umbra along penumbral filaments into the surroundings. The average LCT velocities determined are close to zero and thus significantly lower than the penumbral velocities determined in other studies (i.e., greater than 1.5 km $s^{-1}$, Molowny-Horas 1994; Verma *et al.* 2018b; Wang *et al.* 2018b; Márquez, Sánchez Almeida, and Bonet 2006) or found in simulations (i.e., $3 - 4$ km $s^{-1}$, Rempel 2015). The low penumbral flow speeds are interpreted as the imminent decay of the penumbrae. The variability detected in BaSAMs emphasizes the changes associated with inflows at the umbral borders. However, the penumbra of sunspot No. 1 and the rudimentary penumbrae of sunspots No. 2 and 3 show some of the strongest BaSAM signals during the observations, which becomes much weaker at the periphery of the rudimentary penumbrae. These patches of low flow speeds are located at the interface between the penumbra and the moat flow, which causes the signal to increase with distance. The chromospheric Ca II H observations show inflows at the border of the pore, which are comparable to

photospheric flows, and a divergence region in the middle of the rudimentary penumbra with inflows in the inner penumbra and outflows in the outer parts (Deng *et al.* 2007; Verma and Denker 2011).

In magnetograms the moat regions appear to be enhanced after the umbrae have moved to the center of the supergranules. The present flow maps show that the moat flow is closely associated with rudimentary and regular penumbrae. Several studies have determined horizontal velocities of the moat flow in the range of 0.5 km $s^{-1}$ – 1.0 km $s^{-1}$ (Muller and Mena 1987; Shine *et al.* 1996; Bonet *et al.* 2005; Sobotka and Roudier 2007), which is consistent with the present measurements in the range of 0.2 km $s^{-1}$ – 1.0 km $s^{-1}$. Moving magnetic features, transporting magnetic flux from the umbra to the supergranular cell boundaries, reach velocities up to 2 km $s^{-1}$ – 3 km $s^{-1}$ (Shine *et al.* 1996; Hagenaar and Shine 2005). These velocities are typically measured by applying feature tracking methods to small-scale magnetic features. In contrast, LCT follows contrast variations within a sampling window, which contains contributions from various features. These contrast changes are not always related to plasma motions, and even if a close relationship to plasma motions exists, LCT method can significantly underestimate plasma velocities (Verma, Steffen, and Denker 2013). Thus, the present results do not argue against higher flow speeds observed for moving magnetic features. Due to the late evolutionary stage of the sunspots, the flow speed within the moat significantly exceeds the outflows in the penumbra. The moat flow is visible in the flow maps up to about 4 Mm beyond the periphery of the penumbra, which is a much smaller value than previously reported (i.e., 10 Mm – 20 Mm, Sheeley 1972; Brickhouse and Labonte 1988) and contradicts the tendency of more mature sunspots to have more extended moat regions (Sobotka and Roudier 2007). However, Löhner-Böttcher and Schlichenmaier (2013) concluded that moat radii are independent of sunspot radii, which was further supported by Verma, Kummerow, and Denker (2018a). The present study supports the finding that moat and Evershed flows are firmly linked to the presence of a penumbra. Even the smallest patches of penumbra are accompanied by these outflows. In summary, the moat flow dissolves and disappears after the decay of the penumbra. However, spectropolarimetric observations with higher cadence are needed to study the cessation of the moat flow as a function of time, which is an interesting science case for high-resolution telescopes equipped with imaging spectropolarimeters.

All observed umbrae contain umbral dots, which are however less prominent in BaSAMs due to their shorter lifetimes of 15 min – 60 min and dimensions of 80 km – 400 km (Beckers and Schröter 1968; Koutchmy and Adjabshirzadeh 1981; Lites *et al.* 1991; Sobotka, Brandt, and Simon 1997; Denker 1998). Moreover, they are stable features, at least in the central part of the umbrae. The chromospheric Ca II H BaSAMs and LCT maps closely resemble those of the blue continuum observations. Strong variations within the umbrae are not detected, although some intrusions of bright points from the periphery, which only give weak signals. However, bright intergranular lanes in between the positive-polarity sunspots and extending out to the trailing part of NOAA 13096 are very prominent in the BaSAMs.

In the chromospheric narrow-band H$\alpha$ BaSAMs, the umbrae are clearly visible as regions with only small variations. However, the central T-shaped part in between the positive-polarity sunspots on the other hand stands out for its bright and spongy appearance, causing a strong signal in the BaSAMs and highlighting the strong variability on small spatial scales. This phenomenon is called "moss" in EUV images (Berger *et al.* 1999) and is caused by thermal conduction from coronal loops with temperatures of $(3-5) \times 10^6$ K situated above a plage. In fact, this location is associated with the footpoint region of a coronal loop. Berger *et al.* (1999) emphasized that the spongy appearance is caused by chromospheric jets (Wang *et al.* 1998; Mulay *et al.* 2016; Iijima and Yokoyama 2017) and spicules (Moore *et al.* 1977; Tsiropoula *et al.* 2012) interspersed with EUV emission. The misalignment with the underlying magnetic elements can be confirmed in the present study. Despite the apparent increase in activity, the superpenumbral flows in this region are low, if present at all.

While the leading sunspot No. 1 is almost completely surrounded by superpenumbra, the other two leading sunspots developed only rudimentary superpenumbral structures at the locations where also rudimentary penumbra had formed in the photosphere. The BaSAMs indicate a rather stable configuration of the superpenumbra around sunspot No. 1 by its alternating red and blue filamentary structure. In addition, LCT flow maps show an inward motion for sunspot No. 1, which is not aligned with the superpenumbral filaments. The dark filaments, seen as elongated dark blue structures in BaSAMs, extending from sunspot No. 3 to the trailing negative-polarity sunspot, appear in a stable configuration, while inhibiting major horizontal proper motion.

## 3.5 Conclusions

The combination of ground-based high-resolution observations of different spectral regions and thus different atmospheric heights with synoptic SDO full-disk data made a comprehensive analysis of the active region NOAA 13096 possible, scrutinizing the photospheric Evershed flow and the chromospheric inverse Evershed flow. The fragmentation of the leading sunspots before the trailing sunspot is a rather atypical behavior for active region evolution. The decay process was studied in terms of plasma flows and connectivity to the surroundings using LCT and BaSAMs.

The imminent decay of the active region is characterized by the relatively low Evershed flows. Only one of the leading positive-polarity sunspots has a superpenumbra, while rudimentary superpenumbrae formed only at the locations where photospheric rudimentary penumbrae already existed, which were facing the trailing negative-polarity sunspot. Exploding or expanding granules, which are typically present in the center of bipolar regions, are not observed. Light bridges, present in all three leading sunspots, do not cause a temperature increase. However, they appear as field-free regions in horizontal and vertical magnetic field maps. In addition, no convective outflows were found along the light bridges. In chromospheric narrow-band H$\alpha$ observations, features associated with EUV moss were found in the form of a bright spongy region. This region was slightly displaced with respect to magnetic features in lower atmospheric layers, in agreement with previous descriptions of this phenomenon.

Further analysis of emerging and decaying active regions is needed to better understand the difference between regions with and without field-aligned flows. In particular, the transition from emergence to decay needs to be studied in more detail to clarify the role of light bridges in the decay process. How does the magnetic field weaken in these regions, which eventually become field-free? In addition, the influence of the low-lying magnetic canopy over light bridges and its relation to the umbral magnetic field and the plasma flows requires closer scrutiny. To get a coherent picture of the interplay between features caused by strong magnetic fields (i.e., sunspots and pores) and features related to them (i.e., light bridges and umbral dots), more case studies are required, combining different spatial and temporal scales and covering different atmospheric heights in multi-wavelength observations. As more and more high-resolution imaging and spectropolarimetric data become publicly accessible in archives of for example, the GREGOR solar telescope, Daniel K. Inouye Solar Telescope (DKIST), and the Swedish Solar Telescope (SST), targeted searches to answer some of the open questions on active-region evolution become possible.

# Chapter 4

# Wide-field Image Restoration of G-band and Ca II K Images Containing Large and Complex Active Regions

## 4.1 Introduction

Data from space missions such as the Solar Dynamics Observatory (SDO, Pesnell, Thompson, and Chamberlin 2012) now routinely provide full-disk images of the Sun's atmospheric layers, as well as measurements of magnetic and velocity fields across the solar disk, with a spatial resolution of about one arcsecond. Moving to much smaller spatial scales (down to 0.06″ or even 0.02″), facilities such as the 1.0-meter Swedish Solar Telescope (SST Scharmer *et al.* 2003), the 1.5-meter GREGOR solar telescope (Schmidt *et al.* 2012), the 1.7-meter Goode Solar Telescope (GST, Cao *et al.* 2010b), the 4-meter Daniel K. Inouye Solar Telescope (DKIST, Rimmele *et al.* 2020), and the future 4-meter European Solar Telescope (EST, Quintero Noda *et al.* 2022a) reach the dimensions of the photon mean free path and of fundamental magnetic structures in the solar atmosphere of just a few tens of kilometers. Bridging the diffraction-limited spatial scales of high-resolution and synoptic telescopes will require telescopes and instruments that explore the spatial domain between 0.1″ and 1.0″ with a field-of-view (FOV) that is sufficiently large to capture, for example, large active regions and extended chromospheric filaments.

The demonstration of the unique scientific capabilities of the Vacuum Tower Telescope (VTT, von der Lühe 1998) motivated this work. In particular, the telescope combines a large FOV, which is partially corrected by an adaptive optics (AO) system (Berkefeld *et al.* 2010), and an ultra-high-resolution ($\mathcal{R} \approx 1\,000\,000$) echelle spectrograph. This work focuses on the first aspect and demonstrates that AO correction and image restoration techniques can provide image quality, approaching the telescope's diffraction limit, over a circular FOV with a diameter of 270″. As a proof of concept, one of the high-cadence, large-format CMOS cameras of the Fast Multi-line Universal Spectrograph (FaMuLUS) camera system was used to observe G-band and Ca II K images of large and complex active regions. The goal is to verify that the camera system provides high-resolution data for measuring horizontal proper motions, identifying the locations of enhanced solar activity, enabling image restoration, and delivering data for seeing characterization.

## 4.2 Observations

The VTT is located at the Observatory del Teide, Izaña, Tenerife, Spain, where it has been in operation since the 1980s (Schröter, Soltau, and Wiehr 1985). The VTT has a coelostat system with two 80 cm mirrors installed on a platform at a height of 38 m, where the sunlight is directed into a vacuum tank with an aperture of 75 cm in diameter (see Figure 1 in von der Lühe *et al.* 2003). The primary mirror with a diameter of 70 cm is mounted in an off-axis configuration inside the vacuum tank. The secondary mirror focuses the light onto the entrance slit of the Echelle spectrograph. At this location the focal length of the telescope is 45.65 m, the plate scale is 4.49″ mm$^{-1}$, and the diameter of the FOV is 600″. Two folding

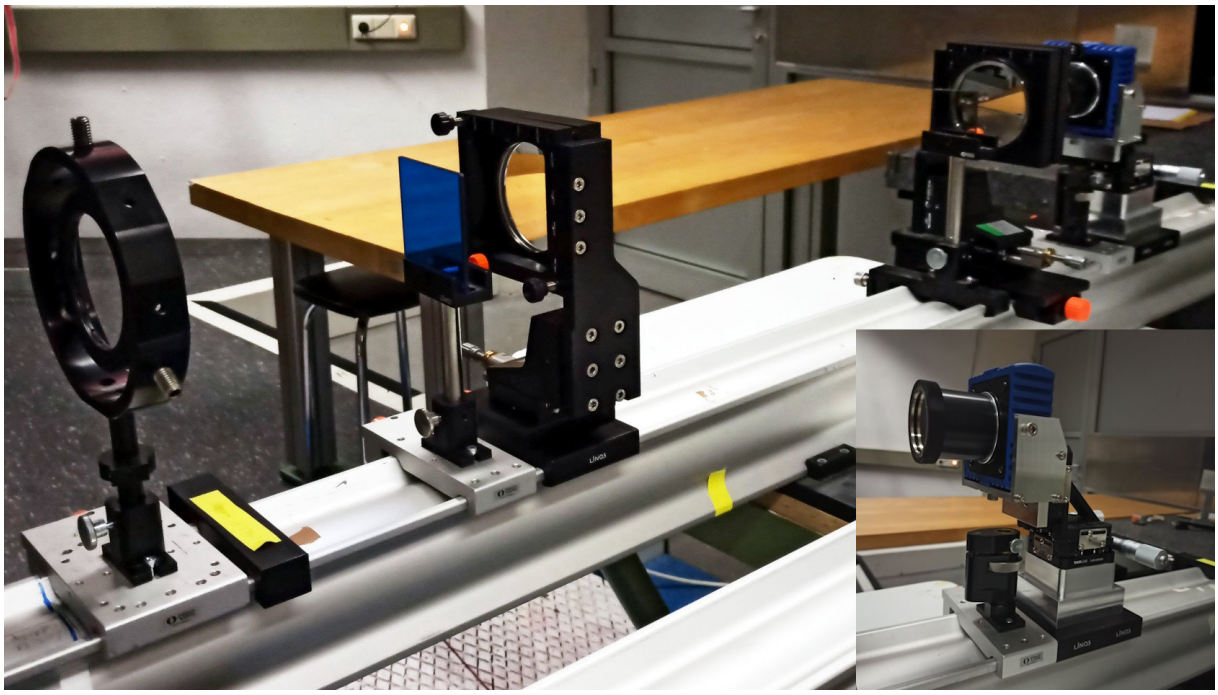

**Figure 4.1** Optical setup for wide-field imaging at the VTT: iris field stop, blue color filter, achromat ($f_1 = 310$ mm), neutral density filter, achromat ($f_2 = 160$ mm), and camera with interference filter (from left to right). The insert shows details of the camera mount and the interference filter holder.

mirrors can be inserted, so that the incoming light makes a U-turn through the Kiepenheuer Adaptive Optics System (KAOS, von der Lühe *et al.* 2003; Berkefeld *et al.* 2010), which preserves the plate scale but reduces the diameter of the FOV to about 270″. Another folding mirror on a rotary stage, just after the exit of the AO system, directs the light horizontally to optical laboratories or optical benches inside the tower. The latter were used for a compact imaging setup with a transfer optic with two achromats ($f_1 = 310$ mm and $f_2 = 160$ mm, see Figure 4.1) that increases the plate scale to 8.70″ mm$^{-1}$. A blue color filter and a neutral density filter reduced the light level so that overexposures can be avoided and short-exposure images (1.2 ms and 10 ms) can still be obtained with G-band (central wavelength $\lambda_0 = 430.71$ nm, FWHM $\Delta\lambda = 0.93$ nm, and maximum transmission $\tau_{\max} = 40\%$) and Ca II K ($\lambda_0 = 393.55$ nm, $\Delta\lambda = 1.04$ nm, and $\tau_{\max} = 16\%$) interference filters. The diffraction limit of the 0.7-meter VTT is $\lambda/D = 0.127''$ and $0.116''$ at 430.7 nm and 393.3 nm, respectively.

An Imager MX 50M CMOS camera from LaVision GmbH, Göttingen, Germany (LaVision 2021b) is used for image acquisition. The camera is controlled by the DaVis software (version 10.2, LaVision 2021a), which provides an easy and intuitive graphical user interface (GUI). The large sensor format of 36.4 mm × 27.6 mm motivated the choice of this detector for the acquisition of spectroscopic data with the VTT Echelle spectrograph, but it also proved to be advantageous for wide-field imaging. This camera records 48 megapixels at a frame rate of 30 Hz. The full well capacity is 14 500 e$^{-1}$, and the maximum quantum efficiency is 62% at 500 nm. The CMOS sensor has 7920 × 6004 pixels with a pixel size of 4.6 $\mu$m × 4.6 $\mu$m, and the digitization depth is 12 bits. The plate scale is 0.040″ pixel$^{-1}$. Thus, the G-band and Ca II K images are oversampled by a factor of 1.6 and 1.4, respectively. However, the available space on the optical rail and the available achromats for the transfer optics led to some compromises in the optical setup. Consequently, the entire circular FOV could not be captured, so that it is clipped at the top and bottom of the detector, and a smaller region-of-interest (ROI) could be selected in the horizontal direction, resulting in 6852 and 6848 pixels, respectively.

A data acquisition rate of 30 Hz can be achieved when writing to memory. Therefore, the nominal cadence for writing datasets with 100 frames is 3.33 s. This cadence is sufficient for features with horizontal flow velocities of less than 10 km s$^{-1}$, which will not cross a pixel during this time. Thus, the underlying assumption for image restoration is assured, that is, the object is stationary while the seeing fluctuates and the wavefronts are changing. However, when writing to eight solid state drives (SSDs) with 960 GB storage capacity in a RAID 0 configuration, the cadence is only about 11 s for datasets with

100 frames (8 GB), that is, some extra time is needed for writing the data. The total storage capacity is about 7.7 TB, which is enough to record 950 datasets in about three hours. Longer observing periods are possible by introducing a delay time in the data recording loop. Cadences in the range of 20 s to 30 s can be considered an acceptable compromise, considering the evolution time scale of features in the photosphere and chromosphere. For more details on the data analysis challenges related to high-cadence and large-format imagers, see Denker (2010).

High-resolution G-band observations at 430.7 nm were carried out on 2024 May 24. G-band imaging combines proxy magnetometry (Sánchez Almeida *et al.* 2001; Steiner, Hauschildt, and Bruls 2001; Schüssler *et al.* 2003; Uitenbroek and Tritschler 2006) with high spatial resolution in the blue wavelength regime. A total of 110 datasets for image restoration were acquired during the time period 09:53:28 UT – 10:32:59 UT (solar elevation 46.5° – 55.3°). Each dataset contained 100 images recorded at 30 Hz, and the cadence of the datasets was about 20 s. Seeing conditions were good to very good. The Fried parameter $r_0$ was about 7 cm during the time series as measured by the AO system, with values up to $r_{0,\max} = 11$ cm.

Figure 4.2 shows the FOV with a diameter of about 270″, containing the active region NOAA 13686 in the upper part and the four times larger active region NOAA 13685 in the lower part. The top panel shows the best G-band image of the time series, while the bottom panel shows an image, which was restored with Multi-Frame Blind Deconvolution (MFBD, Löfdahl 2002) using the best dataset. Active region NOAA 13685 (see speckle-restored G-band image in Figure 4.3 for details) was labeled as a $\beta\gamma$- and an E-region, respectively, according to the Hale and Waldmeier classification with an area of about 400 millionths of a solar hemisphere. The active region NOAA 13686 has been classified as a $\beta$- and a C-region with an area of about 100 millionths of a solar hemisphere. Earlier in its evolution, this region was the source of three M-class and several C-class flares. Both regions were in or entering the decay phase at the time of the observations.

High-resolution Ca II K observations (for chromospheric diagnostics see Carlsson, De Pontieu, and Hansteen 2019) were carried out on 2024 May 28 during the three time periods 07:51:35 UT – 08:59:36 UT (top panel of Figure 4.4), 09:13:28 UT – 09:24:20 UT (bottom panel of Figure 4.4), and 09:35:51 UT – 09:46:48 UT. The corresponding ranges for the solar elevation were 20.1° – 35.0°, 37.8° – 40.4°, and 42.6° – 45.3°, respectively. The three time series contained 180, 20, and 20 datasets, respectively, and the cadence of the datasets was about 20 s. The diameter of the FOV (about 264″) was slightly smaller compared to the May 24 observations because the differential rotation compensation was not working at that time and the first time series was longer. Thus, this motion was off-loaded to the tip-tilt mirror of the AO system reducing the common FOV. Seeing conditions were good to excellent. The Fried parameter $r_0$ was mostly around 7 cm, with $r_0$ values up to $r_{0,\max} = 22$ cm at moments of excellent seeing. Some restoration artifacts are visible at the periphery of the FOV, mainly on the eastern side. In addition, since the experimental optical setup was not covered by a protective box, some dust particles settled on the interference filter, which is very close to the the focal plane, causing artifacts that could not be corrected by flat-fielding.

The observations covered the active region NOAA 13691 and the positive-polarity pores of the active region NOAA 13695 (top panel of Figure 4.4) as well as the active region NOAA 13693 (bottom panel of Figure 4.4). The active region NOAA 13691 was classified as a $\beta\gamma\delta$- and an E-region, with an area of about 480 millionths of a solar hemisphere. Although this complex active region was still compact, its decay had already begun, and the region fragmented more and more during its disk passage, producing three C-class flares before it rotated off the disk on June 6. The much smaller active region NOAA 13693 was classified as a $\beta$- and a D-region, with an area of about 40 millionths of a solar hemisphere, which is close to its maximum size of 50 millionths of a solar hemisphere on the next day. This active region appeared on the solar surface two days before the observations and produced five M-class flares and one C-class flare one day after the observations. Speckle-restored Ca II K images of the active regions NOAA 13691 and 13693 (top and bottom panels of Figure 4.5, respectively) zoom in on details of pores, penumbrae, light bridges, umbral dots, and small-scale brightenings.

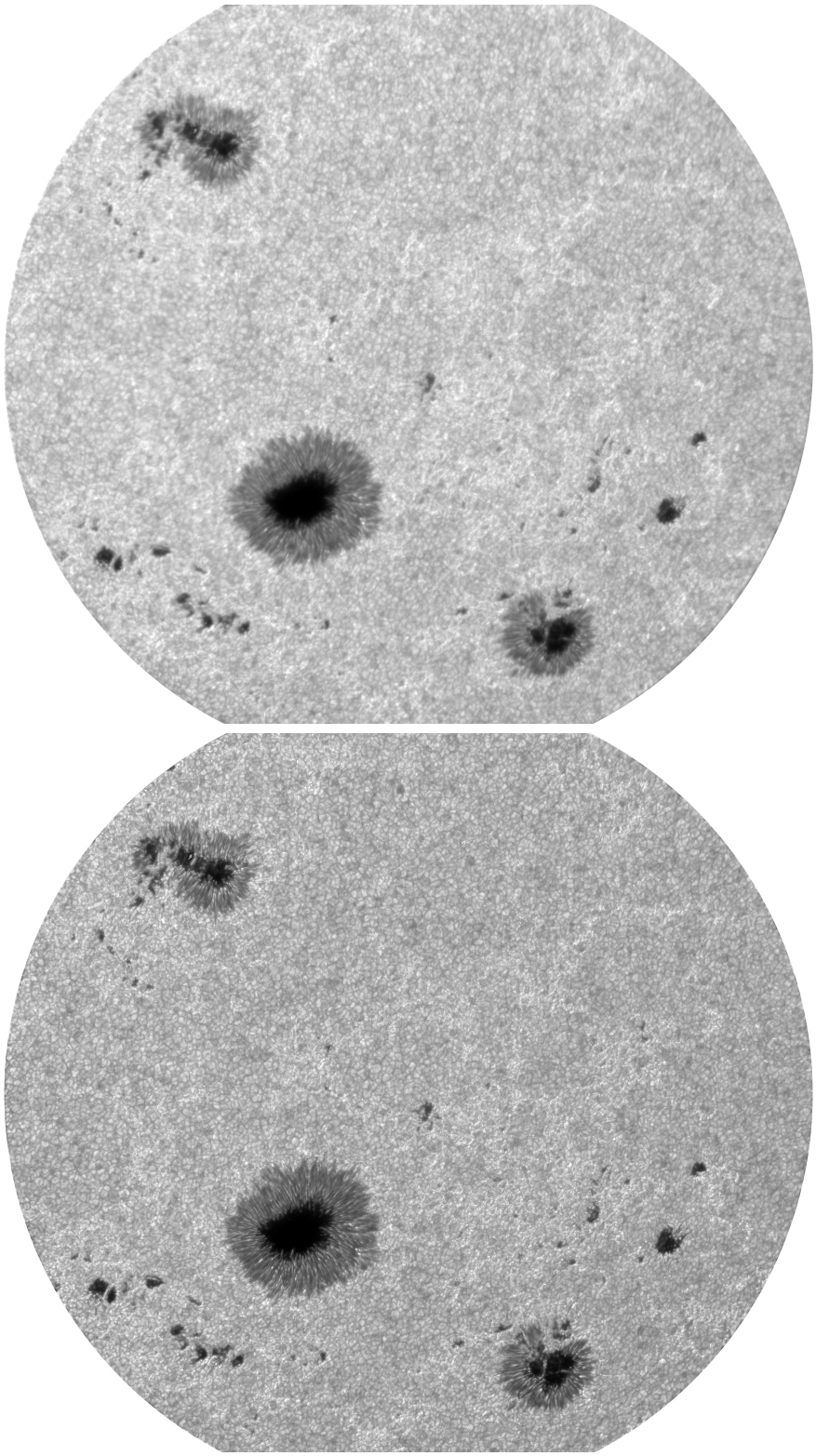

**Figure 4.2** Best of 100 G-band images (top), showing active regions NOAA 13685 (W28.5°, S13.6°) and 13686 (W19.7°, S7.7°) observed with the VTT at 10:03:32 UT on 2024 May 24, and the corresponding MFBD-restored G-band image (bottom) using all 100 images of the dataset. The diameter of the FOV is approximately 270″.

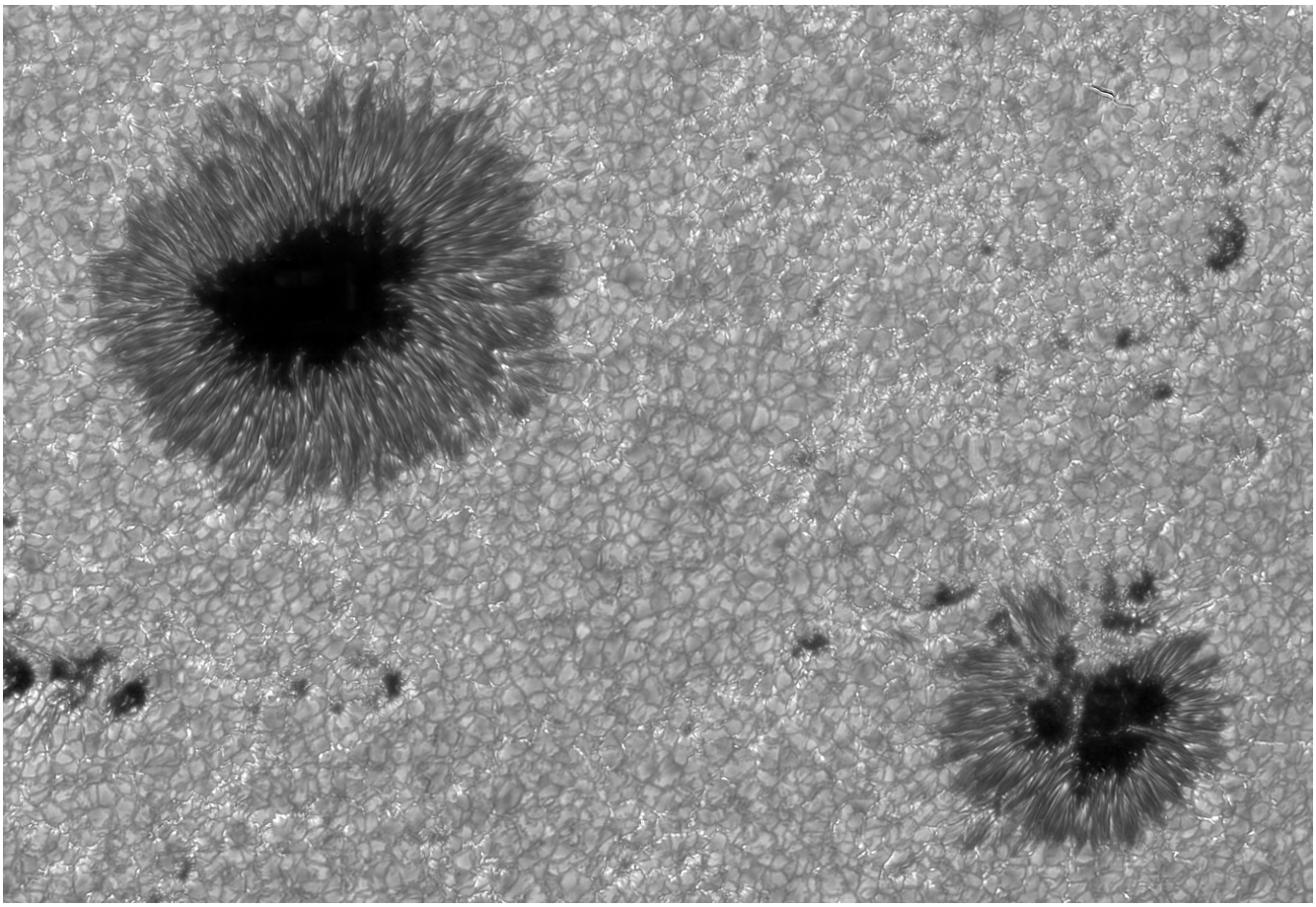

**Figure 4.3** Speckle-masking restored G-band, showing a zoom-in of the active region NOAA 13685. The size of the region-of-interest (ROI) is $140'' \times 96''$.

## 4.3 Results

The scientific capabilities of the wide-field imaging system are demonstrated in the following sections. However, it is not the intention of this work to embark on a scientific exploitation of these data, which is deferred to a future publication.

### 4.3.1 Image Restoration

The wide-field G-band (bottom panel of Figure 4.2) and Ca II K (Figure 4.3) images are restored using MFBD (Löfdahl 2002). The "sTools" data processing pipeline (Kuckein *et al.* 2017) is written in the Interactive Data Language (IDL) and provides an interface to the original MOMFBD C++ code for parallel processing (van Noort, Rouppe van der Voort, and Löfdahl 2005), which includes MFBD image restoration as a particular case. A detailed description of the tools for imaging spectroscopy and image restoration is given in Denker *et al.* (2018a) for data from the GREGOR solar telescope (Schmidt *et al.* 2012). However, new features had to be implemented in the sTools IDL code because in the case of a circular FOV, no image information is available outside the FOV. Therefore, the part of the image that is unilluminated is padded with data from the central part of the FOV. Note that a newer version of the MOMFBD inversion code (REDUX, Löfdahl *et al.* 2021) implements a more fine-grained bookkeeping scheme that specifies the isoplanatic patches to be restored by the MFBD algorithm. Overlapping stacks of image tiles of $128 \times 128$ pixels, corresponding to $5.1'' \times 5.1''$, were restored individually, using 60 Karhunen–Loève modes in the MFBD algorithm. The restored tiles are assembled as a mosaic, with a smooth transition for the overlapping parts, before the circular FOV is cut out in the final step. A wide-field MFBD restoration of one dataset with 100 images takes about five hours (285 min) on an AMD Ryzen Threadripper 3970X CPU with 32 cores and two threads per core and with 256 GB of memory. Restoring a one-hour time series of 180 datasets takes about 15 days.

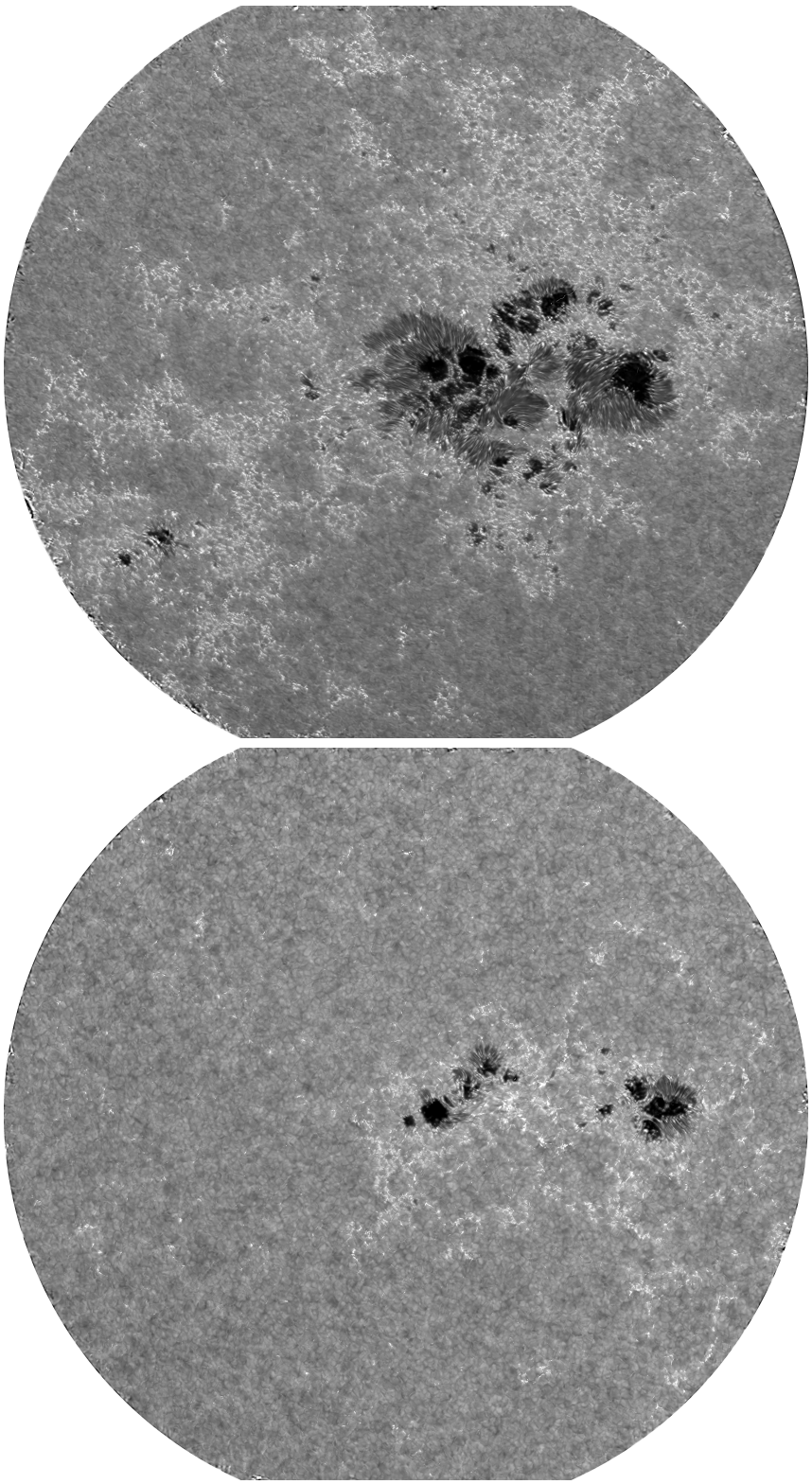

**Figure 4.4** MFBD-restored Ca II K images based on 100 short-exposure images, showing the active regions NOAA 13691 (E31.7°, N21.4°) observed at 08:31:20 UT on 2024 May 28 (top) and NOAA 13693 (E18.9°, N3.7°) observed at 09:15:48 UT on 2024 May 28 (bottom). The diameter of the FOV is approximately 264″.

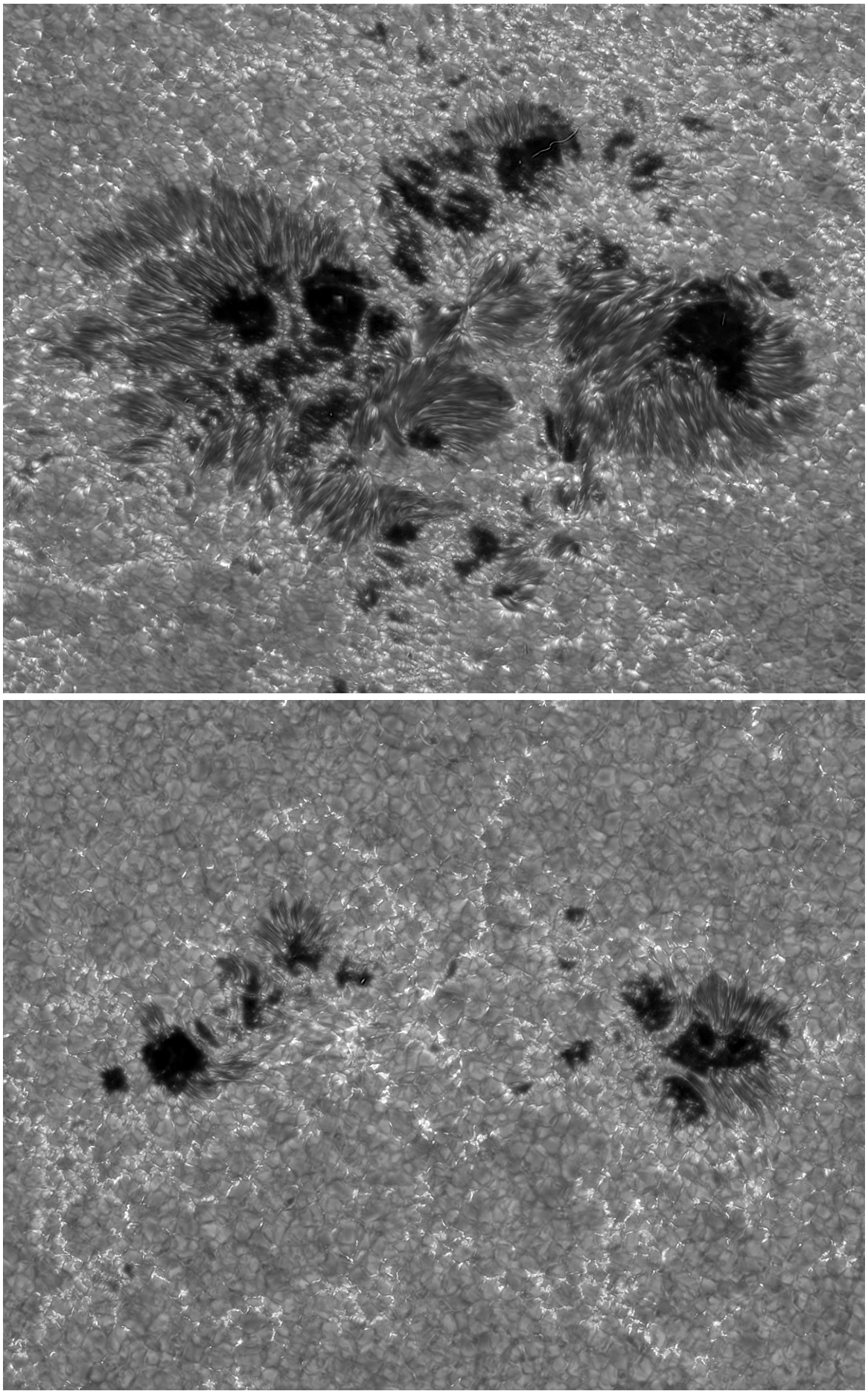

**Figure 4.5** Speckle-masking restored Ca II K image, showing a zoom-in of active regions NOAA 13691 (top) and NOAA 13693 (bottom). The size of the ROI is $120'' \times 96''$.

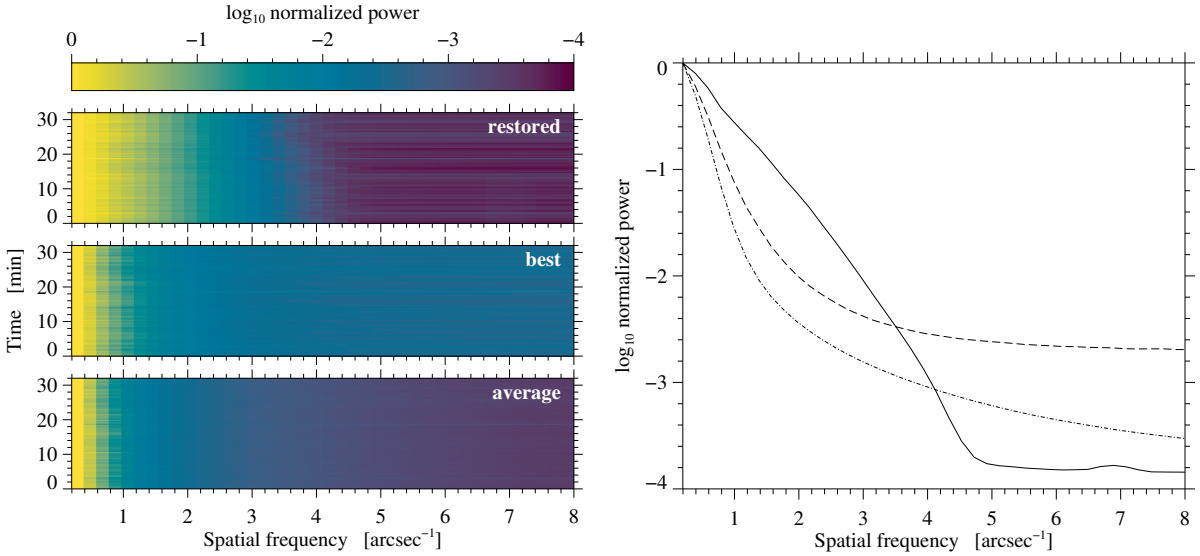


**Figure 4.6** Temporal evolution of 90 one-dimensional power spectra (left) computed for the average, best, and speckle-restored images of each dataset. The power spectrum profiles of the best dataset (right) were selected to better compare the general shape of the average (dash-dotted), best (dashed), and speckle-restored (solid) power spectra.

Speckle masking is another image restoration technique commonly used in solar imaging. The sTools data processing pipeline also provides an interface to the Kiepenheuer Institute Speckle Interferometry Package (KISIP, Wöger and von der Lühe 2008; Wöger, von der Lühe, and Reardon 2008). Examples of restored images are shown in Figures 4.3 and 4.5 for smaller ROIs. The speckle-restored G-band image has $3500 \times 2400$ pixels. It represents a mosaic that was assembled from $58 \times 40$ overlapping isoplanatic patches with a size of $128 \times 128$ pixels. Computing a restored G-band image takes about 3 min on the aforementioned compute server, meaning that the entire G-band time series can be restored in less than six hours.

The pupil of the VTT contains a central obscuration (12% of the aperture diameter) caused by a 45°-mirror which reflects a small part of the light to a guiding telescope. The four struts supporting this mirror are also visible in the pupil image. The shape of the pupil is shown in Figure 4 of Beck, Rezaei, and Fabbian (2011), which also shows the non-uniform illumination of the pupil caused by the coelostat system. The authors studied the straylight contribution to the slit spectra, which is surprisingly one of the few investigations considering the VTT pupil geometry, given the pioneering work with adaptive optics, image restoration, imaging spectropolarimetry, and spectroscopy with the high-spectral resolution echelle spectrograph. The non-uniform pupil illumination affects the spatial resolution, which is different along the short and long axis of the pupil oval. This also affects the power spectra. Pupil illumination is not taken into account in either speckle-masking image restoration or MFBD. However, the circular pupil function and the amount of AO correction with distance from the AO point is taken into account in both methods (for speckle-restored images see Puschmann and Sailer 2006; Wöger and von der Lühe 2007). Since the pupil geometry can be handed over to the MFBD code as private data, the time dependent pupil illumination could be directly implemented.

In discussing the power spectra of the restored images, the G-band time series was chosen because of the higher solar elevation, which results in a more circular pupil illumination. In addition, the G-band morphology of the quiet Sun is closer to continuum images of granulation, which can be assumed to be uniform and isotropic at the disk center. The temporal evolution (Figure 4.6) and field dependence (Figure 4.7) of the power spectra provide two means of quantifying the performance of wide-field image restoration.

For the first 90 datasets of the zoomed-in G-band images (see Figure 4.3), quiet-Sun power spectra were computed for 1340 (overlapping) isoplanatic patches with $128 \times 128$ pixels. Power spectra were computed before the restored image is assembled from the mosaic of isoplanatic patches because merging of images tiles produces power at high spatial frequencies. This spurious power obfuscates measuring the spatial resolution. One-dimensional power spectra were computed for horizontal and vertical intensity traces using Lomb-Scargle (LS) normalized periodograms (Lomb 1976; Scargle 1982; Press *et al.* 1992,

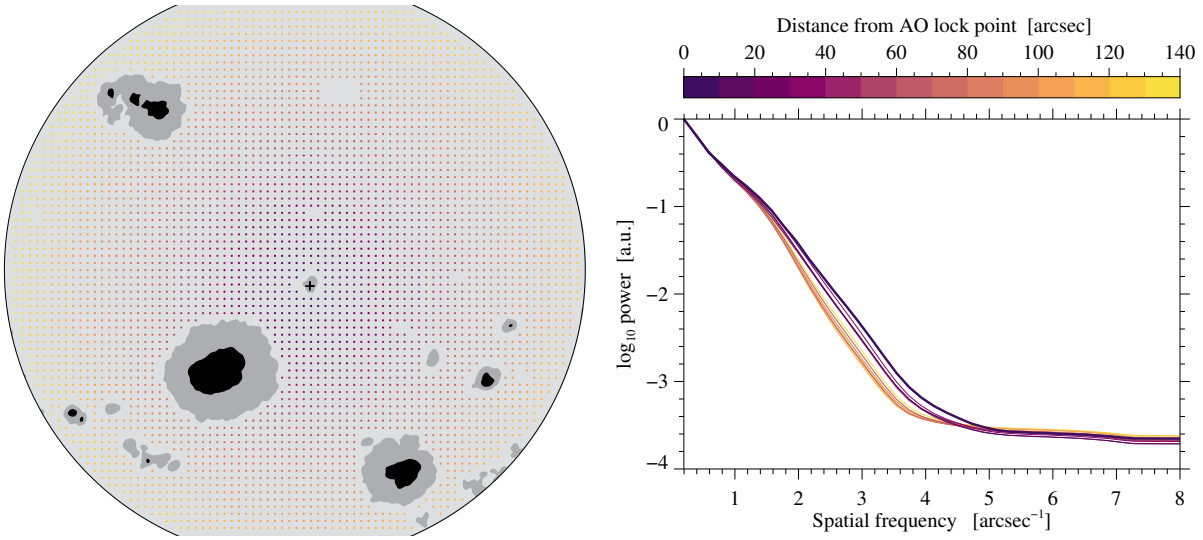


**Figure 4.7** Schematic sketch (left) showing the locations for which the one-dimensional spectra were computed. The circle outlines the circular FOV and the cross marks the location of the AO lock point, that is, a small pore. The lock point is slightly off-center with respect to the FOV. One-dimensional power spectra (right) were averaged over 14 annuli with a width of 10″ centered on the AO lock point. The power spectrum for the central part is represented by a thicker line. Regions with sunspots and pores and a region containing some artifacts in the upper-right part of the FOV were excluded from the averaging.

Section 13.8) without oversampling. Periodograms deliver power spectra for non-uniform data, which converge to FFT power spectra in the limit of equal spacing. The LS periodograms weigh the input signal per point and not by interval, which can produce superior results than FFT methods, for example with respect to aliasing. In addition, the LS periodograms are normalized by the variance of the noise, for example, random noise with a Gausian distribution will result in a power spectrum where mean and variance are unity.

In the computation of the LS power spectra, intensity traces have been omitted for 10 columns and rows at the edges of the image tiles due to the apodization window of the speckle-restored data. The average one-dimensional power spectrum is calculated by first averaging 108 horizontal and 108 vertical power spectra, and then by taking the mean of all the quiet-Sun isoplanatic patches in a dataset. The one-dimensional power spectra were computed for the image tiles of the average image, the best image, and the speckle-restored image of each dataset. The temporal evolution of the power spectra is shown in the left panel of Figure 4.6. The color-coded bar shows decreasing power spectral densities from left to right. Colorblind-friendly color scales have been used in all figures. The increase in power spectral density from the lower to the upper panel is clearly visible. Furthermore, the temporal evolution of seeing is very similar in all three panels. The frequency, where the power spectrum becomes horizontal, indicates the range where the signal is dominated by noise. The plotting range was truncated at a spatial frequency of 8 arcsec$^{-1}$, which corresponds roughly to the diffraction limit. However, since the data were oversampled, the highest spatial frequency corresponds to about 12 arcsec$^{-1}$, also the power spectrum of the average image becomes flat at high frequencies.

The right panel of Figure 4.6 shows the one-dimensional power spectra for the best dataset of the time series. The diffraction limit of $\lambda/D$ or $1.22\lambda/D$ corresponds to the spatial frequencies 7.9 arcsec$^{-1}$ and 6.5 arcsec$^{-1}$, respectively. A similar analysis was already presented in Figure 4 of Denker *et al.* (2005). The power of the speckle-restored data extends to a spatial frequency of about 5 arcsec$^{-1}$, which corresponds to a spatial resolution of about 0.2″. Considering that the pupil was not fully illuminated, that is, the aspect ratio of the long and short axis of the two-dimensional power spectrum was about 1.1, the spatial resolution is reduced by about 5%. In addition, geometric foreshortening of granulation can also lead to oblong power spectra (Wilken *et al.* 1997). More importantly, seeing conditions were only good to very good during the time series, so a higher spatial resolution could be expected in very good to excellent seeing conditions.

The field-dependence of quiet-Sun power spectra was computed for the 90 datasets of the MFBD-restored G-band images with the full FOV (see Figure 4.2). Intensity thresholds of 0.5 and 0.9 times the quiet-Sun intensity were used, after significant smoothing of the average MFBD-restored image, to create

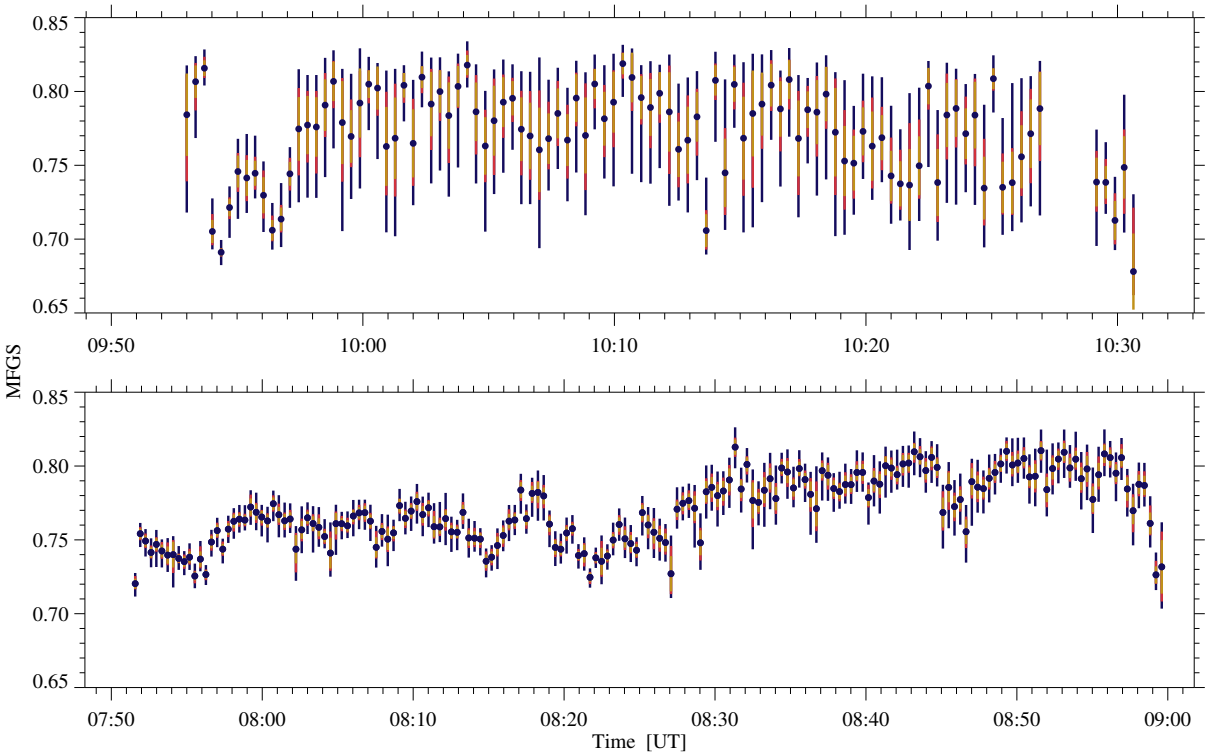


**Figure 4.8** MFGS values for the G-band time series ($n = 105$) on 2024 May 24 (top) and the first Ca II K time series ($n = 180$) on 2024 May 28 (bottom). The black circles indicate the mean value of a dataset, while the vertical bars cover the range between the mean ± standard deviation (gold), between the 10$^{\text{th}}$ and 90$^{\text{th}}$ percentiles (red), and between the minimum and maximum (blue). The AO lost its lock towards the end of the G-band time series, thus, some MFGS are missing.

a mask of major pores and sunspots with penumbra and umbra. Isoplanatic patches containing parts of sunspots and major pores and a region with flat-fielding artifacts were excluded from further analysis. Minor pores are not included in the mask but were excluded in the subsequent power spectrum analysis as well. The procedure to compute the one-dimensional power spectra is similar to that described above. The 4167 locations of the isoplanatic patches, for which the one-dimensional power spectra are computed, are marked by color-coded bullet points in the left panel of Figure 4.7. The colors correspond to the distance from the AO lock point in increments of 10″. The lock point is slightly offset from the center of the FOV. The power spectra are then averaged at each location over the 90 datasets.

The one-dimensional quiet-Sun power spectra are averaged over 10″-wide annuli to show their field dependence without crowding the display. The results are shown in the right panel of Figure 4.7, where the distance from the AO lock point is color coded. The 14 power spectra show a monotonic decrease down to a spatial frequency of about 4 arcsec$^{-1}$ before reaching a constant power level at about 5 arcsec$^{-1}$. These spatial frequencies correspond to a spatial resolution of 0.20″ to 0.25″. This is about twice the diffraction-limited resolution of 0.127″. The average power spectrum of the central part of the FOV extends farthest toward higher spatial frequencies, whereas other power spectra are shifted to lower frequencies with increasing distance from the AO lock point. The power spectra cover two regimes, that is, the purple power spectra up to distance of 60″ from the AO lock point still benefit from the AO correction, while at larger distances the orange-yellow power spectra cluster, indicating the absence of AO correction. The decrease in spatial resolution from the center to the periphery of the FOV is 10 – 15%. The Fried parameter in the periphery of the FOV was $r_0 = (5.2 \pm 0.2)$ cm (see Section 4.3.2 for details and limitations). Based on the average power spectra, the spatial resolution of the speckle-restored data is 5 – 10% higher compared to MFBD-restored data. In summary, the analysis of power spectra shows that the spatial resolution is moderately field dependent, that is, the field dependence escapes visual inspection.

The current image restoration results confirm the findings of Puschmann and Beck (2011), who concluded that the overall performance of both image restoration approaches is very similar, that is, differences easily escape visual inspection. The main difference is the much shorter computation time for the speckle-masking technique. Both methods can be used for wide-field image restoration. Image

restoration over a large FOV becomes feasible because AO correction removes significant aberrations originating from the telescope and transfer optics. In particular, the entrance window of the vacuum tank can be a source of significant aberrations due to heat transfer to the window and its mounting, which causes mechanical stress in the window. Once these aberrations are reduced, wide-field image restoration becomes possible at an observatory site with very good to excellent seeing conditions. As a side note, image restoration was introduced at the VTT (de Boer and Kneer 1992; de Boer 1993) much earlier than the first steps towards AO at the VTT (Soltau *et al.* 1997). The first CCD cameras for speckle-masking imaging had $384 \times 286$ pixels, 8- or 12-bit digitization, and frame rates of up to 6 Hz. The current observations at the VTT demonstrate the impressive development of camera and detector technology over the last decades.

### 4.3.2 Seeing Characterization

Figure 4.8 shows the temporal evolution of the image quality during the G-band and Ca II K observations. The image quality is directly related to the prevailing seeing conditions. The Median Filter Gradient Similarity (MFGS, Deng *et al.* 2015) method was used to track the seeing variability during the observations and to identify the best datasets (see Figures 4.2 – 4.5). This MFGS method was slightly modified by using a more accurate calculation of the image intensity gradients (Denker *et al.* 2018c). The MFGS method returns values in the interval [0, 1], where higher values indicate better image quality, which translates into better seeing conditions when observing the same object on the solar surface. The method is also fairly insensitive to the image content. The MFGS was computed for the central region of the FOV with a size of $3426 \times 3002$ pixels ($137'' \times 120''$), using a 2×2-pixel binning to reduce the computation time. Consequently, problems arising from the circular FOV were not an issue in computing the MFGS. The MFGS is computed for each image in a dataset, and Figure 4.8 summarizes the key statistical properties of the MFGS distribution for each dataset as a function of time. The mean value of each dataset is shown as a filled black circle. The mean value ± standard deviation is indicated by the gold-colored bar. The red bar highlights the $10^{\text{th}}$ and $90^{\text{th}}$ percentiles, and the blue bar covers the entire range of MFGS values.

The G-band MFGS values were high for the first three datasets and then dropped considerably for the next 10 datasets before recovering. Towards the end of the observing run, seeing conditions deteriorated and the AO system was no longer able to lock on to the pore in the center of the FOV. The color-coded bars in the plot panel can be viewed as a simplified histogram of the MFGS values in a dataset, providing access to the basic properties of the distribution functions. Some of the narrowest distributions belong to moments of the best and worst seeing conditions. The Ca II K MFGS values improved during the one-hour observing run, and only at the very end did the values drop rapidly. This general trend is accompanied by variations on shorter time scales. Overall, the MFGS variation in the datasets of the Ca II K time series is smaller compared to the G-band data, indicating that the seeing fluctuates less during the individual datasets. However, the mean MFGS values cannot be directly compared because of the different wavelength regions, which map different atmospheric heights from the photosphere to the chromosphere. Considering only continuum images of granulation and based on the experience with image restoration at the VTT and the GREGOR solar telescope, lower MFGS values are expected at shorter wavelength. In addition, although the MFGS method is less sensitive to the image content compared to other image quality metrics (Popowicz *et al.* 2017), the very different scenes observed on the Sun will also affect the results.

The observing conditions can be assessed either by seeing parameters (Figure 4.9) or by image quality metrics (Figure 4.10). The former are based on the analysis of time-series data, while the latter can be derived directly from a single image. One of the most commonly used seeing parameters is the Fried parameter $r_0$ (Fried and Mevers 1974), which has been derived using the spectral-ratio technique (von der Lühe 1984). Ideally, the observed scene on the solar surface should be a quiet-Sun region at the solar disk center, exploiting the uniform and isotropic properties of the granulation, see the middle panel in the last row of Figure 4 in Denker *et al.* (2007). In time series of AO-corrected images, the theoretical models of the long- and short-exposure transfer functions (Fried 1966; Korff 1973) are no longer directly applicable. However, Cagigal and Canales (2000) proposed a generalized Fried parameter $\rho_0$ that takes into account the partial wavefront compensation by an AO system. In the periphery of a larger FOV, where the incoming wavefront is minimally, if at all, corrected by the AO system (i.e., $\rho_0$ approaches $r_0$), the

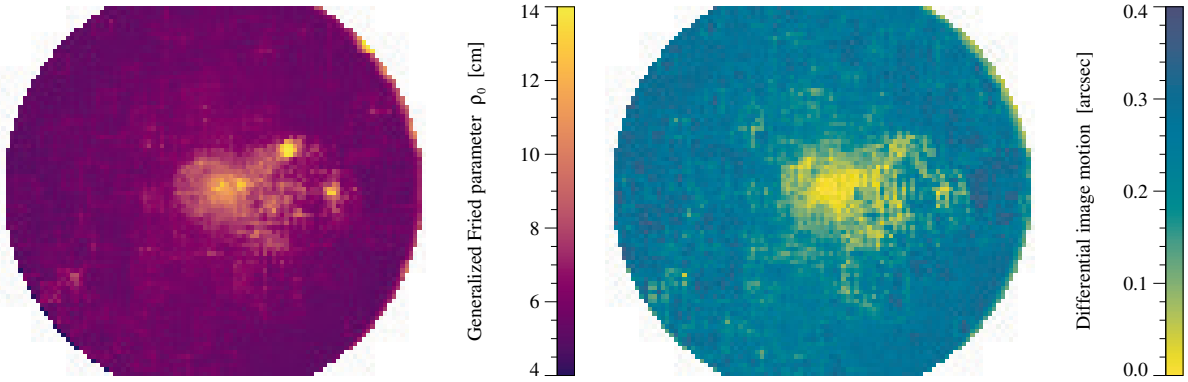


**Figure 4.9** Seeing parameters: Maps of the generalized Fried parameter $\rho_0$ (left) and the differential image motion (right). The results represent an average over the first Ca II K time series with 180 datasets.

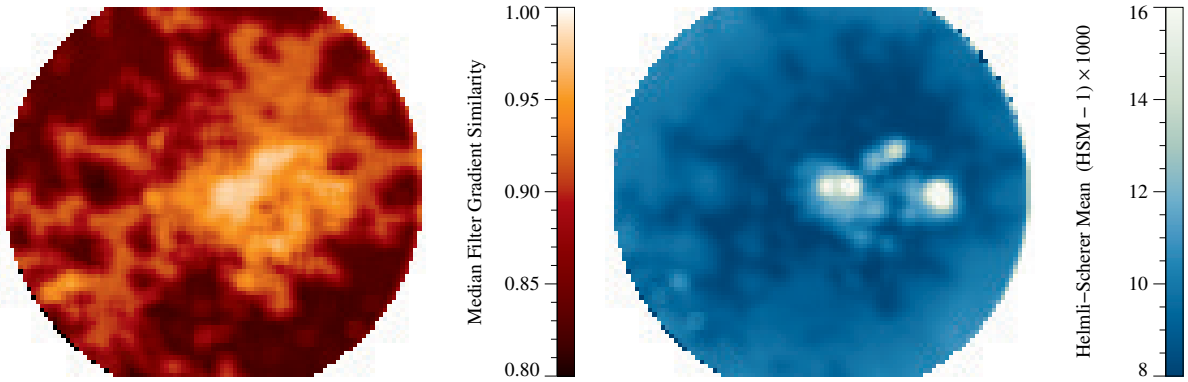


**Figure 4.10** Image quality metrics: Maps of the MFGS (left) and the HSM (right). The results represent an average over the first Ca II K time series with 180 datasets.

spectral ratio technique provides the Fried parameter $r_0$ representing the free atmosphere. Despite these caveats, the generalized Fried parameter $\rho_0$ based on the formalism of the spectral ratio technique can be used to study the performance of an AO system (Mikurda and von der Lühe 2006; Denker *et al.* 2007).

Of similar importance is the differential image motion (DIM), which is the basis for a certain class of seeing monitors. Early results on the field dependence of the level of AO correction were presented by Denker *et al.* (2005, 2007). In particular, the right panel in last row of Figure 4 in Denker *et al.* (2007) shows results derived from granulation data, where the field dependence is independent of any high-contrast features such as sunspots, pores, and bright plages. Overlapping sampling windows of $128 \times 128$ pixels were used to compute these seeing parameters for stacks of 100 image tiles, resulting in two-dimensional maps of the circular FOV with up to 100 values in the horizontal direction and 86 values in the vertical direction. These maps were averaged over the first Ca II K time series comprising 180 datasets. Two image quality metrics were also computed for the same datasets, that is, the MFGS and the Helmli-Scherer mean (HSM, Helmli and Scherer 2001). Additional information and details can be found in Kamlah *et al.* (2021), who compared image quality metrics and seeing parameters and investigated their wavelength dependence for time series of AO-corrected images.

The lock point of the AO system was the easternmost umbra of the main spot in active region NOAA 13691, from which the sunspot group extends westward. The highest Fried parameters $r_0$ are associated with the sunspot umbrae (see left panel of Figure 4.9). Surprisingly, the umbra at the lock point does not have the highest $r_0$ values. However, a halo of high $r_0$ values surrounds this umbra, indicating a circular region with a radius of about 15″ that benefits from the AO correction. Overall, dark contrast features such as umbra and penumbra leave an imprint on the two-dimensional map of the Fried parameter $r_0$. Moving away from the central FOV toward the periphery, one encounters Fried parameters $r_0 = (3.9 \pm 0.7)$ cm, which are fairly evenly distributed. More than 750 isoplanatic patches were selected in the periphery to compute the mean and the standard deviation, which refer to the time series of 180 datasets. The typical standard deviation within a dataset is only 0.4 cm. In addition, the

Pearson correlation coefficient between the peripheral Fried parameter and the MFGS (see lower panel of Figure 4.8) is $\rho = 0.84$, indicating that the image quality metrics and seeing parameters are strongly correlated. The imprint of contrast features on the two-dimensional DIM map is more diluted (see right panel of Figure 4.9), with a more pronounced and extended region of low DIM around the AO lock point. The DIM is uniformly around 0.3″ in the periphery of the FOV.

The shape and structure of the two-dimensional MFGS and HSM maps (Figure 4.10) are very different from seeing parameter maps (Figure 4.9). The Ca II K brightenings dominate the image quality metrics. The highest MFGS values are associated with the sunspot umbrae and penumbrae. However, their appearance is more washed out compared to the HSM map where the umbrae clearly dominate. Interestingly, the Ca II K brightenings lead to lower HSM values so that the HSM becomes larger again in the periphery. Consequently, image quality metrics are only useful to determine the field dependence of the AO correction when applied to uniform and isotropic solar features such as solar granulation at disk center. Unfortunately, such data were not collected during the proof-of-concept observations for wide-field image restoration. On the other hand, seeing parameters (Figure 4.9) and image quality metrics (Figure 4.10) are important to assess the data quality of time series following the temporal evolution of solar features. In addition, they add information to archived data, potentially opening them up for "big data" applications. This lead to increased efforts to better understand the methods, their advantages, and shortcomings (Deng *et al.* 2015; Popowicz *et al.* 2017; Denker *et al.* 2018a,c; Kamlah *et al.* 2021; So *et al.* 2024).

### 4.3.3 Background-subtracted Solar Activity Maps

The goal of data visualization with BaSAMs is to easily identify features or regions that show strong intensity $\langle|I - \langle I\rangle|\rangle$ or magnetic field $\langle|B - \langle B\rangle|\rangle$ variations (Denker and Verma 2019), where $\langle\ldots\rangle$ denotes the ensemble mean. The seeing conditions during the G-band observations on 2024 May 24 were good enough to restore the first 90 datasets using the speckle-masking method. Only one restoration failed and was replaced by the average of the restored images immediately before and after that event. For clarity, only a $140'' \times 96''$ ROI was chosen (see Figure 4.3) to study the G-band intensity variations (Figure 4.11) in detail. The 30-minute time series of restored G-band images was aligned with respect to the average restored image using cross-correlation techniques. Much of the rigid image motion of ±4 pixels or 0.16″ peak-to-valley was removed by full-pixel shifts. Differential image motion was removed using a destretching algorithm with a 64×64-pixel kernel. The intensity of the restored image was normalized with respect to the quiet Sun, that is, a region of $600 \times 440$ pixels between the two large sunspots of active region NOAA 13685, which was free of any small-scale G-band brightenings. Finally, a subsonic filter was applied to remove the signal of the five-minute oscillations from the time series.

The intensity values of the G-band BaSAM are clipped at 0.1% of the brightest and darkest values, which greatly enhances the contrast. In addition, the color scale is displayed without units, as quantifying the intensity variations is not the primary purpose of BaSAMs. Solar disk center is towards the upper-left corner of the G-band BaSAM, and the limb is towards the lower-right corner. Intensity variations are significantly stronger in the limb-side penumbra of both sunspots and weaker at their peripheral penumbra. This is caused by the inward motion of penumbral grains in the inner penumbra and their outward motion in the outer penumbra, which is accompanied by upwelling granules squeezing out in between penumbral filaments (Sobotka, Brandt, and Simon 1999). The observed asymmetry is only caused by the viewing geometry near the solar limb. The faint and strong light bridges in the smaller, leading sunspot are also locations of increased activity, signalling the sunspot's decay. A pore at the upper end of the strong light bridge on the northern side of the sunspot has already broken up the sunspot's penumbra. Some stronger variations are also associated with this process. Both sunspots are surrounded by an annulus of enhanced intensity variations that fills up the space of the supergranular cell in which the sunspot is embedded (Verma *et al.* 2012; Verma, Kummerow, and Denker 2018a). This annular pattern is associated with the moat flow (Hagenaar and Shine 2005). Interestingly, much of the area around the sunspots is occupied by G-band bright points that produce as strong BaSAM signal, while the region between the sunspots is the largest, continuous, quiet region.

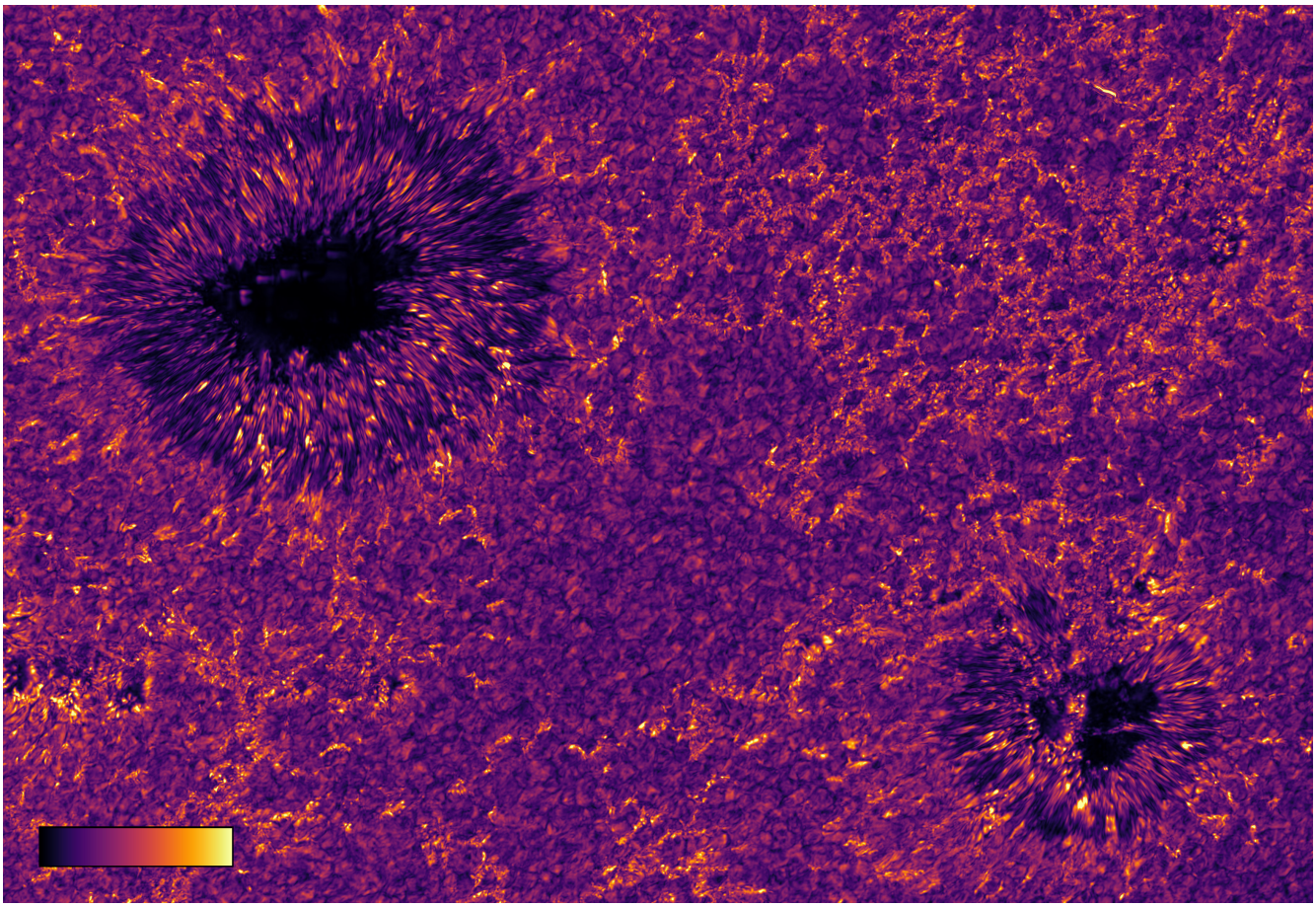

**Figure 4.11** G-band BaSAM of active region NOAA 13685 corresponding to Figure 4.3, which shows the intensity variation $\langle |I - \langle I \rangle| \rangle$. The color scale in the lower left corner indicates the strength of the intensity variation from low to high.

### 4.3.4 Local Correlation Tracking

The horizontal proper motions shown in Figure 4.12 were derived with LCT using the implementation of Verma and Denker (2011). The data from Section 4.3.3 were used as input. This algorithm was originally developed for time series of Hinode G-band images, which were obtained with the Solar Optical Telescope (SOT, Tsuneta *et al.* 2008). Images from SOT have a comparable plate scale of 0.054″ pixel$^{-1}$ and 0.040″ pixel$^{-1}$, respectively, so that similar settings can be used. A Gaussian kernel with $64 \times 64$ pixels was used, corresponding to about 1890 km × 1890 km on the solar surface. The FWHM of the Gaussian was 1200 km, and this kernel was used for high-pass filtering the time series of the speckle-restored G-band images and as a sampling window for computing the cross-correlations between successive images that were 60 s apart in time. Therefore, the horizontal proper motions were derived mainly for granule-sized features. Averaging over all flow maps of the 30-minute time series yields the persistent flow field of the sunspots and their surroundings.

The magnitude of the horizontal proper motions, that is, the flow speed is displayed in a colorblind-friendly color scale that covers the range from 0.0 km s$^{-1}$ to 1.5 km s$^{-1}$. The flow vectors were computed by averaging over regions of $20 \times 20$ pixels, resulting in a grid of $175 \times 120$ vectors. In both sunspots, outward flows are seen in the outer penumbra and inward flows in the outer penumbra, with a dividing line intersecting the penumbra (see the results of Section 4.3.3). This pattern is only interrupted for the missing penumbra segment of the smaller leading sunspot. Beyond the penumbra of the sunspots a second annulus of outflows extends the flow field to the boundary of the surrounding supergranular cell. While the region with G-band bright points indicates higher levels of activity in the G-band BaSAM (see Figure 4.11), the flow speeds are significantly reduced in this region due to the presence of small-scale magnetic fields. Conversely, the low-activity region between the two sunspots shows flow speed comparable to those of penumbral outflows and the moat flow. In addition, this region is characterized by a large number of divergence centers.

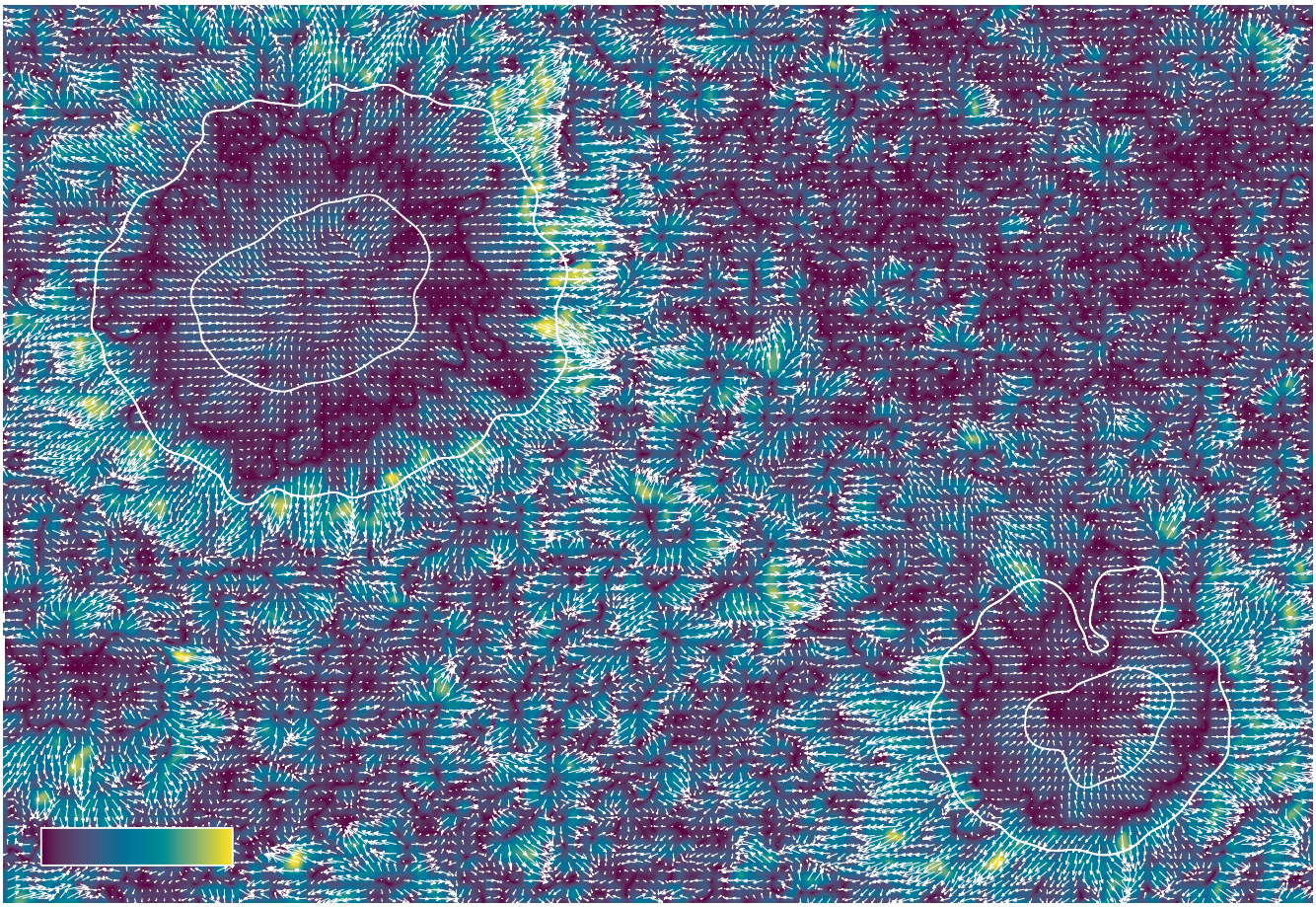

**Figure 4.12** Persistent horizontal proper motions are derived from a 30-minute time series of speckle-restored G-band images. The $175 \times 100$ flow vectors are superimposed on a flow speed map, which is displayed in the range from 0.0 km s$^{-1}$ to 1.5 km s$^{-1}$ as indicated by the color bar in the lower-left corner. Smoothed contours for the umbra/penumbra of the two major sunspots were added for intensity thresholds of 0.5/0.9 $I/I_0$, where $I_0$ refers to the quiet-Sun intensity.

## 4.4 Conclusions

Speckle-masking imaging at the diffraction limit of a solar telescope becomes more difficult with increasing aperture diameter, as illustrated by these "back of the napkin" calculations. The diffraction limit of a 4-meter aperture telescope at 500 nm is $\alpha = \lambda/D = 0.026''$. Even with currently employed 4k×4k-pixel detectors at larger-aperture telescopes the FOV is only about $50'' \times 50''$ with critical sampling. A larger FOV can only be achieved by dropping the Nyquist sampling requirement or by changing the telescope pointing to take raster scans of the solar surface. The latter case affects the temporal sampling of the observing sequence (Wöger *et al.* 2021). The pixel width with critical sampling corresponds to $0.013''$ or about 10 km on the solar surface, that is, a feature moving at 10 km s$^{-1}$ traverses the pixel in 1 s. Choosing a speed of 10 km s$^{-1}$ was motivated by rounding up the photospheric sound speed in the quiet Sun of about 8 km s$^{-1}$ (e.g., Schrijver, Hagenaar, and Title 1997; Srivastava *et al.* 2008). Therefore, a camera system with a frame rate of 100 Hz can only record 100 independent wavefront realizations assuming a daytime correlation time scale of $\tau = 10$ ms, which is in turn also the maximum possible exposure time for the short-exposure images. Typically, the speckle-masking method requires this number of images for a good wavefront statistics. In summary, dynamic and rapidly evolving features will violate some of the basic assumptions of speckle-masking imaging.

This line of arguments supports the continued operation of solar telescopes such as the VTT, where the limitations imposed by the aperture diameter are relaxed by a factor of almost six. The VTT is perfectly positioned to bridge the gap between high-spatial resolution and synoptic telescopes. The large diameter of its FOV of up to $600''$ makes it also an ideal development platform for wide-field AO systems and imaging spectropolarimeters, providing access to the physical properties of entire active regions and their surroundings at high temporal resolution. Even when using the current AO system, the

present results demonstrate the potential of the VTT for wide-field image restoration. This capability complements existing instruments at the VTT such as the HELioseismic Large Region Interferometric DEvice (HELLRIDE, Pruthvi and Roth 2023), the Laser Absolute Reference Spectrograph (LARS, Doerr *et al.* 2012; Löhner-Böttcher *et al.* 2017), and the Fast Multi-line Universal Spectrograph (FaMuLUS) camera system, all of which explore the spatial domain between 0.1″ and 1.0″. Compared to these modern instruments, the VTT's AO and telescope control systems are outdated, and their upgrades can significantly improve performance and reduce operating costs. Long-term observing programs can be easily implemented, and queue observations can provide data of consistent quality for database research. Considering the oversubscription of large-aperture telescopes, telescopes such as VTT could provide broader and easier data access, which could, for example, pave the way and lay the foundation for competitive research proposals at large-aperture telescopes. In conclusion, the present work can be seen as support and advocacy for the continued operation of the VTT.

# Chapter 5

# Conclusions

Combining high-resolution ground-based observations with synoptic space-based observations provides a powerful tool to further explain the processes associated with the formation, evolution, and decay of active regions. This research project aims to address some of the open questions in our understanding of these processes. The analyzed data in this work include imaging, filtergram, and spectro-polarimetric data observed with different instruments at different telescopes, complemented by synoptic data from the HMI on board SDO. The data have been subjected to a variety of techniques including LCT, BaSAMs, and SIR inversions. This allowed us to construct a more comprehensive picture of the evolution of the active regions and to add valuable information to some of the open questions raised in Section 1.4. Trailing, positive-polarity pores separated by light bridges were observed, which developed into a sunspot (Chapter 2). In contrast, three leading, positive-polarity sunspots with light bridges were observed in a decaying active region (Chapter 3). Finally, four active regions were observed using an experimental setup that allowed us to carry out wide-field imaging of a circular FOV with a diameter of about 270″ (Chapter 4).

The first study of this thesis was related to pores with thick granular light bridges (Kamlah *et al.* 2023). The main objective of the project was *to characterize the physical properties of the granular light bridge and its influence on the surrounding features including the penumbra*. The data were obtained at the GST and included images in TiO and imaging spectroscopic data in H$\alpha$. The line-wing H$\alpha$ filtergrams are very similar to the photospheric observations. In the higher atmospheric layers, the FOV is dominated by fibrils emanating from the pores and extending in a chromospheric canopy structure with its characteristic filamentary structure and strong dark filaments connecting surface features. The photosphere shows the most pronounced variations at umbral boundaries and in regions of flux emergence, while the chromosphere shows the most pronounced variability in the vicinity of magnetic features. The observed light bridge is characterized by bidirectional outflows along its length, as proposed by Toriumi, Cheung, and Katsukawa (2015), transporting material and magnetic flux towards the surroundings with average horizontal velocities of $(0.34 \pm 0.18)$ km s$^{-1}$. To confirm the expected convective upwelling in the center of the light bridge, it would be necessary to obtain photospheric spectropolarimetric data. It was difficult to assess the influence of plasma flows and the magnetic field configuration above the photosphere, given the presence of chromospheric filaments obscuring the light bridge. However, the chromospheric H$\alpha$ LOS velocities showed granular patterns above the light bridge. In addition, twisting motions, jets, and other small-scale features are often observed at the light bridge–umbra interface, where they act as potential contributors to coronal heating.

Three positive-polarity sunspots in active region NOAA 13096 were the focus of the work in Kamlah *et al.* (2024). The goal of this work was *to understand the interplay of magnetic fields and plasma flows associated with the formation, evolution, and decay of the sunspot*. The high-resolution observations from GREGOR are interpreted in the context of active region decay in the following days using SDO/HMI data. Only the leading sunspot had a penumbra, and the two other sunspots had rudimentary penumbrae. As expected from previous studies, no penumbra formed in the central regions where sunspots of the same polarity were facing each other. In addition, the mostly vertical field lines of three sunspots hindered the presence of an overlying chromospheric canopy, which in some cases was observed to confine the chromospheric field lines and to transform them into inclined photospheric fields to form a penumbra.

Furthermore, in narrow-band H$\alpha$ chromospheric images, the decaying active region is characterized by a triangular region between the three leading, positive-polarity sunspots with unfavorable conditions for penumbra formation. This sponge-like region showed signs of enhanced activity on small spatial scales, was free of divergence centers and exploding granules, lacked well-ordered horizontal flows, had low flow velocities, and was dominated by horizontal magnetic fields. The Evershed flow was present around all three sunspots. However, the measured average LCT velocities were close to zero. This is significantly lower than the penumbral velocities found in other studies. One interpretation of the low penumbral flow velocity is the imminent decay of the penumbra. Due to the late evolutionary stage of the sunspots, the flow velocity in the moat significantly exceeds the outflows in the penumbra. The measured moat flow was in the range of 0.2 km $s^{-1}$ to 1.0 km $s^{-1}$. In the chromospheric images, superpenumbral structures were present around all sunspots, but only the leading sunspot was surrounded by a complete and stable configuration. This work emphasized that the presence of the penumbra depends strongly on the magnetic topology of the active region and the structure of the local plasma flows. Furthermore, when a sunspot has a penumbra, both moat and Evershed flow are present, as demonstrated in this work, where even the smallest patches of penumbra are accompanied by these outflows.

The final study is a more instrumental and method-oriented study that promotes the science capabilities of the VTT, a telescope with a 0.7-meter aperture, conveniently located between telescopes for synoptic observations and observations with the highest spatial resolution. The ambition was to demonstrate *the science potential of image restoration in combination with AO-assisted wide-field imaging*. Two commonly used image restoration methods were successfully applied to time series of short-exposure photospheric G-band and chromospheric Ca II K images. Nearly diffraction-limited resolution was achieved over the entire circular FOV with a 270″ diameter, although the amplitude correction of the Fourier-transformed restored images shows some dependence with the distance from the lock point of the AO system. In addition, the techniques used in the two high-resolution science studies, namely LCT and BaSAMs, successfully demonstrated their performance on wide-field VTT imaging data. As an added bonus, image quality metrics and seeing parameters were derived, allowing data quality to be measured as a function of time. An application that is becoming increasingly important for "big data" and database research.

Further high-resolution observations of active regions are needed to gain a deeper understanding of the processes involved in their formation, evolution, and decay. Ideally, these observations should begin before the initial disturbance of the quiet Sun in the photosphere and the formation of umbral cores. To obtain a comprehensive picture, it is necessary to combine high-resolution, high-cadence imaging with high-resolution, high-cadence spectro-polarimetric data suitable for inversions. This will make it possible to link variations in the magnetic field configuration, horizontal and vertical plasma motions, and various other physical parameters such as temperature, horizontal and vertical magnetic field, inclination, azimuth, among others. Such observations should simultaneously cover several atmospheric layers of the Sun to enable a comprehensive analysis of the three-dimensional structure and morphological changes in the photosphere and chromosphere. A detailed analysis of small-scale features associated with active regions is needed to assess their impact on active region evolution and their contribution to coronal heating. In addition, the possible interaction of active regions with each other and with the Sun's large-scale flow motion needs to be further investigated. High-resolution observations of wide FOVs from smaller telescopes such as VTT can provide contextual data on global flows and magnetic structure that can complement zoom-in observations of small FOVs from large-aperture telescopes. Therefore, co-observations with different telescopes at different observatories with different FOVs and capabilities will enable observations of small features such as penumbral filaments as well as the evolution of entire sunspots, active regions, or multiple interacting active regions.

# Bibliography


Abdusamatov, H.I., Krat, V.A.: 1969, Magnetic 'Knots' in the Solar Photosphere. *Solar Phys.* **9**, 420. doi:10.1007/BF02391664.

Avrett, E.H., Fontenla, J.M., Loeser, R.: 1994, Formation of the Solar 10830 Å Line. In: Rabin, D.M., Jefferies, J.T., Lindsey, C. (eds.) *Infrared Solar Physics*, *IAU Symp.* **154**, 35. doi:10.1017/S0074180900124234.

Balasubramaniam, K.S., Pevtsov, A., Rogers, J.: 2004, Statistical Properties of Superpenumbral Whorls around Sunspots. *Astrophys. J.* **608**, 1148. doi:10.1086/420759.

Balasubramaniam, K.S., Pevtsov, A.A., Olmschenk, S.: 2008, Evershed Flow, Oscillations, and Sunspot Structure. In: Howe, R., Komm, R.W., Balasubramaniam, K.S., Petrie, G.J.D. (eds.) *Subsurface and Atmospheric Influences on Solar Activity*, *ASP Conf. Ser.* **383**, 279.

Balthasar, H., Gömöry, P.: 2008, The Three-Dimensional Structure of Sunspots. I. The Height Dependence of the Magnetic Field. *Astron. Astrophys.* **488**, 1085. doi:10.1051/0004-6361:200809575.

Balthasar, H., Muglach, K.: 2010, The Three-dimensional Structure of Sunspots. II. The Moat Flow at Two Different Heights. *Astron. Astrophys.* **511**, A67. doi:10.1051/0004-6361/200912978.

Balthasar, H., Gömöry, P., González Manrique, S.J., Kuckein, C., Kavka, J., Kucera, A., *et al.*: 2016, Spectropolarimetric Observations of an Arch Filament System with the GREGOR Solar Telescope. *Astron. Nachr.* **337**, 1050. doi:10.1002/asna.201612432.

Bard, S., Carlsson, M.: 2008, Constructing Computationally Tractable Models of Si I for the 1082.7 nm Transition. *Astrophys. J.* **682**, 1376. doi:10.1086/589910.

Beauregard, L., Verma, M., Denker, C.: 2012, Horizontal Flows Concurrent with an X2.2 Flare in Active Region NOAA 11158. *Astron. Nachr.* **333**. doi:10.1002/asna.201111631.

Beck, C., Choudhary, D.P.: 2020, Temporal Evolution of the Inverse Evershed Flow. *Astrophys. J.* **891**, 119. doi:10.3847/1538-4357/ab75bd.

Beck, C., Choudhary, D.P., Ranganathan, M.: 2020, Center-to-limb Variation of the Inverse Evershed Flow. *Astrophys. J.* **902**, 30. doi:10.3847/1538-4357/abb3bf.

Beck, C., Rezaei, R., Fabbian, D.: 2011, Stray-light Contamination and Spatial Deconvolution of Slit-spectrograph Observations. *Astron. Astrophys.* **535**, A129. doi:10.1051/0004-6361/201015702.

Beckers, J.M.: 1964, A Study of the Fine Structures in the Solar Chromosphere. PhD Thesis, University of Utrecht.

Beckers, J.M., Schröter, E.H.: 1968, The Intensity, Velocity and Magnetic Structure of a Sunspot Region. I: Observational Technique; Properties of Magnetic Knots. *Solar Phys.* **4**, 142. doi:10.1007/bf00148076.

Bellot Rubio, L.R., Schlichenmaier, R., Tritschler, A.: 2006, Two-dimensional Spectroscopy of a Sunspot. III. Thermal and Kinematic Structure of the Penumbra at 0.5 arcsec Resolution. *Astron. Astrophys.* **453**, 1117.

Berger, T.E., De Pontieu, B., Fletcher, L., Schrijver, C.J., Tarbell, T.D., Title, A.M.: 1999, What is Moss? *Solar Phys.* **190**, 409. doi:10.1023/A:1005286503963.

Berkefeld, T., Soltau, D., Schmidt, D., von der Lühe, O.: 2010, Adaptive Optics Development at the German Solar Telescopes. *Appl. Opt.* **49**, G155. doi:10.1364/ao.49.00g155.

Berkefeld, T., Schmidt, D., Soltau, D., von der Lühe, O., Heidecke, F.: 2012, The GREGOR Adaptive Optics System. *Astron. Nachr.* **333**, 863. doi:10.1002/asna.201211739.

Bharti, L.: 2015, Fine Structure above a Light Bridge in the Transition Region and Corona. *Mon. Not. R. Astron. Soc.* **452**, L16. doi:10.1093/mnrasl/slv071.

Bharti, L., Joshi, C., Jaaffrey, S.N.A.: 2007, Observations of Dark Lanes in Umbral Fine Structure from the Hinode Solar Optical Telescope: Evidence for Magnetoconvection. *Astrophys. J. Lett.* **669**, L57.

Bharti, L., Quintero Noda, C., Joshi, C., Rakesh, S., Pandya, A.: 2016, Fine Structures at Pore Boundary. *Mon. Not. R. Astron. Soc.* **462**, L93. doi:10.1093/mnrasl/slw130.

Bobra, M.G., Sun, X., Hoeksema, J.T., Turmon, M., Liu, Y., Hayashi, K., *et al.*: 2014, The Helioseismic and Magnetic Imager (HMI) Vector Magnetic Field Pipeline: SHARPs – Space-Weather HMI Active Region Patches. *Solar Phys.* **289**, 3549. doi:10.1007/s11207-014-0529-3.

Boerner, P., Kneer, F.: 1992, High Resolution Observations of the Evershed Flow. *Astron. Astrophys.* **259**, 307.

Bonet, J.A., Márquez, I., Muller, R., Sobotka, M., Roudier, T.: 2005, Phase Diversity Restoration of Sunspot Images. II. Dynamics around a Decaying Sunspot. *Astron. Astrophys.* **430**, 1089. doi:10.1051/0004-6361:20041356.

Borrero, J.M., Tomczyk, S., Kubo, M., Socas-Navarro, H., Schou, J., Couvidat, S., Bogart, R.: 2011, VFISV: Very Fast Inversion of the Stokes Vector for the Helioseismic and Magnetic Imager. *Solar Phys.* **273**, 267. doi:10.1007/s11207-010-9515-6.

Brants, J.J., Steenbeek, J.C.M.: 1985, Morphological Evolution of an Emerging Flux Region. *Solar Phys.* **96**, 229. doi:10.1007/bf00149682.

Bray, R.J., Loughhead, R.E.: 1964, *Sunspots*, The International Astrophysics Series, Chapman & Hall, London.

Brickhouse, N.S., Labonte, B.J.: 1988, Mass and Energy Flow near Sunspots. I. Observations of Moat Properties. *Solar Phys.* **115**, 43. doi:10.1007/bf00146229.

Brummell, N.H., Tobias, S.M., Thomas, J.H., Weiss, N.O.: 2008, Flux Pumping and Magnetic Fields in the Outer Penumbra of a Sunspot. *Astrophys. J.* **686**, 1454 – 1465. doi:10.1086/591640.

Bumba, V.: 1963, Development of Spot Group Areas in Dependence on the Local Magnetic Field. *Bull. Astron. Inst. Czech* **14**, 91.

Cagigal, M.P., Canales, V.E.: 2000, Generalized Fried Parameter after Adaptive Optics Partial Wave-front Compensation. *J. Opt. Soc. Am. A* **17**, 903. doi:10.1364/JOSAA.17.000903.

Cameron, R., Schüssler, M., Vögler, A., Zakharov, V.: 2007, Radiative Magnetohydrodynamic Simulations of Solar Pores. *Astron. Astrophys.* **474**, 261. doi:10.1051/0004-6361:20078140.

Cao, W., Gorceix, N., Coulter, R., Wöger, F., Ahn, K., Shumko, S., et al.: 2010a, Nasmyth focus instrumentation of the New Solar Telescope at Big Bear Solar Observatory. In: McLean, I.S., Ramsay, S.K., Takami, H. (eds.) *Ground-based and Airborne Instrumentation for Astronomy III*, *Proc. SPIE* **7735**, 77355V. doi:10.1117/12.856613.

Cao, W., Gorceix, N., Coulter, R., Ahn, K., Rimmele, T.R., Goode, P.R.: 2010b, Scientific Instrumentation for the 1.6 m New Solar Telescope in Big Bear. *Astron. Nachr.* **331**, 636. doi:10.1002/asna.201011390.

Cao, W., Goode, P.R., Ahn, K., Gorceix, N., Schmidt, W., Lin, H.: 2012, NIRIS: The Second Generation Near-infrared Imaging Spectro-polarimeter for the 1.6 Meter New Solar Telescope. In: Rimmele, T.R., Tritschler, A., Wöger, F., Collados Vera, M., Socas-Navarro, H., Schlichenmaier, R., et al. (eds.) *Second ATST-EAST Meeting: Magnetic Fields from the Photosphere to the Corona.*, *ASP Conf. Ser.* **463**, 291.

Carlsson, M., De Pontieu, B., Hansteen, V.H.: 2019, New View of the Solar Chromosphere. *Ann. Rev. Astron. Astrophys.* **57**, 189. doi:10.1146/annurev-astro-081817-052044.

Cauzzi, G., Reardon, K., Rutten, R.J., Tritschler, A., Uitenbroek, H.: 2009, The Solar Chromosphere at High Resolution with IBIS. IV. Dual-line Evidence of Heating in Chromospheric Network. *Astron. Astrophys.* **503**, 577. doi:10.1051/0004-6361/200811595.

Chae, J., Denker, C., Spirock, T.J., Wang, H., Goode, P.R.: 2000, High-resolution H$\alpha$ Observations of Proper Motion in NOAA 8668. Evidence for Filament Mass Injection by Chromospheric Reconnection. *Solar Phys.* **195**, 333.

Chae, J., Park, H., Ahn, K., Yang, H., Park, Y., Nah, J., *et al.*: 2013, Fast Imaging Solar Spectrograph of the 1.6 Meter New Solar Telescope at Big Bear Solar Observatory. *Solar Phys.* **288**, 1. doi:10.1007/s11207-012-0147-x.

Chae, J., Song, D., Seo, M., Cho, K.S., Park, Y.D., Yurchyshyn, V.: 2015, Detection of Shock Merging in the Chromosphere of a Solar Pore. *Astrophys. J. Lett.* **805**, L21. doi:10.1088/2041-8205/805/2/L21.

Cheung, M.C.M., Rempel, M., Title, A.M., Schüssler, M.: 2010, Simulation of the Formation of a Solar Active Region. *Astrophys. J.* **720**, 233. doi:10.1088/0004-637x/720/1/233.

Choudhary, D.P., Beck, C.: 2018, Thermodynamic Properties of the Inverse Evershed Flow at its Downflow Points. *Astrophys. J.* **859**, 139. doi:10.3847/1538-4357/aabf36.

Cliver, E.W., White, S.M., Richardson, I.G.: 2024, A Floor in the Sun's Photospheric Magnetic Field: Implications for an Independent Small-scale Dynamo. *Astrophys. J. Lett.* **961**, L46. doi:10.3847/2041-8213/ad192e.

Collados, M.: 1999, High Resolution Spectropolarimetry and Magnetography. In: Schmieder, B., Hofmann, A., Staude, J. (eds.) *Third Advances in Solar Physics Euroconference: Magnetic Fields and Oscillations*, *ASP Conf. Ser.* **184**, 3.

Collados, M., López, R., Páez, E., Hernández, E., Reyes, M., Calcines, A., *et al.*: 2012, GRIS: The GREGOR Infrared Spectrograph. *Astron. Nachr.* **333**, 872. doi:10.1002/asna.201211738.

David, K.H.: 1961, Die Mitte-Rand Variation der Balmerlinien H$\alpha$–H$\delta$ auf der Sonnenscheibe. *Z. Astrophys.* **53**, 37.

de Boer, C.R.: 1993, Speckle-Interferometrie und ihre Anwendungen auf die Sonnenbeobachtung. PhD Thesis, Georg-August Universität Göttingen.

de Boer, C.R., Kneer, F.: 1992, Speckle Observations of Abnormal Solar Granulation. *Astron. Astrophys.* **264**, L24.

de la Cruz Rodríguez, J., Leenaarts, J., Danilovic, S., Uitenbroek, H.: 2019, STiC: A Multiatom Non-LTE PRD Inversion Code for Full-Stokes Solar Observations. *Astron. Astrophys.* **623**, A74. doi:10.1051/0004-6361/201834464.

Deng, H., Zhang, D., Wang, T., Ji, K., Wang, F., Liu, Z., *et al.*: 2015, Objective Image-quality Assessment for High-resolution Photospheric Images by Median Filter-Gradient Similarity. *Solar Phys.* **290**, 1479. doi:10.1007/s11207-015-0676-1.

Deng, N., Liu, C., Yang, G., Wang, H., Denker, C.: 2005, Rapid Penumbral Decay Associated with an X2.3 Flare in NOAA Active Region 9026. *Astrophys. J.* **623**, 1195. doi:10.1086/428821.

Deng, N., Choudhary, D.P., Tritschler, A., Denker, C., Liu, C., Wang, H.: 2007, Flow Field Evolution of a Decaying Sunspot. *Astrophys. J.* **671**, 1013. doi:10.1086/523102.

Denker, C.: 1998, Speckle Masking Imaging of Sunspots and Pores. *Solar Phys.* **180**, 81.

Denker, C.: 2010, Instrument and Data Analysis Challenges for Imaging Spectropolarimetry. *Astron. Nachr.* **331**, 648. doi:10.1002/asna.201011393.

Denker, C., Verma, M.: 2019, Background-subtracted Solar Activity Maps. *Solar Phys.* **294**, 71. doi:10.1007/s11207-019-1459-x.

Denker, C., Mascarinas, D., Xu, Y., Cao, W., Yang, G., Wang, H., *et al.*: 2005, High-spatial-resolution Imaging Combining High-order Adaptive Optics, Frame Selection, and Speckle Masking Reconstruction. *Solar Phys.* **227**, 217. doi:10.1007/s11207-005-1108-4.

Denker, C., Deng, N., Rimmele, T.R., Tritschler, A., Verdoni, A.: 2007, Field-dependent Adaptive Optics Correction Derived with the Spectral Ratio Technique. *Solar Phys.* **241**, 411. doi:10.1007/s11207-007-0315-6.

Denker, C., Kuckein, C., Verma, M., González Manrique, S.J., Diercke, A., Enke, H., *et al.*: 2018a, Data Analysis and Management for High-resolution Solar Physics – Image Restoration and Imaging Spectroscopy at the GREGOR Solar Telescope. *Astrophys. J. Suppl. Ser.* **236**. doi:10.3847/1538-4365/aab773.

Denker, C., Kuckein, C., Verma, M., González Manrique, S.J., Diercke, A., Enke, H., *et al.*: 2018b, High-cadence Imaging and Imaging Spectroscopy at the GREGOR Solar Telescope—A Collaborative Research Environment for High-resolution Solar Physics. *Astrophys. J. Suppl. Ser.* **236**, 5. doi:10.3847/1538-4365/aab773.

Denker, C., Dineva, E., Balthasar, H., *et al.*: 2018c, Image Quality in High-resolution and High-cadence Solar Images. *Solar Phys.* **5**, 236. doi:10.3847/1538-4365/aab773.

Denker, C., Verma, M., Wiśniewska, A., Kamlah, R., Kontogiannis, I., Dineva, E., *et al.*: 2023a, Improved High-resolution Fast Imager. *J. Astron. Telesc. Inst. Syst.* **9**, 015001. doi:10.1117/1.JATIS.9.1.015001.

Denker, C., Verma, M., Pietrow, A.G.M., Kontogiannis, I., Kamlah, R.: 2023b, Spectral Background-subtracted Activity Maps. *Res. Not. Amer. Astron. Soc.* **7**, 224. doi:10.3847/2515-5172/ad04e0.

Dineva, E., Verma, M., González Manrique, S.J., Schwartz, P., Denker, C.: 2020, Cloud Model Inversions of Strong Chromospheric Absorption Lines Using Principle Component Analysis. *Astron. Nachr.* **341**, 64. doi:10.1002/asna.202013652.

Doerr, H.P., Steinmetz, T., Holzwarth, R., Kentischer, T., Schmidt, W.: 2012, A Laser Frequency Comb System for Absolute Calibration of the VTT Echelle Spectrograph. *Solar Phys.* **280**, 663. doi:10.1007/s11207-012-9960-5.

Dominguez-Tagle, C., Collados, M., Lopez, R., Cedillo, J.J.V., Esteves, M.A., Grassin, O., *et al.*: 2022, First Light of the Integral Field Unit of GRIS on the GREGOR Solar Telescope. *J. Astron. Telesc. Inst. Syst.* **11**, 2250014. doi:10.1142/S2251171722500143.

D'Silva, S., Howard, R.F.: 1994, Sunspot Rotation and the Field Strengths of Subsurface Flux Tubes. *Solar Phys.* **151**, 213. doi:10.1007/BF00679072.

Evershed, J.: 1909, Radial Movement in Sunspots. *Mon. Not. R. Astron. Soc.* **69**, 454. doi:10.1093/mnras/69.5.454.

Felipe, T., Collados, M., Khomenko, E., Kuckein, C., Asensio Ramos, A., Balthasar, H., *et al.*: 2016, Three-dimensional Structure of a Sunspot Light Bridge. *Astron. Astrophys.* **596**, A59. doi:10.1051/0004-6361/201629586.

Franz, M., Schlichenmaier, R.: 2010, Center to Limb Variation of Penumbral Stokes V Profiles. *Astron. Nachr.* **331**, 570. doi:10.1002/asna.201011374.

Frazier, E.N., Stenflo, J.O.: 1978, Magnetic, Velocity and Brightness Structure of Solar Faculae. *Astron. Astrophys.* **70**, 789.

Freij, N., Scullion, E.M., Nelson, C.J., Mumford, S., Wedemeyer, S., Erdélyi, R.: 2014, The Detection of Upwardly Propagating Waves Channeling Energy from the Chromosphere to the Low Corona. *Astrophys. J.* **791**, 61. doi:10.1088/0004-637X/791/1/61.

Fried, D.L.: 1966, Optical Resolution through a Randomly Inhomogeneous Medium for Very Long and Very Short Exposures. *J. Opt. Soc. Am. A* **56**, 1372. doi:10.1364/JOSA.56.001372.

Fried, D.L., Mevers, G.E.: 1974, Evaluation of $r_0$ for Propagation Down through the Atmosphere. *Appl. Opt.* **13**, 2620. doi:10.1364/AO.13.002620.

Gallagher, P.T., Moon, Y.J., Wang, H.: 2002, Active-region Monitoring and Flare Forecasting I. Data Processing and First Results. *Solar Phys.* **209**, 171. doi:10.1023/A:1020950221179.

Georgakilas, A.A., Christopoulou, E.B.: 2003, Temporal Behavior of the Evershed Effect. *Astrophys. J.* **584**, 509. doi:10.1086/345550.

Giovanelli, R.G.: 1972, Oscillations and Waves in a Sunspot. *Solar Phys.* **27**, 71. doi:10.1007/BF00151771.

González Manrique, S.J., Kuckein, C., Collados, M., Denker, C., Solanki, S.K., Gömöry, P., *et al.*: 2018, Temporal Evolution of Arch Filaments as seen in He I 10 830 Å. *Astron. Astrophys.* **617**, A55. doi:10.1051/0004-6361/201832684.

Guglielmino, S.L., Zuccarello, F.: 2011, High-resolution Observations of Siphon Flows in a Solar Magnetic Pore. *Astrophys. J. Lett.* **743**, L9. doi:10.1088/2041-8205/743/1/L9.

Hagenaar, H.J., Shine, R.A.: 2005, Moving Magnetic Features Around Sunspots. *Astrophys. J.* **635**, 659. doi:10.1086/497367.

Hale, G.E.: 1908, On the Probable Existence of a Magnetic Field in Sun-spots. *Astrophys. J.* **28**, 315. doi:10.1086/141602.

Hale, G.E.: 1925, Nature of the Hydrogen Vortices Surrounding Sun-spots. *Publ. Astron. Soc. Pac.* **37**, 268. doi:10.1086/123497.

Hale, G.E.: 1927, The Fields of Force in the Atmosphere of the Sun. *Nature* **119**, 708. doi:10.1038/119708a0.

Hale, G.E., Ellerman, F., Nicholson, S.B., Joy, A.H.: 1919, The Magnetic Polarity of Sun-spots. *Astrophys. J.* **49**, 153. doi:10.1086/142452.

Hammerschlag, R.H., Kommers, J.N., Visser, S., Bettonvil, F.C.M., van Schie, A.G.M., van Leverink, S.J., *et al.*: 2012, Open-foldable Domes with High-tension Textile Membranes: The GREGOR Dome. *Astron. Nachr.* **333**, 830. doi:10.1002/asna.201211731.

Hanisch, R.J., Farris, A., Greisen, E.W., Pence, W.D., Schlesinger, B.M., Teuben, P.J., *et al.*: 2001, Definition of the Flexible Image Transport System (FITS). *Astron. Astrophys.* **376**, 359. doi:10.1051/0004-6361:20010923.

Harvey, K., Harvey, J.: 1973, Observations of Moving Magnetic Features near Sunspots. *Solar Phys.* **28**, 61. doi:10.1007/bf00152912.

Hathaway, D.H.: 2010, The Solar Cycle. *Living Rev. Solar Phys.* **7**, 1. doi:10.12942/lrsp-2010-1.

Haugen, E.: 1969, On the Chromospheric Velocity Field in Sunspot Regions. *Solar Phys.* **9**, 88. doi:10.1007/BF00145731.

Helmli, F.S., Scherer, S.: 2001, Adaptive Shape from Focus with an Error Estimation in Light Microscopy. In: Lončarić, S., Babić, H. (eds.) *Proceedings of the 2nd International Symposium on Image and Signal Processing and Analysis. In Conjunction with 23rd International Conference on Information Technology Interfaces*, *IEEE Cat. No.01EX480*, 188. doi:10.1109/ISPA.2001.938626.

Hirzberger, J.: 2003, Imaging Spectroscopy of Solar Pores. *Astron. Astrophys.* **405**, 331. doi:10.1051/0004-6361:20030595.

Hirzberger, J., Stangl, S., Gersin, K., Jurčák, J., Puschmann, K.G., Sobotka, M.: 2005, The Structure of a Penumbral Connection between Solar Pores. *Astron. Astrophys.* **442**, 1079. doi:10.1051/0004-6361:20053257.

Hou, Y.J., Li, T., Zhong, S.H., Yang, S.H., Guo, Y.L., Li, X.H., *et al.*: 2020, Sunspot Penumbral Filaments Intruding into a Light Bridge and the Resultant Reconnection Jets. *Astron. Astrophys.* **642**, A44. doi:10.1051/0004-6361/202038668.

Howard, R.F.: 1990, The Magnetic Fields of Active Regions. II. Rotation. *Solar Phys.* **126**, 299.

Iijima, H., Yokoyama, T.: 2017, A Three-dimensional Magnetohydrodynamic Simulation of the Formation of Solar Chromospheric Jets with Twisted Magnetic Field Lines. *Astrophys. J.* **848**, 38. doi:10.3847/1538-4357/aa8ad1.

Jahn, K., Schmidt, H.U.: 1994, Thick Penumbra in a Magnetostatic Sunspot Model. *Astron. Astrophys.* **290**, 295.

Jess, D.B., Reznikova, V.E., Van Doorsselaere, T., Keys, P.H., Mackay, D.H.: 2013, The Influence of the Magnetic Field on Running Penumbral Waves in the Solar Chromosphere. *Astrophys. J.* **779**, 168. doi:10.1088/0004-637X/779/2/168.

Jing, J., Li, Q., Liu, C., Lee, J., Xu, Y., Cao, W., Wang, H.: 2019, High-resolution Observations of Dynamics of Superpenumbral H$\alpha$ Fibrils. *Astrophys. J.* **880**, 143. doi:10.3847/1538-4357/ab2b44.

Jing, J., Liu, N., Lee, J., Xu, Y., Cao, W., Wang, H.: 2023, Characterizing 3D Magnetic Structures in Sunspot Light Bridges. *Astrophys. J.* **952**, 40. doi:10.3847/1538-4357/acd44f.

Joshi, J., Lagg, A., Hirzberger, J., Solanki, S.K., Tiwari, S.K.: 2017, Vertical Magnetic Field Gradient in the Photospheric Layers of Sunspots. *Astron. Astrophys.* **599**, A35. doi:10.1051/0004-6361/201527060.

Jurčák, J., Martínez Pillet, V., Sobotka, M.: 2006, The Magnetic Canopy above Light Bridges. *Astron. Astrophys.* **453**, 1079. doi:10.1051/0004-6361:20054471.

Kamlah, R., Verma, M., Diercke, A., Denker, C.: 2021, Wavelength Dependence of Image Quality Metrics and Seeing Parameters and Their Relation to Adaptive Optics Performance. *Solar Phys.* **296**, 29. doi:10.1007/s11207-021-01771-y.

Kamlah, R., Verma, M., Denker, C., Wang, H.: 2023, High-resolution Imaging of Solar Pores. *Astron. Astrophys.* **675**, A182. doi:10.1051/0004-6361/202245410.

Kamlah, R., Verma, M., Denker, C., Huang, N., Lee, J., Wang, H.: 2024, Impact of Magnetic and Flow Fields on Penumbrae and Light Bridges of Three Leading Sunspots in an Active Region. *Solar Phys.* **299**, 144. doi:10.1007/s11207-024-02386-9.

Katsukawa, Y., Yokoyama, T., Berger, T.E., Ichimoto, K., Kubo, M., Lites, B., *et al.*: 2007, Formation Process of a Light Bridge Revealed with the Hinode Solar Optical Telescope. *Publ. Astron. Soc. Japan* **59**, S577. doi:10.1093/pasj/59.sp3.S577.

Keil, S.L., Balasubramaniam, K.S., Smaldone, L.A., Reger, B.: 1999, Velocities in Solar Pores. *Astrophys. J.* **510**, 422. doi:10.1086/306549.

Khomenko, E., Collados, M.: 2015, Oscillations and Waves in Sunspots. *Living Rev. Solar Phys.* **12**, 6. doi:10.1007/lrsp-2015-6.

Kilpua, E.K.J., Balogh, A., von Steiger, R., Liu, Y.D.: 2017, Geoeffective Properties of Solar Transients and Stream Interaction Regions. *Space Sci. Rev.* **212**, 1271. doi:10.1007/s11214-017-0411-3.

Kitiashvili, I.N., Kosovichev, A.G., Wray, A.A., Mansour, N.N.: 2009, Traveling Waves of Magnetoconvection and the Origin of the Evershed Effect in Sunspots. *Astrophys. J. Lett.* **700**, L178. doi:10.1088/0004-637X/700/2/L178.

Kleint, L., Berkefeld, T., Esteves, M., Sonner, T., Volkmer, R., Gerber, K., *et al.*: 2020, GREGOR: Optics Redesign and Updates from 2018 – 2020. *Astron. Astrophys.* **641**, A27. doi:10.1051/0004-6361/202038208.

Kontogiannis, I., Dineva, E., Diercke, A., Verma, M., Kuckein, C., Balthasar, H., Denker, C.: 2020, High-resolution Spectroscopy of an Erupting Minifilament and its Impact on the Nearby Chromosphere. *Astrophys. J.* **898**, 144. doi:10.3847/1538-4357/aba117.

Korff, D.: 1973, Analysis of a Method for Obtaining Near-diffraction-limited Information in the Presence of Atmospheric Turbulence. *J. Opt. Soc. Am. A* **63**, 971. doi:10.1364/josa.63.000971.

Koutchmy, S., Adjabshirzadeh, A.: 1981, Photometric Analysis of the Sunspot Umbral Dots – Part Two – Size Shape and Temperature. *Astron. Astrophys.* **99**, 111.

Kuckein, C., Denker, C., Verma, M., Balthasar, H., González Manrique, S.J., Louis, R.E., Diercke, A.: 2017, sTools – a Data Reduction Pipeline for the GREGOR Fabry-Pérot Interferometer and the High-resolution Fast Imager at the GREGOR Solar Telescope. In: Vargas Domínguez, S., Kosovichev, A.G., Harra, L., Antolin, P. (eds.) *Fine Structure and Dynamics of the Solar Atmosphere*, *IAU Symp.* **327**, 20. doi:10.1017/S1743921317000114.

Kuckein, C., Denker, C., Verma, M., Balthasar, H., Diercke, A., González Manrique, S.J., et al.: 2018, sTools – A Software Package for Data Reduction of GREGOR Instruments and General Data Analysis. In: *Catalyzing Solar Connections*, 105.

Künzel, H.: 1969, Über den Zusammenhang zwischen Penumbraformen und magnetischer Polaritätsverteilung in Sonnenfleckengruppen. *Astron. Nachr.* **291**, 265.

Kutsenko, A.S., Abramenko, V.I., Litvishko, D.V.: 2023, The Rotation Rate of Solar Active and Ephemeral Regions. II. Temporal Variations of the Rotation Rates. *Mon. Not. R. Astron. Soc.* **519**, 5315. doi:10.1093/mnras/stac3826.

Lagg, A., Solanki, S.K., van Noort, M., Danilovic, S.: 2014, Vigorous Convection in a Sunspot Granular Light Bridge. *Astron. Astrophys.* **568**, A60. doi:10.1051/0004-6361/201424071.

Langhans, K., Scharmer, G.B., Kiselman, D., Löfdahl, M.G., Berger, T.E.: 2005, Inclination of Magnetic Fields and Flows in Sunspot Penumbrae. *Astron. Astrophys.* **436**, 1087. doi:10.1051/0004-6361:20052678.

LaVision: 2021a, *Product Manual for DaVis 10.2 Software*. LaVision GmbH, Göttingen, Germany.

LaVision: 2021b, *Product Manual for Imager MX CXP*. LaVision GmbH, Göttingen, Germany.

Lee, J.S.: 1986, Speckle Suppression and Analysis for Synthetic Aperture Radar Images. *Opt. Eng.* **25**, 636. doi:10.1117/12.7973877.

Leenaarts, J., Carlsson, M., Rouppe van der Voort, L.: 2012, The Formation of the H$\alpha$ Line in the Solar Chromosphere. *Astrophys. J.* **749**, 136. doi:10.1088/0004-637X/749/2/136.

Lefèvre, L., Clette, F.: 2011, A Global Small Sunspot Deficit at the Base of the Index Anomalies of Solar Cycle 23. *Astron. Astrophys.* **536**, L11. doi:10.1051/0004-6361/201118034.

Leka, K.D., Skumanich, A.: 1998, The Evolution of Pores and the Development of Penumbrae. *Astrophys. J.* **507**, 454. doi:10.1086/306297.

Leka, K.D., Steiner, O.: 2001, Understanding Small Solar Magnetic Structures: Comparing Numerical Simulations to Observations. *Astrophys. J.* **552**, 354. doi:10.1086/320445.

Lemen, J.R., Title, A.M., Akin, D.J., Boerner, P.F., Chou, C., Drake, J.F., *et al.*: 2012, The Atmospheric Imaging Assembly (AIA) on the Solar Dynamics Observatory (SDO). *Solar Phys.* **275**, 17.

Li, F.Y., Chen, Y.H., Song, Y.L., Hou, Z.Y., Tian, H.: 2021, Statistical Investigation on the Formation of Sunspot Light Bridges. *Res. Astron. Astrophys.* **21**, 144. doi:10.1088/1674-4527/21/6/144.

Lim, E.K., Yurchyshyn, V., Goode, P., Cho, K.S.: 2013, Observation of a Non-radial Penumbra in a Flux Emerging Region under Chromospheric Canopy Fields. *Astrophys. J. Lett.* **769**, L18. doi:10.1088/2041-8205/769/1/L18.

Lindner, P., Kuckein, C., González Manrique, S.J., Bello González, N., Kleint, L., Berkefeld, T.: 2023, The Role of the Chromospheric Magnetic Canopy in the Formation of a Sunspot Penumbra. *Astron. Astrophys.* **673**, A64. doi:10.1051/0004-6361/202245702.

Lites, B.W., Bida, T.A., Johannesson, A., Scharmer, G.B.: 1991, High-resolution Spectra of Solar Magnetic Features. II. Magnetic Fields of Umbral Brightenings. *Astrophys. J.* **373**, 683. doi:10.1086/170089.

Liu, S., Liu, D.: 2015, Fine Magnetic Characteristics of a Light Bridge Observed by Hinode. *Adv. Space Res.* **55**, 2931. doi:10.1016/j.asr.2015.02.034.

Livingston, W.: 2002, Sunspots Observed to Physically Weaken in 2000 – 2001. *Solar Phys.* **207**, 41. doi:10.1023/A:1015555000456.

Löfdahl, M.G.: 2002, Multi-frame Blind Deconvolution with Linear Equality Constraints. In: Bones, P.J., Fiddy, M.A., Millane, R.P. (eds.) *Image Reconstruction from Incomplete Data*, *Proc. SPIE* **4792**, 146. doi:10.1117/12.451791.

Löfdahl, M.G., Hillberg, T., de la Cruz Rodríguez, J., Vissers, G., Andriienko, O., Scharmer, G.B., Haugan, S.V., Fredvik, T.: 2021, SSTRED: Data- and Metadata-processing Pipeline for CHROMIS and CRISP. *Astron. Astrophys.* **653**, A68. doi:10.1051/0004-6361/202141326.

Lohmann, A.W., Weigelt, G., Wirnitzer, B.: 1983, Speckle Masking in Astronomy – Triple Correlation Theory and Applications. *Appl. Opt.* **22**, 4028. doi:10.1364/AO.22.004028.

Löhner-Böttcher, J., Schlichenmaier, R.: 2013, Correlations between Sunspots and their Moat Flows. *Astron. Astrophys.* **551**, A105. doi:10.1051/0004-6361/201220543.

Löhner-Böttcher, J., Schmidt, W., Doerr, H.P., Kentischer, T., Steinmetz, T., Probst, R.A., Holzwarth, R.: 2017, LARS: An Absolute Reference Spectrograph for Solar Observations. Upgrade from a Prototype to a Turn-key System. *Astron. Astrophys.* **607**, A12. doi:10.1051/0004-6361/201731164.

Lomb, N.R.: 1976, Least-squares Frequency Analysis of Unequally Spaced Data. *Astrophys. Space Sci.* **39**, 447 – 462. doi:10.1007/BF00648343.

Loughhead, R.E.: 1968, High-resolution Photography of the Solar Chromosphere. *Solar Phys.* **5**, 489. doi:10.1007/BF00147015.

Louis, R.E.: 2015, Small-scale Magnetic and Velocity Inhomogeneities in a Sunspot Light Bridge. *Adv. Space Res.* **56**, 2305. doi:10.1016/j.asr.2015.09.003.

Louis, R.E., Bayanna, A.R., Mathew, S.K., Venkatakrishnan, P.: 2008, Dynamics of Sunspot Light Bridges as Revealed by High-resolution Images from Hinode. *Solar Phys.* **252**, 43. doi:10.1007/s11207-008-9247-z.

Louis, R.E., Bellot Rubio, L.R., Mathew, S.K., Venkatakrishnan, P.: 2009, Supersonic Downflows in a Sunspot Light Bridge. *Astrophys. J. Lett.* **704**, L29. doi:10.1088/0004-637X/704/1/L29.

Márquez, I., Sánchez Almeida, J., Bonet, J.A.: 2006, High-resolution Proper Motions in a Sunspot Penumbra. *Astrophys. J.* **638**, 553. doi:10.1086/498668.

McIntosh, P.S.: 1990, The Classification of Sunspot Groups. *Solar Phys.* **125**, 251. doi:10.1007/BF00158405.

Meyer, F., Schmidt, H.U.: 1968, Magnetisch Ausgerichtete Strömungen Zwischen Sonnenflecken. *Zeitschrift Angewandte Mathematik und Mechanik* **48**, 218.

Mikurda, K., von der Lühe, O.: 2006, High Resolution Solar Speckle Imaging with the Extended Knox-Thompson Algorithm. *Solar Phys.* **235**, 31. doi:10.1007/s11207-006-0069-6.

Molowny-Horas, R.: 1994, Proper Motion Measurements of Umbral and Penumbral Structure. *Solar Phys.* **154**, 29. doi:10.1007/bf00676775.

Moore, R., Rabin, D.: 1985, Sunspots. *Ann. Rev. Astron. Astrophys.* **23**, 239. doi:10.1146/annurev.aa.23.090185.001323.

Moore, R.L., Tang, F., Bohlin, J.D., Golub, L.: 1977, H$\alpha$ Macrospicules – Identification with EUV Macrospicules and with Flares in X-Ray Bright Points. *Astrophys. J.* **218**, 286.

Mulay, S.M., Tripathi, D., Del Zanna, G., Mason, H.: 2016, Multiwavelength Study of 20 Jets that Emanate from the Periphery of Active Regions. *Astron. Astrophys.* **589**, A79. doi:10.1051/0004-6361/201527473.

Muller, R., Mena, B.: 1987, Motions around a Decaying Sunspot. *Solar Phys.* **112**, 295 – 303. doi:10.1007/BF00148783.

Murabito, M., Romano, P., Guglielmino, S.L., Zuccarello, F., Solanki, S.K.: 2016, Formation of the Penumbra and Start of the Evershed Flow. *Astrophys. J.* **825**, 75. doi:10.3847/0004-637X/825/1/75.

Murabito, M., Romano, P., Guglielmino, S.L., Zuccarello, F.: 2017, On the Formation of a Stable Penumbra in a Region of Flux Emergence in the Sun. *Astrophys. J.* **834**, 76. doi:10.3847/1538-4357/834/1/76.

Murabito, M., Zuccarello, F., Guglielmino, S.L., Romano, P.: 2018, Formation of Penumbra in a Sample of Active Regions Observed by the SDO Satellite. *Astrophys. J.* **855**, 58. doi:10.3847/1538-4357/aaac7c.

Murabito, M., Guglielmino, S.L., Ermolli, I., Romano, P., Jafarzadeh, S., Rouppe van der Voort, L.H.M.: 2021, Penumbral Decay Observed in Active Region NOAA 12585. *Astron. Astrophys.* **653**, A93. doi:10.1051/0004-6361/202141034.

Neckel, H.: 1999, Announcement – Spectral Atlas of Solar Absolute Disk-averaged and Disk-center Intensity from 3290 to 12510 Å Now Available from Hamburg Observatory Anonymous FTP Site. *Solar Phys.* **184**, 421. doi:10.1023/A:1017165208013.

Neckel, H., Labs, D.: 1984, The Solar Radiation Between 3300 and 12500 A. *Solar Phys.* **90**, 205. doi:10.1007/BF00173953.

Nordlund, Å., Stein, R.F., Asplund, M.: 2009, Solar Surface Convection. *Living Rev. Solar Phys.* **6**, 1. doi:10.12942/lrsp-2009-2.

November, L.J., Simon, G.W.: 1988, Precise Proper-Motion Measurement of Solar Granulation. *Astrophys. J.* **333**, 427. doi:10.1086/166758.

Panja, M., Cameron, R.H., Solanki, S.K.: 2021, Sunspot Simulations: Penumbra Formation and the Fluting Instability. *Astrophys. J.* **907**, 102. doi:10.3847/1538-4357/abccbf.

Parker, E.N.: 1955, The Formation of Sunspots from the Solar Toroidal Field. *Astrophys. J.* **121**, 491. doi:10.1086/146010.

Pence, W.D., Chiappetti, L., Page, C.G., Shaw, R.A., Stobie, E.: 2010, Definition of the Flexible Image Transport System (FITS), Version 3.0. *Astron. Astrophys.* **524**, A42. doi:10.1051/0004-6361/201015362.

Pesnell, W.D., Thompson, B.J., Chamberlin, P.C.: 2012, The Solar Dynamics Observatory (SDO). *Solar Phys.* **275**, 3. doi:10.1007/978-3-319-03952-7_16.

Peter, H.: 1996, Superpenumbral Vortices. *Mon. Not. R. Astron. Soc.* **278**, 821. doi:10.1093/mnras/278.3.821.

Pierce, A.K., Slaughter, C.D., Weinberger, D.: 1977, Solar Limb Darkening. II. In the Interval 7404 – 24018 Å. *Solar Phys.* **52**, 179.

Pietrow, A.G.M., Druett, M.K., de la Cruz Rodriguez, J., Calvo, F., Kiselman, D.: 2022, Physical Properties of a Fan-shaped Jet Backlit by an X9.3 Flare. *Astron. Astrophys.* **659**, A58. doi:10.1051/0004-6361/202142346.

Ponz, J.D., Thompson, R.W., Munoz, J.R.: 1994, The FITS Image Extension. *Astron. Astrophys. Suppl. Ser.* **105**, 53.

Popowicz, A., Radlak, K., Bernacki, K., Orlov, V.: 2017, Review of Image Quality Measures for Solar Imaging. *Solar Phys.* **292**, 187. doi:10.1007/s11207-017-1211-3.

Press, W.H., Flannery, B.P., Teukolsky, S.A.: 1986, *Numerical Recipes. The Art of Scientific Computing*, Cambridge University Press, New York. doi:10.2307/1269484.

Press, W.H., Teukolsky, S.A., Vetterling, W.T., Flannery, B.P.: 1992, *Numerical Recipes in C. The Art of Scientific Computing*, Cambridge University Press, New York.

Pruthvi, H., Roth, M.: 2023, The New HELLRIDE at the Vacuum Tower Telescope. *Solar Phys.* **298**, 41. doi:10.1007/s11207-023-02138-1.

Puschmann, K.G., Beck, C.: 2011, Application of Speckle and (Multi-object) Multi-frame Blind Deconvolution Techniques on Imaging and Imaging Spectropolarimetric Data. *Astron. Astrophys.* **533**, A21. doi:10.1051/0004-6361/201116904.

Puschmann, K.G., Sailer, M.: 2006, Speckle Reconstruction of Photometric Data Observed with Adaptive Optics. *Astron. Astrophys.* **454**, 1011. doi:10.1051/0004-6361:20053918.

Quintero Noda, C., Shimizu, T., Ruiz Cobo, B., Suematsu, Y., Katsukawa, Y., Ichimoto, K.: 2016, Analysis of a Spatially Deconvolved Solar Pore. *Mon. Not. R. Astron. Soc.* **460**, 1476. doi:10.1093/mnras/stw1068.

Quintero Noda, C., Schlichenmaier, R., Bellot Rubio, L.R., Löfdahl, M.G., Khomenko, E., Jurčák, J., *et al.*: 2022a, The European Solar Telescope. *Astron. Astrophys.* **666**, A21. doi:10.1051/0004-6361/202243867.

Quintero Noda, C., Collados, M., Regalado Olivares, S., González, F., Quintero Nehrkorn, J., Rodríguez Delgado, H., et al.: 2022b, The Upgraded GREGOR Infrared Spectrograph. In: Evans, C.J., Bryant, J.J., Motohara, K. (eds.) *Ground-based and Airborne Instrumentation for Astronomy IX*, *Proc. SPIE* **12184**, 121840U. doi:10.1117/12.2628721.

Regalado Olivares, S., López López, R., González, F., Collados, M., Dominguez-Tagle, C., Mato Martínez, Á., et al.: 2022, Optical and Mechanical Updates in the GREGOR Infrared Spectrograph for Simultaneous Spectral oObservations. In: Navarro, R., Geyl, R. (eds.) *Advances in Optical and Mechanical Technologies for Telescopes and Instrumentation V*, *Proc. SPIE* **12188**, 121885B. doi:10.1117/12.2628928.

Rempel, M.: 2011, 3D numerical MHD Modeling of Sunspots with Radiation Transport. In: P. Choudhary, D., Strassmeier, K.G. (eds.) *Physics of Sun and Star Spots*, *IAU Symp.* **273**, 8. doi:10.1017/S1743921311014931.

Rempel, M.: 2015, Numerical Simulations of Sunspot Decay: On the Penumbra – Evershed Flow – Moat Flow Connection. *Astrophys. J.* **814**, 125. doi:10.1088/0004-637X/814/2/125.

Rempel, M., Cheung, M.C.M.: 2014, Numerical Simulations of Active Region Scale Flux Emergence: From Spot Formation to Decay. *Astrophys. J.* **785**, 90. doi:10.1088/0004-637x/785/2/90.

Rempel, M., Schlichenmaier, R.: 2011, Sunspot Modeling: From Simplified Models to Radiative MHD Simulations. *Living Rev. Solar Phys.* **8**, 3. doi:10.12942/lrsp-2011-3.

Rempel, M., Schüssler, M., Knölker, M.: 2009a, Radiative Magnetohydrodynamic Simulation of Sunspot Structure. *Astrophys. J.* **691**, 640. doi:10.1088/0004-637X/691/1/640.

Rempel, M., Schüssler, M., Cameron, R.H., Knölker, M.: 2009b, Penumbral Structure and Outflows in Simulated Sunspots. *Science* **325**, 171. doi:10.1126/science.1173798.

Rezaei, R., Bello González, N., Schlichenmaier, R.: 2012, The Formation of Sunspot Penumbra. Magnetic Field Properties. *Astron. Astrophys.* **537**, A19. doi:10.1051/0004-6361/201117485.

Richardson, R.S.: 1941, The Nature of Solar Hydrogen Vortices. *Astrophys. J.* **93**, 24. doi:10.1086/144238.

Richardson, R.S., Schwarzschild, M.: 1950, On the Turbulent Velocities of Solar Granules. *Astrophys. J.* **111**, 351. doi:10.1086/145269.

Riethmüller, T.L., Solanki, S.K., Zakharov, V., Gandorfer, A.: 2008, Brightness, Distribution, and Evolution of Sunspot Umbral Dots. *Astron. Astrophys.* **492**, 233. doi:10.1051/0004-6361:200810701.

Rimmele, T.: 2008, On the Relation between Umbral Dots, Dark-cored Filaments, and Light Bridges. *Astrophys. J.* **672**, 684. doi:10.1086/523702.

Rimmele, T.R.: 1995, Evidence for Thin Elevated Evershed Channels. *Astron. Astrophys.* **298**, 260.

Rimmele, T.R., Warner, M., Keil, S.L., Goode, P.R., Knölker, M., *et al.*: 2020, The Daniel K. Inouye Solar Telescope – Observatory Overview. *Solar Phys.* **295**, 172. doi:10.1007/s11207-020-01736-7.

Robustini, C., Leenaarts, J., de la Cruz Rodriguez, J., Rouppe van der Voort, L.: 2016, Fan-shaped Jets above the Light Bridge of a Sunspot Driven by Reconnection. *Astron. Astrophys.* **590**, A57. doi:10.1051/0004-6361/201528022.

Romano, P., Frasca, D., Guglielmino, S.L., Ermolli, I., Tritschler, A., Reardon, K.P., Zuccarello, F.: 2013, Velocity and Magnetic Field Distribution in a Forming Penumbra. *Astrophys. J. Lett.* **771**, L3. doi:10.1088/2041-8205/771/1/l3.

Romano, P., Guglielmino, S.L., Cristaldi, A., Ermolli, I., Falco, M., Zuccarello, F.: 2014, Evolution of the Magnetic Field Inclination in a Forming Penumbra. *Astrophys. J.* **784**, 10. doi:10.1088/0004-637X/784/1/10.

Romano, P., Murabito, M., Guglielmino, S.L., Zuccarello, F., Falco, M.: 2020, Restoring Process of Sunspot Penumbra. *Astrophys. J.* **899**, 129. doi:10.3847/1538-4357/aba18b.

Roudier, T., Bonet, J.A., Sobotka, M.: 2002, Properties of Horizontal Flows Inside and Outside a Solar Pore. *Astron. Astrophys.* **395**, 249. doi:10.1051/0004-6361:20021259.

Rouppe van der Voort, L., Bellot Rubio, L.R., Ortiz, A.: 2010, Upflows in the Central Dark Lane of Sunspot Light Bridges. *Astrophys. J. Lett.* **718**, L78. doi:10.1088/2041-8205/718/2/L78.

Roy, J.R.: 1973, The Magnetic Properties of Solar Surges. *Solar Phys.* **28**, 95. doi:10.1007/BF00152915.

Rucklidge, A.M., Schmidt, H.U., Weiss, N.O.: 1995, The Abrupt Development of Penumbrae in Sunspots. *Mon. Not. R. Astron. Soc.* **273**, 491. doi:10.1093/mnras/273.2.491.

Ruiz Cobo, B., del Toro Iniesta, J.C.: 1992, Inversion of Stokes Profiles. *Astrophys. J.* **398**, 375. doi:10.1086/171862.

Sainz Dalda, A., Bellot Rubio, L.R.: 2008, Detection of Sea-serpent Field Lines in Sunspot Penumbrae. *Astron. Astrophys.* **481**, L21. doi:10.1051/0004-6361:20079115.

Sánchez Almeida, J., Asensio Ramos, A., Trujillo Bueno, J., Cernicharo, J.: 2001, G-band Spectral Synthesis in Solar Magnetic Concentrations. *Astrophys. J.* **555**, 978. doi:10.1086/321521.

Sankarasubramanian, K., Rimmele, T.: 2003, Properties of Magnetic and Velocity Fields in and around Solar Pores. *Astrophys. J.* **598**, 689. doi:10.1086/378883.

Scargle, J.D.: 1982, Studies in Astronomical Time Series Analysis. II. Statistical Aspects of Spectral Analysis of Unevenly Spaced Data. *Astrophys. J.* **263**, 835. doi:10.1086/160554.

Schad, T.A., Penn, M.J., Lin, H., Tritschler, A.: 2015, He I Vector Magnetic Field Maps of a Sunspot and Its Superpenumbral Fine-Structure. *Solar Phys.* **290**, 1607. doi:10.1007/s11207-015-0706-z.

Scharmer, G.B., Gudiksen, B.V., Kiselman, D., Löfdahl, M.G., Rouppe van der Voort, L.H.M.: 2002, Dark Cores in Sunspot Penumbral Filaments. *Nature* **420**, 151. doi:10.1038/nature01173.

Scharmer, G.B., Bjelksjo, K., Korhonen, T.K., Lindberg, B., Petterson, B.: 2003, The 1-meter Swedish Solar Telescope. In: Keil, S.L., Avakyan, S.V. (eds.) *Innovative Telescopes and Instrumentation for Solar Astrophysics*, *Proc. SPIE* **4853**, 341. doi:10.1117/12.460377.

Scharmer, G.B., de la Cruz Rodriguez, J., Sütterlin, P., Henriques, V.M.J.: 2013, Opposite Polarity Field with Convective Downflow and its Relation to Magnetic Spines in a Sunspot Penumbra. *Astron. Astrophys.* **553**, A63. doi:10.1051/0004-6361/201220899.

Schatten, K.H.: 2009, Modeling a Shallow Solar Dynamo. *Solar Phys.* **255**, 3. doi:10.1007/s11207-008-9308-3.

Scherrer, P.H., Schou, J., Bush, R.I., Kosovichev, A.G., Bogart, R.S., Hoeksema, J.T., *et al.*: 2012, The Helioseismic and Magnetic Imager (HMI) Investigation for the Solar Dynamics Observatory (SDO). *Solar Phys.* **275**, 207.

Schlichenmaier, R., Schmidt, W.: 2000, Flow Geometry in a Sunspot Penumbra. *Astron. Astrophys.* **358**, 1122.

Schlichenmaier, R., Bellot Rubio, L.R., Tritschler, A.: 2004, Two-dimensional Spectroscopy of a Sunspot. II. Penumbral Line Asymmetries. *Astron. Astrophys.* **415**, 731. doi:10.1051/0004-6361:20034430.

Schlichenmaier, R., Jahn, K., Schmidt, H.U.: 1998, Magnetic Flux Tubes Evolving in Sunspots. A Model for the Penumbral Fine Structure and the Evershed Flow. *Astron. Astrophys.* **337**, 897.

Schlichenmaier, R., Rezaei, R., González, N.B.: 2012, On the Formation of Penumbrae as Observed with the German VTT SOHO/MDI, and SDO/HMI. In: Bellot Rubio, L., Reale, F., Carlsson, M. (eds.) *4th Hinode Science Meeting: Unsolved Problems and Recent Insights*, *ASP Conf. Ser.* **455**, 61.

Schlichenmaier, R., Rezaei, R., Bello González, N., Waldmann, T.A.: 2010a, The Formation of a Sunspot Penumbra. *Astron. Astrophys.* **512**, L1. doi:10.1051/0004-6361/201014112.

Schlichenmaier, R., Bello González, N., Rezaei, R., Waldmann, T.A.: 2010b, The Role of Emerging Bipoles in the Formation of a Sunspot Penumbra. *Astron. Nachr.* **331**, 563. doi:10.1002/asna.201011372.

Schmidt, W., Schlichenmaier, R.: 2000, Small-scale Flow Field in a Sunspot Penumbra. *Astron. Astrophys.* **364**, 829.

Schmidt, W., Stix, M., Wöhl, H.: 1999, Center-to-limb Variation of the Solar Oscillation. New Results from MDI Data. *Astron. Astrophys.* **346**, 633.

Schmidt, W., von der Lühe, O., Volkmer, R., Denker, C., Solanki, S.K., Balthasar, H., *et al.*: 2012, The 1.5 Meter Solar Telescope GREGOR. *Astron. Nachr.* **333**, 796. doi:10.1002/asna.201211725.

Schou, J., Scherrer, P.H., Bush, R.I., Wachter, R., Couvidat, S., Rabello-Soares, M.C., *et al.*: 2012, Design and Ground Calibration of the Helioseismic and Magnetic Imager (HMI) Instrument on the Solar Dynamics Observatory (SDO). *Solar Phys.* **275**, 229.

Schrijver, C.J., Zwaan, C.: 2000, Solar and Stellar Magnetic Activity. *Camb. Astrophys. Ser.* **34**. doi:10.1017/cbo9780511546037.

Schrijver, C.J., Hagenaar, H.J., Title, A.M.: 1997, On the Patterns of the Solar Granulation and Supergranulation. *Astrophys. J.* **475**, 328. doi:10.1086/303528.

Schröter, E.H., Soltau, D., Wiehr, E.: 1985, The German Solar Telescopes at the Observatorio del Teide. *Vistas Astron.* **28**, 519. doi:10.1016/0083-6656(85)90073-X.

Schüssler, M., Shelyag, S., Berdyugina, S., Vögler, A., Solanki, S.K.: 2003, Why Solar Magnetic Flux Concentrations are Bright in Molecular Bands. *Astrophys. J. Lett.* **597**, L173. doi:10.1086/379869.

Sheeley, J. N. R.: 1969, The Evolution of the Photospheric Network. *Solar Phys.* **9**, 347. doi:10.1007/BF02391657.

Sheeley, N.R. Jr.: 1972, Observations of the Horizontal Velocity Field Surrounding Sunspots. *Solar Phys.* **25**, 98. doi:10.1007/bf00155747.

Shimizu, T., Ichimoto, K., Suematsu, Y.: 2012, Precursor of Sunspot Penumbral Formation Discovered with Hinode Solar Optical Telescope Observations. *Astrophys. J. Lett.* **747**, L18. doi:10.1088/2041-8205/747/2/L18.

Shine, R.A., Title, A., Frank, Z., Scharmer, G.: 1996, Photospheric Surface Flows and Small Magnetic Structures in Sunspot Moats. *Astron. Astrophys. Suppl. Ser.* **28**, 871.

Shumko, S., Gorceix, N., Choi, S., Kellerer, A., Cao, W., Goode, P.R., et al.: 2014, AO-308: The High-order Adaptive Optics System at Big Bear Solar Observatory. In: Marchetti, E., Close, L.M., Véran, J.P. (eds.) *Adaptive Optics Systems IV*, *Proc. SPIE* **9148**, 1073. doi:10.1117/12.2056731.

Siu-Tapia, A.L., Rempel, M., Lagg, A., Solanki, S.K.: 2018, Evershed and Counter-Evershed Flows in Sunspot MHD Simulations. *Astrophys. J.* **852**, 66. doi:10.3847/1538-4357/aaa007.

So, C.W., Yuen, E.L.H., Leung, E.H.F., Pun, J.C.S.: 2024, Solar Image Quality Assessment: A Proof of Concept Using Variance of Laplacian Method and its Application to Optical Atmospheric Condition Monitoring. *Publ. Astron. Soc. Pac.* **136**, 044504. doi:10.1088/1538-3873/ad3b39.

Sobotka, M., Puschmann, K.G.: 2009, Morphology and Evolution of Umbral Dots and their Substructures. *Astron. Astrophys.* **504**, 575. doi:10.1051/0004-6361/200912365.

Sobotka, M., Roudier, T.: 2007, Properties of Sunspot Moats Derived from Horizontal Motions. *Astron. Astrophys.* **472**, 277. doi:10.1051/0004-6361:20077552.

Sobotka, M., Bonet, J.A., Vazquez, M.: 1993, A High-resolution Study of Inhomogeneities in Sunspot Umbrae. *Astrophys. J.* **415**, 832. doi:10.1086/173205.

Sobotka, M., Brandt, P.N., Simon, G.W.: 1997, Fine Structure in Sunspots. I. Sizes and Lifetimes of Umbral Dots. *Astron. Astrophys.* **328**, 682.

Sobotka, M., Brandt, P.N., Simon, G.W.: 1999, Fine Structure in Sunspots. III. Penumbral Grains. *Astron. Astrophys.* **348**, 621.

Sobotka, M., Del Moro, D., Jurčák, J., Berrilli, F.: 2012, Magnetic and Velocity Fields of a Solar Pore. *Astron. Astrophys.* **537**, A85. doi:10.1051/0004-6361/201117851.

Sobotka, M., Švanda, M., Jurčák, J., Heinzel, P., Del Moro, D., Berrilli, F.: 2013, Dynamics of the Solar Atmosphere above a Pore with a Light Bridge. *Astron. Astrophys.* **560**, A84. doi:10.1051/0004-6361/201322148.

Solanki, S.K.: 1993, Smallscale Solar Magnetic Fields – An Overview. *Space Sci. Rev.* **63**, 1. doi:10.1007/BF00749277.

Solanki, S.K.: 2003, Sunspots: An Overview. *Astron. Astrophys. Rev.* **11**, 153. doi:10.1007/s00159-003-0018-4.

Soltau, D., Acton, D.S., Kentischer, T., Roser, M., Schmidt, W., Stix, M., von der Luhe, O.: 1997, Adaptive Optics at the German VTT on Tenerife. In: Schmieder, B., del Toro Iniesta, J.C., Vazquez, M. (eds.) *1st Advances in Solar Physics Euroconference. Advances in Physics of Sunspots*, *ASP Conf. Ser.* **118**, 351.

Soltau, D., Volkmer, R., von der Lühe, O., Berkefeld, T.: 2012, Optical Design of the New Solar Telescope GREGOR. *Astron. Nachr.* **333**, 847. doi:10.1002/asna.201211730.

Srivastava, A.K., Kuridze, D., Zaqarashvili, T.V., Dwivedi, B.N.: 2008, Intensity Oscillations Observed with Hinode near the South Pole of the Sun: Leakage of Low Frequency Magneto-acoustic Waves into the Solar Corona. *Astron. Astrophys.* **481**, L95. doi:10.1051/0004-6361:20079328.

Stanchfield, I. D. C. H., Thomas, J.H., Lites, B.W.: 1997, The Vector Magnetic Field, Evershed Flow, and Intensity in a Sunspot. *Astrophys. J.* **477**, 485. doi:10.1086/303704.

Staude, J.: 1999, Sunspot Oscillations. In: Schmieder, B., Hofmann, A., Staude, J. (eds.) *Third Advances in Solar Physics Euroconference: Magnetic Fields and Oscillations*, *ASP Conf. Ser.* **184**, 113.

Stein, R.F., Lagerfjärd, A., Nordlund, Å., Georgobiani, D.: 2011, Solar Flux Emergence Simulations. *Solar Phys.* **268**, 271.

Stein, R.F., Lagerfjärd, A., Nordlund, ., Georgobiani, D.: 2012, Emerging Flux Simulations and Proto-Active Regions. In: Bellot Rubio, L., Reale, F., Carlsson, M. (eds.) *4th Hinode Science Meeting: Unsolved Problems and Recent Insights*, *ASP Conf. Ser.* **455**, 133.

Steiner, O., Hauschildt, P.H., Bruls, J.: 2001, Radiative Properties of Magnetic Elements. I. Why are G-band Bright Points Bright? *Astron. Astrophys.* **372**, L13.

Strecker, H., Bello González, N.: 2018, Evolution of the Flow Field in Decaying Active Regions. Transition from a Moat Flow to a Supergranular flow. *Astron. Astrophys.* **620**, A122. doi:10.1051/0004-6361/201732164.

Stuart, F.E., Rush, J.H.: 1954, Correlation Analyses of Turbulent Velocities and Brightness of the Photospheric Granulation. *Astrophys. J.* **120**, 245. doi:10.1086/145908.

Sütterlin, P.: 1998, Properties of Solar Pores. *Astron. Astrophys.* **333**, 305.

Sütterlin, P.: 2001, The Size of Penumbral Fine Structure. *Astron. Astrophys.* **374**, L21. doi:10.1051/0004-6361:20010872.

Thomas, J.H., Weiss, N.O., Tobias, S.M., Brummell, N.H.: 2002, Downward Pumping of Magnetic Flux as the Cause of Filamentary Structures in Sunspot Penumbrae. *Nature* **420**, 390. doi:10.1038/nature01174.

Tian, H., Yurchyshyn, V., Peter, H., Solanki, S.K., Young, P.R., Ni, L., *et al.*: 2018, Frequently Occurring Reconnection Jets from Sunspot Light Bridges. *Astrophys. J.* **854**, 92. doi:10.3847/1538-4357/aaa89d.

Tlatov, A.G.: 2023, Lifetime of Sunspots and Pores. *Solar Phys.* **298**, 93. doi:10.1007/s11207-023-02186-7.

Toriumi, S., Wang, H.: 2019, Flare-productive Active Regions. *Living Rev. Solar Phys.* **16**, 3. doi:10.1007/s41116-019-0019-7.

Toriumi, S., Cheung, M.C.M., Katsukawa, Y.: 2015, Light Bridge in a Developing Active Region. II. Numerical Simulation of Flux Emergence and Light Bridge Formation. *Astrophys. J.* **811**, 138. doi:10.1088/0004-637X/811/2/138.

Tortosa-Andreu, A., Moreno-Insertis, F.: 2009, Magnetic Flux Emergence into the Solar Photosphere and Chromosphere. *Astron. Astrophys.* **507**, 949. doi:10.1051/0004-6361/200912394.

Tritschler, A., Schlichenmaier, R., Bellot Rubio, L.R., KAOS Team, BerkefeldT., SchelenzT.: 2004, Two-dimensional Spectroscopy of a Sunspot. I. Properties of the Penumbral Fine Structure. *Astron. Astrophys.* **415**, 717. doi:10.1051/0004-6361:20034599.

Tsiropoula, G., Dialetis, D., Alissandrakis, C.E., Mein, P., Mein, N.: 1997, Evolution in Space and Time of Superpenumbral Chromospheric Fibrils. *Solar Phys.* **172**, 139. doi:10.1023/A:1004939631975.

Tsiropoula, G., Tziotziou, K., Kontogiannis, I., Madjarska, M.S., Doyle, J.G., Suematsu, Y.: 2012, Solar Fine-scale Structures. I. Spicules and other Small-scale, Jet-like Events at the Chromospheric Level: Observations and Physical Parameters. *Space Sci. Rev.* **169**, 181. doi:10.1007/s11214-012-9920-2.

Tsuneta, S., Ichimoto, K., Katsukawa, Y., Nagata, S., Otsubo, M., Shimizu, T., *et al.*: 2008, The Solar Optical Telescope for the Hinode Mission: An Overview. *Solar Phys.* **249**, 167. doi:10.1007/s11207-008-9174-z.

Uitenbroek, H., Tritschler, A.: 2006, The Contrast of Magnetic Elements in Synthetic CH- and CN-Band Images of Solar Magnetoconvection. *Astrophys. J.* **639**, 525. doi:10.1086/499331.

Unsöld, A.: 1930, Konvektion in der Sonnenatmosphäre (nebst einer Bemerkung zur Deutung der Novae). *Z. Astrophys.* **1**, 138.

Švanda, M., Sobotka, M., Bárta, T.: 2014, Moat Flow System around Sunspots in Shallow Subsurface Layers. *Astrophys. J.* **790**, 135. doi:10.1088/0004-637x/790/2/135.

van Driel-Gesztelyi, L., Green, L.M.: 2015, Evolution of Active Regions. *Living Rev. Solar Phys.* **12**, 1. doi:10.1007/lrsp-2015-1.

van Noort, M., Rouppe van der Voort, L., Löfdahl, M.G.: 2005, Solar Image Restoration by Use of Multi-frame Blind Deconvolution with Multiple Objects and Phase Diversity. *Solar Phys.* **228**, 191. doi:10.1007/s11207-005-5782-z.

Vargas Domínguez, S., Rouppe van der Voort, L., Bonet, J.A., Martínez Pillet, V., Van Noort, M., Katsukawa, Y.: 2008, Moat Flow in the Vicinity of Sunspots for Various Penumbral Configurations. *Astrophys. J.* **679**, 900. doi:10.1086/587139.

Varsik, J., Plymate, C., Goode, P., Kosovichev, A., Cao, W., Coulter, R., et al.: 2014, Control and operation of the 1.6 m New Solar Telescope in Big Bear. In: Ramsay, S.K., McLean, I.S., Takami, H. (eds.) *Ground-based and Airborne Instrumentation for Astronomy V*, *Proc. SPIE* **9147**, 91475D. doi:10.1117/12.2056688.

Vega Reyes, N., Esteves, M.A., Sánchez-Capuchino, J., Salaun, Y., López, R.L., Gracia, F., et al.: 2016, Opto-mechanical Design of an Image Slicer for the GRIS Spectrograph at GREGOR. In: Navarro, R., Burge, J.H. (eds.) *Advances in Optical and Mechanical Technologies for Telescopes and Instrumentation II*, *Proc. SPIE* **9912**, 99125P. doi:10.1117/12.2232615.

Verdoni, A.P., Denker, C.: 2007, The Local Seeing Environment at Big Bear Solar Observatory. *Publ. Astron. Soc. Pac.* **119**, 793. doi:10.1086/520773.

Verma, M.: 2018, The Origin of two X-class Flares in Active Region NOAA 12673. Shear Flows and Head-on Collision of New and Preexisting Flux. *Astron. Astrophys.* **612**, A101. doi:10.1051/0004-6361/201732214.

Verma, M., Denker, C.: 2011, Horizontal Flow Fields Observed in Hinode G-band Images. I. Methods. *Astron. Astrophys.* **529**, A153. doi:10.1051/0004-6361/201016358.

Verma, M., Denker, C.: 2012, Horizontal Flow Fields Observed in Hinode G-band Images. III. The Decay of a Satellite Sunspot and the Role of Magnetic Flux Removal in Flaring. *Astron. Astrophys.* **545**, A92. doi:10.1051/0004-6361/201219694.

Verma, M., Denker, C.: 2014, Horizontal Flow Fields Observed in Hinode G-band Images. IV. Statistical Properties of the Dynamical Environment around Pores. *Astron. Astrophys.* **563**, A112. doi:10.1051/0004-6361/201322476.

Verma, M., Kummerow, P., Denker, C.: 2018a, On the Extent of the Moat flow in Axisymmetric Sunspots. *Astron. Nachr.* **339**, 268. doi:10.1002/asna.201813482.

Verma, M., Steffen, M., Denker, C.: 2013, Evaluating Local Correlation Tracking Using CO5BOLD Simulations of Solar Granulation. *Astron. Astrophys.* **555**, A136. doi:10.1051/0004-6361/201321628.

Verma, M., Balthasar, H., Deng, N., Liu, C., Shimizu, T., Wang, H., Denker, C.: 2012, Horizontal Flow Fields Observed in Hinode G-band Images. II. Flow Fields in the Final Stages of Sunspot Decay. *Astron. Astrophys.* **538**, A109. doi:10.1051/0004-6361/201117842.

Verma, M., Denker, C., Böhm, F., Balthasar, H., Fischer, C.E., Kuckein, C., *et al.*: 2016a, Flow and Magnetic Field Properties in the Trailing Sunspots of Active Region NOAA 12396. *Astron. Nachr.* **337**, 1090. doi:10.1002/asna.201612447.

Verma, M., Denker, C., Balthasar, H., Kuckein, C., González Manrique, S.J., Sobotka, M., *et al.*: 2016b, Horizontal Flow Fields in and around a Small Active Region – The Transition Period Between Flux Emergence and Decay. *Astron. Astrophys.* **596**, A3. doi:10.1051/0004-6361/201628380.

Verma, M., Denker, C., Balthasar, H., Kuckein, C., Rezaei, R., Sobotka, M., *et al.*: 2018b, High-resolution Imaging and Near-infrared Spectroscopy of Penumbral Decay. *Astron. Astrophys.* **614**, A2. doi:10.1051/0004-6361/201731801.

Verma, M., Denker, C., Diercke, A., Kuckein, C., Balthasar, H., Dineva, E., *et al.*: 2020, High-resolution Spectroscopy of a Surge in an Emerging Flux Region. *Astron. Astrophys.* **639**, A19. doi:10.1051/0004-6361/201936762.

von der Lühe, O.: 1984, Estimating Fried's Parameter from a Time Series of an Arbitrary Resolved Object Imaged through Atmospheric Turbulence. *J. Opt. Soc. Am. A* **1**, 510. doi:10.1364/JOSAA.1.000510.

von der Lühe, O.: 1993, Speckle Imaging of Solar Small Scale Structure. I. Methods. *Astron. Astrophys.* **268**, 374.

von der Lühe, O.: 1998, High-Resolution Observations with the German Vacuum Tower Telescope on Tenerife. *New Astron. Rev.* **42**, 493. doi:10.1016/S1387-6473(98)00060-8.

von der Lühe, O., Soltau, D., Berkefeld, T., Schelenz, T.: 2003, KAOS: Adaptive Optics System for the Vacuum Tower Telescope at Teide Observatory. In: Keil, S.L., Avakyan, S.V. (eds.) *Innovative Telescopes and Instrumentation for Solar Astrophysics*, *Proc. SPIE* **4853**, 187. doi:10.1117/12.498659.

Švanda, M., Klvaňa, M., Sobotka, M.: 2009, Large-scale Horizontal Flows in the Solar Photosphere. V. Possible Evidence for the Disconnection of Bipolar Sunspot Groups from their Magnetic Roots. *Astron. Astrophys.* **506**, 875. doi:10.1051/0004-6361/200912422.

Wang, H., Zirin, H.: 1992, Flows Around Sunspots and Pores. *Solar Phys.* **140**, 41. doi:10.1007/BF00148428.

Wang, H., Johannesson, A., Stage, M., Lee, C., Zirin, H.: 1998, Study of H$\alpha$ Jets on the Quiet Sun. *Solar Phys.* **178**, 55.

Wang, H., Liu, C., Qiu, J., Deng, N., Goode, P.R., Denker, C.: 2004, Rapid Penumbral Decay Following Three X-Class Solar Flares. *Astrophys. J. Lett.* **601**, 195. doi:10.1086/382188.

Wang, H., Yurchyshyn, V., Liu, C., Ahn, K., Toriumi, S., Cao, W.: 2018a, Strong Transverse Photosphere Magnetic Fields and Twist in Light Bridge Dividing Delta Sunspot of Active Region 12673. *Res. Not. Amer. Astron. Soc.* **2**, 8. doi:10.3847/2515-5172/aaa670.

Wang, J., Liu, C., Deng, N., Wang, H.: 2018b, Evolution of Photospheric Flow and Magnetic Fields Associated with the 2015 June 22 M6.5 Flare. *Astrophys. J.* **853**, 143. doi:10.3847/1538-4357/aaa712.

Watanabe, H., Kitai, R., Otsuji, K.: 2014, Formation and Decay of Rudimentary Penumbra around a Pore. *Astrophys. J.* **796**, 77. doi:10.1088/0004-637X/796/2/77.

Watanabe, H., Bellot Rubio, L.R., de la Cruz Rodríguez, J., Rouppe van der Voort, L.: 2012, Temporal Evolution of Velocity and Magnetic Field in and around Umbral Dots. *Astrophys. J.* **757**, 49. doi:10.1088/0004-637X/757/1/49.

Weigelt, G., Wirnitzer, B.: 1983, Image Reconstruction by the Speckle-masking Method. *Opt. Lett.* **8**, 389. doi:10.1364/OL.8.000389.

Weiss, N.O., Thomas, J.H., Brummell, N.H., Tobias, S.M.: 2004, The Origin of Penumbral Structure in Sunspots: Downward Pumping of Magnetic Flux. *Astrophys. J.* **600**, 1073. doi:10.1086/380091.

Wells, D.C., Greisen, E.W., Harten, R.H.: 1981, FITS – A Flexible Image Transport System. *Astron. Astrophys. Suppl. Ser.* **44**, 363.

Wilken, V., de Boer, C.R., Denker, C., Kneer, F.: 1997, Speckle Measurements of the Centre-to-limb Variation of the Solar Granulation. *Astron. Astrophys.* **325**, 819.

Wöger, F., von der Lühe, O.: 2007, Field Dependent Amplitude Calibration of Adaptive Optics Supported Solar Speckle Imaging. *Appl. Opt.* **46**, 8015. doi:10.1364/AO.46.008015.

Wöger, F., von der Lühe, O.: 2008, KISIP: A Software Package for Speckle Interferometry of Adaptive Optics Corrected Solar Data. In: Bridger, A., Radziwill, N.M. (eds.) *Advanced Software and Control for Astronomy II*, *Proc. SPIE* **7019**, 70191E. doi:10.1117/12.788062.

Wöger, F., von der Lühe, O., Reardon, K.: 2008, Speckle Interferometry with Adaptive Optics Corrected Solar Data. *Astron. Astrophys.* **488**, 375. doi:10.1051/0004-6361:200809894.

Wöger, F., Rimmele, T., Ferayorni, A., Beard, A., Gregory, B.S., Sekulic, P., Hegwer, S.L.: 2021, The Daniel K. Inouye Solar Telescope (DKIST)/Visible Broadband Imager (VBI). *Solar Phys.* **296**, 145. doi:10.1007/s11207-021-01881-7.

Woods, T.N., Eparvier, F.G., Hock, R., Jones, A.R., Woodraska, D., Judge, D., *et al.*: 2012, Extreme Ultraviolet Variability Experiment (EVE) on the Solar Dynamics Observatory (SDO): Overview of Science Objectives, Instrument Design, Data Products, and Model Developments. *Solar Phys.* **275**, 115. doi:10.1007/s11207-009-9487-6.

Yang, G., Xu, Y., Wang, H., Denker, C.: 2003, High Spatial Resolution Observations of Pores and the Formation of a Rudimentary Penumbra. *Astrophys. J.* **597**, 1190. doi:10.1086/377128.

Yang, X., Cao, W., Gorceix, N., Plymate, C., Shumoko, S., Bai, X., et al.: 2020, CYRA: The Cryogenic Infrared Spectrograph for the Goode Solar Telescope in Big Bear. In: Evans, C.J., Bryant, J.J., Motohara, K. (eds.) *Ground-based and Airborne Instrumentation for Astronomy VIII*, *Proc. SPIE* **11447**, 11447AG. doi:10.1117/12.2562474.

Zhang, J., Tian, H., He, J., Wang, L.: 2017, Surge-like Oscillations above Sunspot Light Bridges Driven by Magnetoacoustic Shocks. *Astrophys. J.* **838**, 2. doi:10.3847/1538-4357/aa63e8.

Zirin, H., Stein, A.: 1972, Observations of Running Penumbral Waves. *Astrophys. J. Lett.* **178**, L85. doi:10.1086/181089.

Zwaan, C.: 1985, The Emergence of Magnetic Flux. *Solar Phys.* **100**, 397. doi:10.1007/978-94-009-4588-3_20.

## Appendix A – List of acronyms

| | |
|---|---|
| **AIA** | Atmospheric Imaging Assembly |
| **AIP** | Leibniz-Institut für Astrophysik Potsdam |
| **AO** | Adaptive Optics |
| **ASU** | Astronomical Institute of the Academy of Sciences of the Czech Republic |
| **BaSAMs** | Background-subtracted Activity Maps |
| **BBSO** | Big Bear Solar Observatory |
| **BFI** | Broad-band Filter Imager |
| **CCD** | Charged Coupled Device |
| **CLV** | Center-to-limb-variation |
| **CME** | Coronal Mass Ejection |
| **CMOS** | Complementary Metal-Oxide-Semiconductors |
| **CYRA** | CrYogenic solar spectrogRAph |
| **DIM** | Differential Image Motion |
| **DK** | Dark Frames |
| **DKIST** | Daniel K. Inouye Solar Telescope |
| **DM** | Deformable Mirror |
| **EFR** | Emerging Flux Region |
| **EST** | European Solar Telescope |
| **EUV** | Extreme Ultra-violet |
| **EVE** | Extreme Ultraviolet Variability Experiment |
| **FaMuLUS** | Fast Multi-Line Universal Spectrograph |
| **FFT** | fast Fourier transform |
| **FISS** | Fast Imaging Solar Spectrograph |
| **FITS** | Flexible Image Transport System |
| **FOV** | Field-of-view |
| **FWHM** | Full-width-at-half-maximum |
| **GAOS** | GREGOR adaptive optics system |
| **GRIS** | GREGOR Infrared Spectrograph |
| **GST** | Goode Solar Telescope |
| **GUI** | Graphical User Interface |
| **HELLRIDE** | HELioseismic Large Region Interferometric DEvice |
| **HiFI** | High-resolution Fast Imager |
| **HiFI+** | Improved High-resolution Fast Imager |
| **HMI** | Helioseismic and Magnetic Imager |
| **HSM** | Helmli-Scherer mean |
| **IAC** | Instituto de Astrofísica de Canarias |
| **IDL** | Interactive Data Language |
| **IFU** | Integral Field Unit |
| **IRIM** | InfraRed Imaging Magnetograph |
| **KIS** | Institut für Sonnenphysik |
| **KISIP** | Kiepenheuer-Institute Speckle Interferometry Package |
| **KAOS** | Kiepenheuer Adaptive Optics System |

| | |
|---|---|
| **LARS** | Laser Absolute Reference Spectrograph |
| **LCT** | Local Correlation Tracking |
| **Living With a Star** | LWS |
| **LOS** | Line-of-sight |
| **LTE** | Local Thermodynamic Equilibrium |
| | |
| **MFBD** | Multi-frame Blind Deconvolution |
| **MFGS** | Median Filter Laplacian Similarity |
| **MFLS** | Median Filter Gradient Similarity |
| **MHD** | Magnetohydrodynamics |
| **MMF** | Moving Magnetic Features |
| **MOMFBD** | Multi-object Multi-frame Blind Deconvolution |
| **MPS** | Max-Planck-Institut für Sonnensystemforschung in Göttingen |
| | |
| **NIR** | Near infrared |
| **NJIT** | New Jersey Institute of Technology |
| **NOAA** | National Oceanic and Atmospheric Administration |
| | |
| **OT** | Observatorio del Teide |
| | |
| **RMS** | Root Mean Square |
| **ROI** | Region-of-interest |
| **RTE** | Radiative Transfer Equation |
| | |
| **sCMOS** | scientific Complementary Metal-Oxide-Semiconductors |
| **SDO** | Solar Dynamics Observatory |
| **SIR** | Stokes Inversions based on Response function |
| **SOT** | Solar Optical Telescope |
| **SHARP** | Spaceweather HMI Active Region Patch |
| **SSD** | Solid State Drives |
| **SST** | Swedish Solar Telescope |
| **SVD** | Singular Value Decomposition |
| | |
| **UV** | Ultra-violet |
| | |
| **VIM** | Visible Imaging Magnetograph |
| **VIS** | Visible Imaging Spectrograph |
| **VTT** | Vacuum Tower Telescope |
| | |
| **WFS** | Wavefront sensor |

# Appendix B – Abstracts

## Spectral Background-Subtracted Activity Maps

Denker, C., Verma, M., Pietrow, A.G.M., Kontogiannis, I., Kamlah, R.: 2023, *Res. Not. Am. Astron. Soc.* **7**, 224. doi:10.3847/2515-5172/ad04e0

High-resolution solar spectroscopy provides a wealth of information from photospheric and chromospheric spectral lines. However, the volume of data easily exceeds hundreds of millions of spectra on a single observation day. Therefore, methods are needed to identify spectral signatures of interest in multidimensional datasets. Background-subtracted activity maps (BaSAMs) have previously been used to locate features of solar activity in time series of images and filtergrams. This research note shows how this method can be extended and adapted to spectral data.

## A Comparative Study of Two X2.2 and X9.3 Solar Flares Observed with HARPS-N. Reconciling Sun-as-a-star Spectroscopy and High-spatial Resolution Solar Observations in the Context of the Solar-stellar Connection

Pietrow, A.G.M., Cretignier, M., Druett, M.K., Alvarado-Gómez, J.D., Hofmeister, S.J., Verma, M., Kamlah, R., Baratella, M., Amazo-Gómez, E.M., Kontogiannis, I., Dineva, E., Warmuth, A., Denker, C., Poppenhaeger, K., Andriienko, O., Dumusque, X., Löfdahl, M.G.: 2024, *Eur. Geosci. Union Gen. Assem.*, EGU24-12140. doi:10.5194/egusphere-egu24-12140.

Stellar flares cannot be spatially resolved, which complicates ascertaining the physical processes behind particular spectral signatures. Due to their proximity to Earth, solar flares can serve as a stepping stone for understanding their stellar counterparts, especially when using a Sun-as-a-star instrument and in combination with spatially resolved observations. We aim to understand the disk-integrated spectral behaviors of a confined X2.2 flare and its eruptive X9.3 successor, which had energies of $2.2\times10^{31}$ erg and $9.3\times10^{31}$ erg, respectively, as measured by Sun-as-a-star observations with the High Accuracy Radial velocity Planet Searcher for the Northern hemisphere (HARPS-N). The behavior of multiple photospheric (Na $D_1$ & $D_2$, Mg I at 5173 Å, Fe I at 6173 Å, and Mn I at 4031 Å) and chromospheric (Ca II H & K, H$\alpha$, H$\beta$, and He I $D_3$) spectral lines were investigated by means of activity indices and contrast profiles. A number of different photospheric lines were also investigated by means of equivalent widths, and radial velocity measures, which were then related to physical processes directly observed in high-resolution observations made with the Swedish 1-meter Solar Telescope (SST) and the Atmospheric Imaging Assembly (AIA) on board of the Solar Dynamics Observatory (SDO). Our findings suggest a relationship between the evolving shapes of contrast profile time and the flare locations, which assists in constraining flare locations in disk-integrated observations. In addition, an upward bias was found in flare statistics based on activity indices derived from the Ca II H & K lines. In this case, much smaller flares cause a similar increase in the activity index as that produced by larger flares. H$\alpha$-based activity indices do not show this bias and are therefore less susceptible to activity jitter. Sodium line profiles show a strongly asymmetric response during flare activity, which is best captured with a newly defined asymmetrical sodium activity index. A strong flare response was detected in Mn I line profiles, which is unexpected and calls for further exploration. Intensity increases in H$\alpha$, H$\beta$, and certain spectral windows of AIA before the flare onset suggest their potential use as short-term flare predictors.

## Improved High-resolution Fast Imager

Denker, C., Verma, M., Wiśniewska, A., Kamlah, R., Kontogiannis, I., Dineva, E., Rendtel, J., Bauer, S.-M., Dionies, M., Önel, H., Woche, M., Kuckein, C., Seelemann, T., Pal, P.: 2023, *J. Astron. Tel. Instr. Sys.*, **9**, 015001. doi:10.1117/1.JATIS.9.1.015001.

The improved *High-resolution Fast Imager* (HiFI+) is a multi-wavelength imaging filtergraph, which was commissioned at the GREGOR solar telescope at Observatorio del Teide, Izaña, Tenerife, Spain in March 2022 – followed by science verification in April 2022, after which it entered routine observations. Three camera control computers with two synchronized sCMOS & CMOS cameras each provide near diffraction-limited imaging at high cadence in six wavelength bands (Ca II H at 396.8 nm, G-band at 430.7 nm, blue

continuum at 450.6 nm, narrow- and broad-band H$\alpha$ at 656.3 nm, and TiO bandhead at 705.8 nm). This unique combination of photospheric and chromospheric images provides "tomographic" access to the dynamic Sun and complements spectropolarimetric observations at the GREGOR telescope. High image acquisition rates of 50 & 100 Hz facilitate image restoration, where time-series of restored images have a typical cadence of 6 & 12 s, which is sufficient to resolve the dynamics of the solar photosphere and chromosphere. In principle, all imaging channels can be restored individually using the speckle masking technique or Multi-Frame Blind Deconvolution (MFBD). However, images recorded strictly simultaneously in the narrow-/broad-band H$\alpha$ and the G-band/blue continuum channels can be pairwise subjected to Multi-Object Multi-Frame Deconvolution (MOMFBD) expanding the science capabilities of HiFI+. For example, the narrow-band (FWHM = 60 nm) Halle H$\alpha$ Lyot filter isolates the H$\alpha$ line core, which thus facilitates matching chromospheric fibrils and filamentary structures to photospheric bright points. Likewise, dividing G-band by blue continuum images enhances small-scale brightenings, which are often related to small-scale magnetic fields, so that their evolution can be tracked in time. A detailed description of the new high-cadence, large-format imaging system is presented and its performance is assessed based on first-light observations.

### Classification of High-resolution Solar H$\alpha$ Spectra Using t-distributed Stochastic Neighbor Embedding

Verma, M., Matijevič, G., Denker, C., Diercke, A., Dineva, E, Balthasar, H., Kamlah, R., Kontogiannis, I., Kuckein, C., Pal, P.: 2021, *Astrophys. J.*, **907**, 54. doi:10.3847/1538-4357/abcd95.

The H$\alpha$ spectral line is a well-studied absorption line revealing properties of the highly structured and dynamic solar chromosphere. Typical features with distinct spectral signatures in H$\alpha$ include filaments and prominences, bright active-region plages, superpenumbrae around sunspots, surges, flares, Ellerman bombs, filigree, and mottles and rosettes, among others. This study is based on high-spectral resolution H$\alpha$ spectra obtained with the Echelle spectrograph of the Vacuum Tower Telescope (VTT) located at Observatorio del Teide, Tenerife, Spain. The t-distributed stochastic neighbor embedding (t-SNE) is a machine-learning algorithm, which is used for nonlinear dimensionality reduction. In this application, it projects H$\alpha$ spectra onto a two-dimensional map, where it becomes possible to classify the spectra according to results of cloud model (CM) inversions. The CM parameters optical depth, Doppler width, line-of-sight velocity, and source function describe properties of the cloud material. Initial results of t-SNE indicate its strong discriminatory power to separate quiet-Sun and plage profiles from those that are suitable for CM inversions. In addition, a detailed study of various t-SNE parameters is conducted, the impact of seeing conditions on the classification is assessed, results for various types of input data are compared, and the identified clusters are linked to chromospheric features. Although t-SNE proves to be efficient in clustering high-dimensional data, human inference is required at each step to interpret the results. This exploratory study provides a framework and ideas on how to tailor a classification scheme toward specific spectral data and science questions.

### Wavelength Dependence of Image Quality Metrics and Seeing Parameters and their Relation to Adaptive Optics Performance

Kamlah, R., Verma, M., Diercke, A., Denker, C.: 2021, *Sol. Phys.*, **296**, 29. doi:10.1007/s11207-021-01771-y.

Ground-based solar observations are severely affected by Earth's turbulent atmosphere. As a consequence, observed image quality and prevailing seeing conditions are closely related. Partial correction of image degradation is nowadays provided in real time by adaptive optics (AO) systems. In this study, different metrics of image quality are compared with parameters characterizing the prevailing seeing conditions, i.e., Median Filter Gradient Similarity (MFGS), Median Filter Laplacian Similarity (MFLS), Helmli-Scherer mean, granular rms-contrast, differential image motion, and Fried-parameter $r_0$. The quiet-Sun observations at disk center were carried out at the Vacuum Tower Telescope (VTT), Observatorio del Teide (OT), Izaña, Tenerife, Spain. In July and August 2016, time-series of short-exposure images were recorded with the High-resolution Fast Imager (HiFI) at various wavelengths in the visible and near-infrared parts of the spectrum. Correlation analysis yields the wavelength dependence of the image quality metrics

and seeing parameters, and Uniform Manifold Approximation and Projection (UMAP) is employed to characterize the seeing on a particular observing day. In addition, the image quality metrics and seeing parameters are used to determine the field dependence of the correction provided by the AO system. Management of high-resolution imaging data from large-aperture, ground-based telescopes demands reliable image quality metrics and meaningful characterization of prevailing seeing conditions and AO performance. The present study offers guidance on how retrieving such information ex post facto.

## Acknowledgement

I would like to express my deepest gratitude to my supervisor, Prof. Dr. Carsten Denker, for all his support and contributions to this thesis. Without his support, this thesis would not have been the same. It is my intention to continue to apply the same quality standards and work ethics to my own life that have been introduced by him. I would like to express my sincerest gratitude to my second supervisor, Dr. Meetu Verma. Through her DFG project, titled ”From Flux Emergence to Decay – A High-resolution Study of Sunspots”, she secured the necessary funding to support my PhD research, providing me the opportunity to pursue my dream. She has consistently provided invaluable guidance and support, and without her input, this thesis would not have been the same. It has been a privilege to work under her supervision, and I hope for future collaborative opportunities. Both of my supervisors have become more than just colleagues and mentors, but more like a small family away from home. Thanks a lot for everything. Without you I could not have done this.

Furthermore, I would like to express my gratitude to the entire solar physics group for making the experience of this PhD research an enjoyable one. In particular, Dr. Ekaterina Dineva, with whom I shared an office for so long. Thanks for being a good office mate, always there for a laugh or great discussions. Furthermore, I want to thank my colleagues, Dr. Ioannis Kontogiannis, Dr. Alexander Pietrow, Dr. Horst Balthasar, Dr. Jürgen Rendtel, and Dr. Partha Pal. I really enjoyed our discussions, observing trips, and of course procrastination time. Thanks for all the advice and support.

Moreover, I would like to express my gratitude to my parents, Frank and Susanne. Thanks for your unconditional love and support. You were always there when needed, and I could not have wished for better parents. As well as my brothers Martin and Philipp. Thanks for always cheering me up and being so supportive and just great. You could almost be considered human.

Honorary mentions to Prof. Dr. Michael Vollmer and Prof. Dr. Klaus-Peter Möllmann for their guidance and support during my bachelor and master studies. Their dedication and support, which went beyond their teaching duties, is greatly appreciated and helped pave the way for my Ph.D. studies.

Special thanks to my almost bandmates Ioannis and Jad. Although we did not have enough time, I really enjoyed the clearing of head space jamming with you guys. Same for my buddies, Alex, Ioannis, Jad, and Judy. I really enjoyed our adventures and fun activities that served as great intermissions. Dado, you always manage to put a smile on my face. Just stay who you are. Sophia, thanks for being so supportive, recharging influence, and encouragement to take breaks. Thanks to the entire Mießner family, Kerstin, Gerhard, Julia, and Merle. In particular, Julia, for encouraging me to start this path in the first place. And finally my Brother Basti. Although you are not here anymore, you will always be with me.

We gratefully acknowledge the use of data from the Goode Solar Telescope (GST) of the Big Bear Solar Observatory (BBSO). The GREGOR solar telescope and the Vacuum Tower Telescope (VTT) at the Spanish Observatorio del Teide of the Instituto de Astrofísica de Canarias are operated by the German consortium of the Institut für Sonnenphysik (KIS) in Freiburg, the Leibniz-Institut für Astrophysik Potsdam (AIP), and the Max-Planck-Institut für Sonnensystemforschung (MPS) in Göttingen. SDO HMI and AIA data are provided by the Joint Science Operations Center – Science Data Processing. This research has made use of NASA’s Astrophysics Data System Bibliographic Services. This study was supported by grants DE 787/5-1 and VE 1112/1-1 of the Deutsche Forschungsgemeinschaft (DFG). In addition, the support by the European Commission’s Horizon 2020 Program under grant agreements 824064 (ESCAPE – European Science Cluster of Astronomy & Particle physics ESFRI research infrastructures) and 824135 (SOLARNET – Integrating High Resolution Solar Physics) is highly appreciated.